MASTER

An experimental study of the radial additive density and plasma temperature profiles, and the effect of this on the integral light output of metal halide lamps as a function of gravity

Kemps, P.C.M.

Award date:
2004

Link to publication

An experimental study of the radial additive density and plasma temperature profiles, and the effect of this on the integral light output of metal halide lamps as a function of gravity

Pim Kemps

EPG

April 2004

Summary

High-pressure metal halide lamps are very efficient electrical discharge lamps with a very high intensity. They are widely used for shop lighting, stadium lighting and city beautification, and are promising lamps for other application areas in the future, due to their high efficiency. However, as a result of diffusive and convective effects, axial additive segregation arises in these lamps, which reduces the lamp efficiency and causes the lamp to suffer from color separation in case of a vertical burner orientation. This effect is due to the two-dimensional properties of the discharge and is both difficult to analyze with diagnostic tools and complex to model.

The ARGES project, which is a collaborative project between the Eindhoven University of Technology (TU/e) and Philips Central Development Lighting (CDL), aims to measure the radial additive density and temperature profile of quartz metal halide lamps under micro-gravity conditions. The micro-gravity conditions are aimed to create a one-dimensional discharge, which is more easy to model. Spectroscopic measurements are used to calculate the temperature and radial additive density profile of the burning lamps.

In this report a method is presented to calculate the plasma temperature profile with the use of the absolute intensity of the 579 nm optically thin mercury emission line. This emission line is one of the selected emission lines to be measured, detectable with the previously developed space-compatible spectrometer. After measurements in parabolic flights, as preparation for the ISS mission in April 2004, the plasma temperature profiles have been successfully determined. With the additive emission line intensities also measured, the additive density profile has been calculated for one dysprosium lamp in different gravitational situations. This is done to prove the adequacy of the developed method, and resulted in the calculated additive density profiles to correspond with the expectations.

Moreover, an extra experiment was successfully developed to measure the integral luminous output of ceramic metal halide lamps as a function time, and thus of gravity, when attending a parabolic flight. The measurements have been analyzed and discussed qualitatively, and give more insight in the complex processes inside a metal halide lamp.

Contents

1 Introduction

1.1 Philips Lighting and the ARGES Project

Philips Lighting produces and develops a great variety of lamps including High-Intensity Discharge (HID) lamps. More and more applications with this type of lamp are developed recently, such as car head lighting (Xenon) and data projector lamps (UHP). The market of HID-lamps for road illumination, city beautification, stadium and shop lighting is still growing. The market is however demanding more efficient lamps, with a better colour, a longer life and at a lower price. These are the driving factors for the HID group at Philips Central Development Lighting (CDL) to investigate the processes in an HID lamp and to improve the performance of these type of lamps. Modern HID lamps have an energy efficiency of up to 40%, which is about 10 times better than that of a common use incandescent lamp. Considering the fact that the energy consumption of light is about 25% of the total electricity consumption, HID lamps are a promising product for reducing the world energy consumption.

The light in these type of lamps is generated by an electric discharge in mainly mercury vapour. The first high-pressure mercury lamp dates from 1906 [5], and consists of a quartz tube filled with mercury gas at super-atmospheric pressure. This lamp produces a bluish light. The demand for a better colour and efficiency of the lamp led to the introduction of the *metal halide lamp* in 1960 [35]. This is essentially a regular high pressure mercury discharge with a small amount of metal halide additives put into the discharge tube. The many emission lines of mainly used additive metals like Sodium (Na), Dysprosium (Dy), Cerium (Ce), Thallium (Tl) or Scandium (Sc) can make the light of the lamp sparkling white and much more energy efficient.

However some scientific problems like *segregation effects* of additives [7][9][14] and all kinds of instabilities occur in metal halide lamps. Due to segregation effects the colour of light originating from the top of a vertically burning lamp can differ from the light from the lower part of the lamp. An example of a hardly understood instability is the *helical instability* [16], where the discharge starts spiralling around its central axis, resulting in a flickering lamp. These effects are important limiting factors for the further improvement of the performance metal halide lamps, and that is why extensive research is being conducted on these phenomena. Better understanding can be achieved by diagnostically analysing the discharge or perform modelling. But because the

segregation effect leads to a two-dimensional density distribution of the additives, modelling of the discharge is rather complex. A possible way of reducing the complexity of the modelling is by investigating a one dimensional discharge. Such a discharge manifests itself when a lamp is burned in the absence of gravitational forces. The convection flows that are the cause of axial segregation are not present in the absence of gravity. The European Space Agency (ESA) [18] presents several ways of achieving this situation, like *parabolic flights* and missions to the *International Space Station* (ISS).

In spring 2002 Philips Lighting CDL and the group Elementary Processes in Gas discharges (EPG) of Eindhoven University of Technology (TU/e) were given the opportunity to participate in the Dutch DELTA-mission [19], and have the possibility of doing experiments in the ISS. The Dutch cosmonaut André Kuipers will be able to perform experiments during his two week space mission after his launch scheduled for the 19th of April 2004. This is an excellent opportunity to study metal halide lamps under micro-gravity conditions. The collaborative project of Philips CDL and TU/e is called *ARGES*, an acronym for **A**tomic densities measured **R**adially in metal halide lamps under micro**G**ravity conditions with **E**mission and absorption **S**pectroscopy. The exclusively designed space experiment, filled with 20 metal halide lamps, has successfully been launched at the 29th of January 2004 with a Russian Progress spacecraft and at the time of writing the experiment is stored in the ISS, waiting for André Kuipers to initialise the experiment and start the measurement sequence.

1.2 Metal halide lamps

An example of two different HID lamps is shown in Figure 1.1. The light emitting discharge is contained in a *burner* made of polycrystalline aluminum-oxide (PCA) or quartz. The burner is placed inside an outer balloon, called *BuBa* (which comes from the Dutch word "BUitenBAllon"), which is either vacuum or filled with an inert gas like nitrogen.
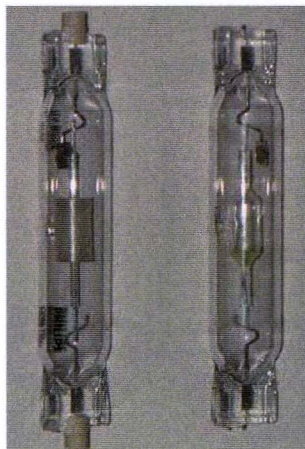

Figure 1.1: *A photograph of the used HID-lamps. Left a double ended lamp with a PCA burner is shown, on the right a lamp with a quartz burner is visible. The small metal plate in the outer balloon is a so called "getter", which keeps the vacuum inside the outer balloon clean.*

The lamps shown in Figure 1.1 are of the *double ended* type, which means that the electrical connections emerge from both sides of the outer balloon. Philips Lighting also produces single ended lamps, where both electrical connections are mounted to one side of the outer balloon and a return wire runs parallel to the burner. In order to preserve a clean vacuum inside the outer balloon, a *getter* is mounted inside the outer balloon. This small plate of Zirconium-Aluminum reacts with possible contaminations in the vacuum.
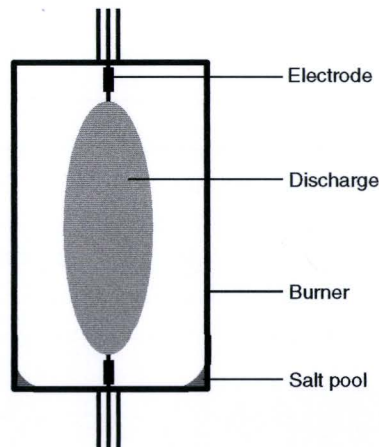
Figure 1.2: *A schematic drawing of a burner. The salt pool is always located on the coldest spot of the burner wall.*

A schematic drawing of a typical burner is shown in Figure 1.2. The burner is typically filled with a few milligram of mercury, the buffer gas, which completely evaporates during lamp operation. Because the temperature of the discharge is typically around 5500 K in the center and around 1200 K near the burner wall, this leads to a total mercury pressure of typically 5 to 30 Bar. The few milligrams of metal halide additive (for example DyI_3 or $NaCeI$) in most cases do not entirely evaporate and a liquid *salt pool* is therefore located at the coldest spot of the burner wall. The typical partial pressure of the additives lies between 5-50 mBar, but the temperature of the salt pool determines the actual vapor pressure of the additive in the discharge. This cold spot temperature is a very important parameter when designing a new lamp. Because the additives usually have a lot of emission lines in the visible part of the spectrum, combined with the fact that their excitation and ionization energy is much lower than that of mercury, the additives take care of the majority of the emitted radiation. This is why the additives are called *the radiating species.* By changing the composition of the additive mixture the color of the lamp can be adjusted. The dominant role of the additives make metal halide lamps very sensitive to changes in the density distribution of these additives.

After the ignition of a metal halide lamp with a high voltage pulse, a conducting arc channel is formed. After that, two burning phases can be distinguished. During the *run-up phase* the temperature of the discharge increases, the buffer gas evaporates and starts to emit radiation. In the third phase the additive iodides start to evaporate and enter the discharge. At this point the amount of emitted radiation increases significantly, up to 50% more than an ordinary mercury discharge at the same power.

The discharge has a negative current-voltage characteristic, so applying a higher current to the discharge will result in a lower resistance and hence an even higher current. This is why a metal halide lamp can not be plugged in directly to an ordinary power outlet. The current in the discharge will then increase until the burner explodes. For normal use of a metal halide lamp a current limiting element (usually called "Driver" or "Ballast") is necessary. Modern drivers present a square wave voltage of about 50-200 Hz with a maximum of about 200 V_{rms} and limit the current through the discharge. By varying the allowed current, the lamp power can be adjusted.

1.3   Parabolic flights

In order to test the prototype of the space experiment and to do measurements with the metal halide lamp under micro gravity conditions, the Arges team attended the 35th ESA Parabolic Flight Campaign (PFC) in October 2003. This PFC is organized by Novespace [20] and ESA [18] at the Merignac airport, Bordeaux, France. During the three days of the PFC the specially equipped "Zero-g" Airbus A300 (Figure 1.3) performs 31 parabolas a day (Figure 1.4).
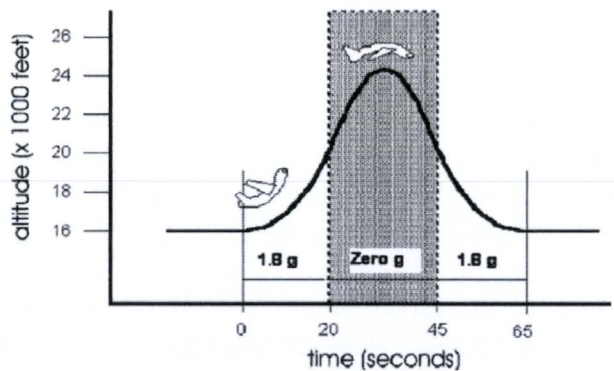
Figure 1.3: The zero-g airplane at the injection point is shown on the left picture. Details of a single parabola including a rough timescale can be seen in the drawing on the right.

A parabola starts when the pilot from a steady horizontal flight at maximum speed pulls up the airplane until the airplane is 47° nose up (*pull up phase*). In this pull up phase of about 20 seconds the gravitation experienced on board of the airplane is ~1.8 g (hyper gravity). Then, at the *injection point,* the pilot reduces the power of the engines in such a way that only the air resistance is compensated and brings the airplane into a free fall. The followed path in the air describes a parabola, and during this phase micro gravity (~0.01 g) is achieved on board. After this period of 20-25 seconds the pilot again pulls up the airplane to bring it in a horizontal flight again. During this *pull out phase* the experienced gravity on board is again ~1.8 g. This sequence is visualized in Figure 1.3.

PARABOLAS SEQUENCE
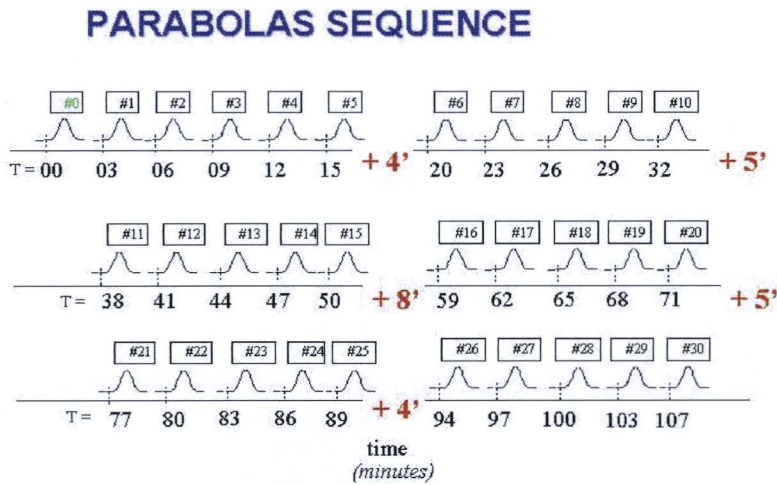
Figure 1.4: *The parabolic flight sequence. Note that every three minutes another parabola is started. After each five parabolas there is a small break, except with the first set of parabolas.*

Because the stabilization time for a metal halide lamp exceeds the 20 seconds of micro gravity offered [36], it is not possible to perform measurements on fully stabilized lamps within the PFC. The experiments in the ISS however do offer this feature. To be sure that useful measurements will be carried out in the ISS, the selected lamps and measurement strategy have to be tested under micro gravity conditions. The PFC is an excellent opportunity for doing this.

1.4 Scope and outline of report

The scope of this study consists of several issues. First of all, the problems encountered in previous 34th PFC [36] concerning measurement techniques and data processing afterwards have to be solved. Furthermore an extra experimental setup has been realized to take a closer look at the role of gravity on total visible light output of metal halide lamps. This in order to increase the understanding of the influence of changes in the additive density distribution on the lamp efficiency. This experiment is baptized the "*Parabolamp experiment*". The experience developed during the PFC's then has to be transferred to the final construction and settings of the ISS experiment.

Chapter 2 briefly explains why metal halide lamps suffer from axial segregation phenomena under 1 g circumstances. Furthermore the role of gravity on the complex processes in a metal halide lamp is discussed. Chapter 3 explains how spectroscopic measurements can be used to construct additive density distributions. A method for spectroscopic determination of the temperature profile of the discharge is introduced. In chapter 4 the Arges experimental setup used in the parabolic flights is presented. The selection of suitable emission lines to be measured and the chosen measurement plan for both the parabolic flights and the space mission is also treated. Chapter 5 deals with the design of the Parabolamp experiment and in chapter 6 the results of the parabolic flight measurements are presented. Because the main objective is developing a solid procedure for analyzing the spectroscopic data including programming some automatic

routines, one lamp is fully analyzed to prove the validation of this procedure. Subsequently, the Parabolamp data is analyzed and presented. Finally in chapter 7 the overall conclusions among with some recommendations will be offered.

Figure 1.5: *An impression of Arges team-members doing measurements in the zero-g plane during a micro gravity phase. Due to loss of gravitation the "Marsupilami" is floating. The experimenters cling to the airplane and the experiment to prevent "free floating", which for safety reasons is not allowed.*

2 The effect of diffusion and convection on metal halide lamps

In this chapter the effects of diffusion and convection on the discharge of metal halide lamps are treated qualitatively. A more extensive description of the resulting segregation phenomena can be found in [12], [9] and [3]. Furthermore the influence of gravity on both vertical and horizontally burning lamps is discussed.

2.1 Radial segregation

The discharge in a lamp consists of mainly mercury vapour and a small fraction of metal halide additives. For simplicity we consider a vertically burning metal halide lamp with just a dysprosium-iodide additive. As mentioned before, the temperature in the centre of the discharge is ~5500 K, and near the wall ~1200 K.
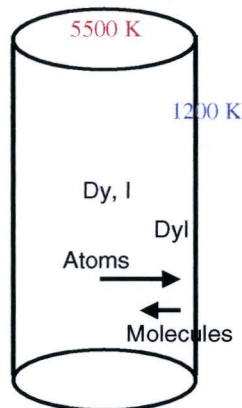
Figure 2.1: *A schematic drawing of a burner with the diffusion processes drawn.*

Because the chemical equilibrium of the additive (Eq. 2.1) is extremely temperature dependent, the majority of the DyI$_3$-molecules is dissociated into dysprosium and iodine atoms in the hot center of the discharge. In the relatively cold zone near the burner wall the atoms recombine again to DyI$_3$-molecules.

$$DyI_3 \Leftrightarrow Dy + 3I \qquad (2.1)$$

When we for a moment neglect convective gas flows, and consider the fact that the larger and heavier DyI$_3$-molecules diffuse much slower in the buffer gas [15] than the smaller and lighter dysprosium atoms, we see that more dysprosium atoms move towards the burner wall than DyI$_3$-molecules move toward the center of the discharge (Figure 2.1). The result is an equilibrium at which the partial pressure of Dy is lower in the center of the discharge than at the burner wall. This effect is called *radial segregation*.

2.2 Axial segregation

But, of course, a contained gas with the assumed large temperature gradients will show convective flows when situated in a gravitational field. Neglecting end effects, this convective flow, which is totally governed by the buffer gas in metal halide lamps, can be calculated using the Navier-Stokes equation for a cylindrical geometry:

$$\frac{\partial p}{\partial z} + \rho g - \frac{1}{r}\frac{\partial}{\partial r}(r\eta \frac{\partial v_z}{\partial r}) = 0 \qquad (2.2)$$

with boundary conditions

$$\frac{\partial v_z}{\partial r} = 0 \text{ at } r = 0, \qquad (2.3)$$

$$v_z = 0 \text{ at } r = R, \text{ and} \qquad (2.4)$$

$$\int_0^R \rho v r dr = 0, \qquad (2.5)$$

where r denotes the radial position, R the radius of the burner, p and ρ the buffer gas pressure and mass density, η the viscosity of the buffer gas, and v_z the axial velocity. Elenbaas [6] calculated the convection velocity as a function of the radius for a vertically burning high pressure mercury discharge using Eq. (2.2), assuming a parabolic temperature profile. The result of this calculation is shown in Figure 2.2. Following Elenbaas, the convection velocity on the axis of the discharge ($r = 0$) varies according to:

$$v_z \propto \frac{\rho_{Hg} R^2 g}{\eta}. \qquad (2.6)$$
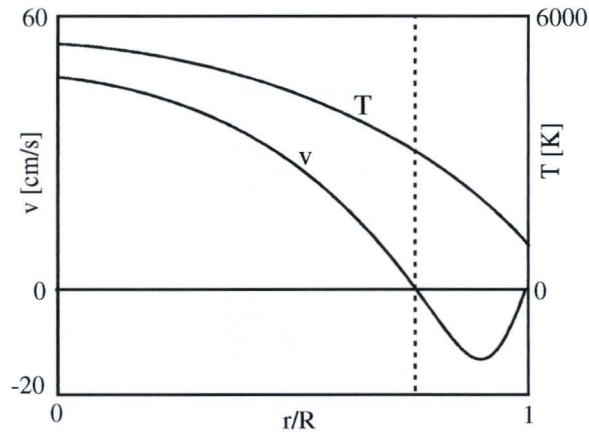
Figure 2.2: *A typical temperature and convection velocity distribution of a mercury lamp.*

In Figure 2.2 we see that the hot gas in the center of the discharge moves upwards, and that the relatively cold gas near the burner wall moves downwards. Apparently the hot gas in the center of the discharge moves up, reaches the top of the burner, cools down, and moves downwards along the burner wall. In section 2.1 we saw however that the partial pressure of atomic dysprosium in the center of the discharge is lower than near the wall. As a result the upward stream of buffer gas contains less atomic dysprosium than the stream going downwards. Consequently, as a result of this phenomenon, there is a net downward transport of dysprosium. In a steady state situation this is, however, not possible. An equilibrium establishes at which the density of atomic dysprosium at the top of the discharge is lower than in the lower part of the discharge. In this way the diffusive axial transport cancels the net downward transport of dysprosium caused by radial diffusion and convection. This is called *axial segregation*.

This axial segregation has an important negative effect on the lamp performance. First of all, due to the lack of dysprosium in the upper part of the burner, less radiation is emitted from the dysprosium in that part of the lamp. As a result, *color separation* emergences: the color of the light originating from the upper part of the burner has a different color that the light emitted at the lower part. An example of a burning lamp suffering from color separation is shown in Figure 2.3.

Another negative effect of axial segregation is the loss of efficiency. Due to the deficiency of the radiating species in the upper part of the burner, the overall efficiency of the lamp decreases. This is, of course, a serious unwanted effect.
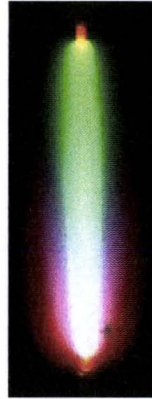
Figure 2.3: *A photograph of a vertically burning quartz burner with 10.00 mg Hg and a Dyl additive. The color separation due to axial segregation of the additive is clearly visible.*

2.3   Axial segregation vs. gravity: the Fischer curve

In order to be able to quantify the amount of axial segregation, Fischer [7] introduced the *segregation parameter* λ:

$$\lambda = -\frac{1}{n_x}\frac{dn_x}{dz}.$$

(2.7)

Here n_x represents the atomic additive density, in our case atomic Dy. Geijtenbeek [9] showed that in first order approximation, this segregation parameter is constant as a function of z.

Fischer also presented the a curve (Figure 2.4), showing the relation between the buffer gas pressure p_0 and the segregation parameter λ, which we refer to as the *Fischer curve*.
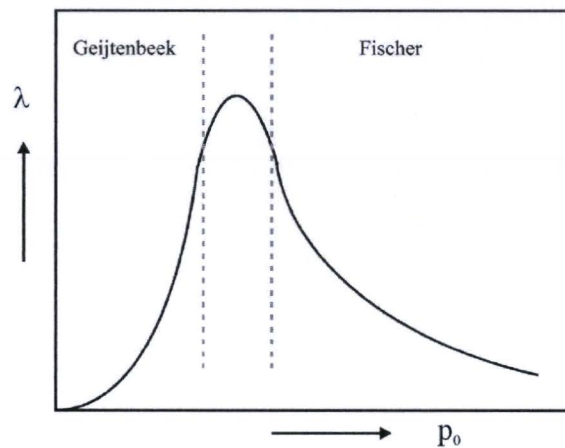
Figure 2.4: *The Fischer curve showing the segregation parameter λ as a function of the buffer gas pressure p_0.*

If we look at the Fischer curve, we can distinguish two regions. One located to the left and one located to the right of the dotted lines drawn in Figure 2.4. If the buffer gas pressure is very small (left side of the curve), we see (Eq. 2.6) that the convection velocity is also very small. As a result, the diffusive effects are dominant over the convective effects and only radial segregation manifests, while axial segregation is very small. When then the convection velocity is increased (by increasing the buffer gas pressure) axial segregation arises, because the convective flow drags the radially segregated additive along. Geijtenbeek [9] has shown that the dependence of the segregation parameter in this region is:

$$\lambda \propto v_z \cdot p_{Hg} \left(\frac{1}{D_M^*} - \frac{1}{D_A^*} \right),$$

(2.8)

where D_M^* and D_A^* denote the state independent relative diffusion coefficients of the molecules and atoms respectively, calculated using the hard sphere model [15].

However, at some point, increasing the buffer gas pressure does not lead to more axial segregation. At the top of the curve the convective gas flow starts "mixing" the buffer gas en hence reducing the radial segregation. This results in a decrease of axial segregation. When the convection velocity is increased even more, the radial segregation can be canceled out almost completely. Following Fischer [7], the dependence of the segregation parameter in this region is:

$$\lambda \propto \frac{1}{p_{Hg}^2 R^2 g}.$$

(2.9)

Combining these two results, we see that if a lamp with little axial segregation is desired, two options are available. A low buffer gas pressure combined with a small burner radius, and a high buffer gas pressure combined with a large burner radius will both result in little or negligible axial segregation, and therefore little color separation and loss of efficiency.

2.4 Arc bending

Unlike the previous paragraphs, we will now consider a horizontally burning metal halide lamp. When a horizontally burning lamp is situated in a gravitational field, again convective flows arise, due to the large temperature gradients present in a burning lamp. The hot gas in the center of the discharge moves up until it reaches the burner wall, cools down, and moves downwards along the relatively cold burner wall. This process is visualized in Figure 2.5. As a result of the upward gas flow in the hot center of the discharge, the discharge is pushed towards the upper burner wall. A curved discharge like shown in Figure 2.5 is the consequence. This phenomenon is called *arc bending*, and in fact holds the origin of the word *arc*.
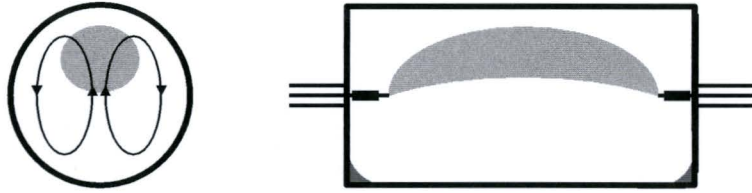
Figure 2.5: *A schematic drawing of the discharge in a horizontally burning lamp. Due to convection the discharge is pushed to the upper burner wall. The result is an curved discharge. Note that in a horizontally burning lamp usually two salt pools are present.*

Because the middle of the discharge is now much closer to the burner wall than in vertical operation, larger temperature gradients exist. This results in a higher heat flow from the discharge to the upper burner wall and thus creating an extra energy loss. To investigate the influence of arc bending on the lamp efficiency, Weerdesteijn [41] performed experiments on horizontally burning lamps without and with arc straightening by means of applying an external magnetic field. Weerdesteijn measured losses in lamp efficiency of about 1.5 − 6.5 % due to arc bending, depending on burner diameter and buffer gas pressure. The effect of the convection flow reducing the radial segregation is discussed in the next paragraph.

2.5   Light output vs. gravity

In order to get more insight in the processes in a metal halide lamp while varying gravitation, we try to combine the effects described in the previous paragraphs. For now, we are only interested in the first order effects, so we assume that during the gravity transitions the temperature of the salt pool remains unchanged. This implies that the molecular additive pressure in the vicinity of the salt pool is constant:

$$\frac{dP_M}{dt} = 0, \tag{2.10}$$

Furthermore the effect of arc bending on the light output is not taken into account, and for simplicity we will assume that the amount of atomic additive present in the discharge is proportional to the total visible light output of the lamp. (In practice this is not true, but in this qualitative analysis we will assume this to be the case).

First, let's consider a horizontally burning metal halide lamp. When the gravity is very strong, the additive is totally mixed due to the high convection velocity of the buffer gas and therefore the elemental pressure of the additive is equal to the elemental pressure above the salt pool. For this situation we normalize the atomic additive pressure:

$$\frac{\left(P_A\right)_{mixed}}{P_M} = 1. \tag{2.11}$$

On the other hand, in the situation without gravity ($g=0$), there is no convection-driven mixing of the additives and therefore radial segregation arises. For this case Geijtenbeek [9] determined that the normalized atomic additive pressure can be estimated by:

$$\frac{P_A}{P_M} = \frac{D_M^*}{D_A^*}.$$

(2.12)

For Dy, Ce and Na the ratio of these relative diffusion coefficients of the molecules and atoms is approximately 0.3. This is visualized by the light blue line in Figure 2.6. The shape of this line is however not exactly known, so this line has to be seen as a trend line. Note that because we assumed that the amount of atomic additive present in the discharge is proportional to total visible light output, the y-axis corresponds to the visible light output of a lamp.
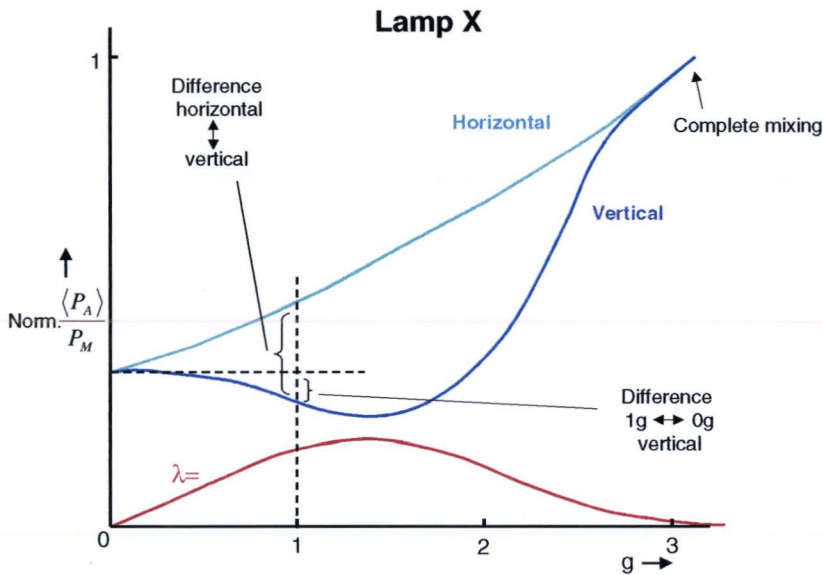
Figure 2.6: *A sketch of the effects of radial and axial segregation on the amount of atomic additive in the discharge of a both horizontally and vertically burning lamp. The amount of atomic additive in the discharge is approximately proportional to the visible light output of a lamp. The segregation parameter λ as a function of g is also drawn in red. In this analysis the salt pool temperature is assumed to be constant.*

Now we consider a vertically burning lamp. The combination of radial diffusion and convection causes axial segregation for some values of *g*. The axial segregation parameter λ for lamp X is drawn in Figure 2.6, and varies according to Eq. (2.8) and (2.9). For high values of *g* the convective flow again mixes the additives, and for $g=0$ only radial segregation exists. Due to axial segregation the geometrical averaged atomic additive pressure in the discharge $<P_A>$ is lowered in comparison with the horizontal situation. This is also visualized in Figure 2.6 by the dark blue line.

We can also see, in first order approximation, that the efficiency of a horizontally burning lamp is always higher in comparison with a vertically burning lamp. This is however without the effect of energy losses due to arc bending, and these effect are proven to be not negligible. Without the effect of arc bending we subsequently see that the light output of a horizontally burning lamp in *0g* is always lower than with higher *g* values. In practice, however, arc bending always manifests in a horizontally burning lamps in the presence of a gravitational field.

However, the amount of radial and axial segregation in a lamp is fully determined by its burner geometry, buffer gas pressure and the additive used. As a result the graph of the axial segregation λ as a function of gravity for an other type of lamp can differ much from the one visualized in Fig. 2.6. Consequently, the changes of the light output of those two lamps when going from a *1g* to a *0g* situation can be rather different. An example for an other type of lamp Y is given in Fig. 2.7. Surprisingly, we see that the light output of a vertically burning lamp X becomes larger when going from *1g* to *0g*, whereas the light output of a vertically burning lamp Y becomes smaller.
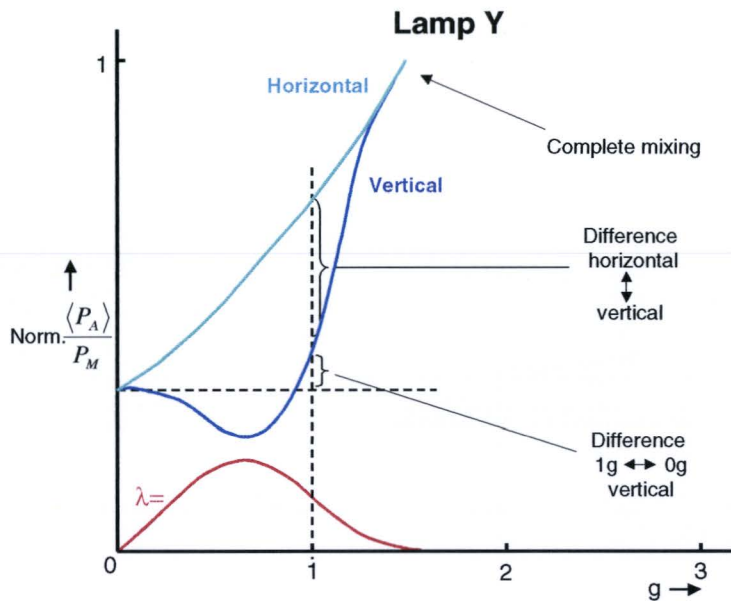
Figure 2.7: *A sketch of the effects of radial and axial segregation on the amount of atomic additive in the discharge of lamp Y. Due to the different behavior of the axial segregation parameter as a function of gravity, the light output as a function of gravity of lamp Y differs much from lamp X, visualized in Fig. 2.6.*

The Parabolamp experiment (Chapter 5) is designed to investigate the processes and assumptions described above. By attending the parabolic flight campaign, the unique possibility is given to do experiments under varying gravity situations, while keeping the buffer gas pressure and burner geometry constant. The original idea for performing these kind of experiments was generated by J.J.F. Geijtenbeek, Philips Lighting CDL.

3 Spectroscopic method to determine radial density profiles

This chapter describes the method to determine radial additive density profiles from spectroscopic emission measurements. For that, a procedure is presented to calculate temperature profiles from calibrated measurements of an optically thin Hg emission line.

3.1 Spontaneous emission of radiation

Spectroscopic methods used to measure atomic densities are based on spontaneous emission of radiation. For the plasmas in high pressure metal halide lamps we can assume Local Thermal Equilibrium (LTE) [25]. This implies that the same temperature applies for all particles in the plasma and that the excited-state distribution of atoms is governed by the Boltzmann formula. If no absorption of radiation takes place, the *radiant power* U_{rad} *[Wm^{-3}]* of a single spectral line per unit volume is:

$$U_{rad} = Ah\nu n_{up} = Ah\nu \frac{p_x}{kT} \frac{g_{up}}{Q(T)} \exp(-E_{up} / kT).$$
(3.1)

Here *A* denotes the transition probability of considered transition, $h\nu$ the energy of the emitted photon, and n_{up} the density of atoms occupying the upper energy state. $p_x = n_x kT$ represents the local partial pressure of the atomic species, with *T* the temperature and *k* the Boltzmann constant. $g_{up} = 2J_{up} + 1$ is the statistical weight of the upper energy state of the considered transition. *Q(T)* is the *partition function* and holds the energy-weighted sum over all energy levels of the considered species:

$$Q(T) = \sum_i g_i \exp(-E_i / kT).$$
(3.2)

The values of the partition function can be found on the internet for almost every element [23], as well as many transition probabilities and other spectroscopic data [32].

3.2 Optical thickness of a spectral line

Because we want to calculate radial additive density profiles from the measurement of the intensity of emission lines, we have to make sure that light emitted from the center of the discharge is not reabsorbed by the plasma, before leaving the plasma. It is necessary to estimate the amount absorption of light from an emission line before leaving the plasma. For that, the *optical thickness* τ_0 of a spectral line is examined. The optical thickness τ_0 can be estimated using [28]:

$$\tau_0 = 1.06 \cdot 10^{-5} \frac{\langle n_x \rangle R_{eff} \, f g_{low} \exp(-E_{low} / kT)}{Q(T)\pi\delta\nu},$$

(3.3)

where R_{eff} is the effective radius of the channel, $<n_x>$ the average species density, and T the effective temperature. The oscillator strength f can be calculated using

$$f = A \frac{g_{up}}{g_{low}} \cdot 1.499 \cdot 10^{-14} \lambda^2$$

(3.4)

with λ the wavelength of the emitted photon in nm. $\delta\nu$ is the spectral line width and can be calculated with the Full Width at Half Maximum (FWHM) $\delta\lambda$ of the emission line using

$$\delta\nu = \frac{c}{\lambda^2} \delta\lambda,$$

(3.5)

where c represents the speed of light.

A spectral line is considered to be optically thin if τ_0 is small ($\tau_0 \leq 1$). In that case a neglectable part of the radiation is absorbed before leaving the plasma.

3.3 Line broadening

For determination of the emission line intensity, we will use an automatic fitting procedure. To choose the right fitting procedure, the different line broadening effects are discussed in this paragraph.

The line width of an atomic emission line is determined by its natural line width, Doppler and pressure broadening effects [31]. In HID lamps, the major source of line broadening is pressure broadening. Pressure broadening is caused by the interaction of the radiating atom with the surrounding particles. Pressure broadening can be divided into three types of broadening mechanisms, i.e. resonance broadening, Stark broadening and VanderWaals broadening. Resonance broadening is caused by the interaction of the radiating atom with other atoms of the same species that are in the

ground state. Stark broadening arises due to the interaction of the radiating atom with electrical fields and/or charges particles, like electrons and ions, and VanderWaals broadening is caused by the interactions between the radiating atom and atoms of a different species that are in the vicinity.

Resonance and Stark broadening both result in a Lorentz shaped line profile

$$I_{\lambda, Lorentz} = \frac{2I_0}{\pi} \frac{w}{4(\lambda - \lambda_c)^2 + w^2},$$
(3.6)

where I_0 is the intensity of an emission line with wavelength λ_c and FWHM w.

The emission lines of dysprosium and cerium are only weakly broadened by VanderWaals broadening, and their line profiles can be described excellently by a Lorentz shaped line profile [31].

3.4   **Conservation of the lateral position**

In order to determine how the spatially resolved measurements are influenced by the fact that the plasma is contained in a cylindrical shaped quartz burner with relatively thick walls, we have to calculate how the distance y_0 in Figure 3.1 is related to distance y^*.
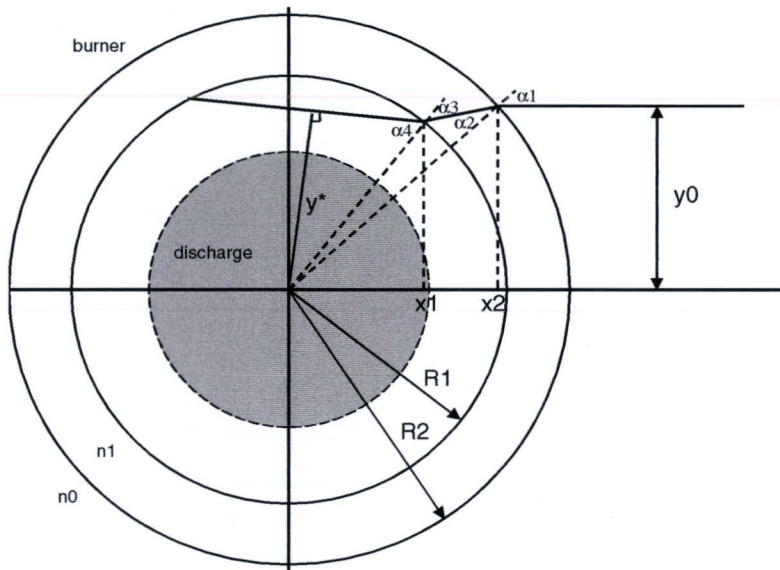
Figure 3.1: *The propagation of a ray of light through the burner wall.*

The refraction of a ray of light is given by the Snell's law:

$$n_i \sin \alpha_i = n_t \sin \alpha_t$$
(3.7)

with α_i the angle of incidence in a medium with refractive index n_i, and α_t the angle of the transmitted light in a medium with refractive index n_t.

Following the definitions given in Fig. 3.1, we can see that

$$\alpha_1 = \arcsin\left(\frac{y_0}{R_2}\right),$$ (3.8)

and with Snell's law:

$$\alpha_2 = \arcsin\left(\frac{y_0}{R_2}\frac{n_0}{n_1}\right).$$ (3.9)

The formula for the line between x_1 and x_2 is given by:

$$y = \tan(\alpha_1 - \alpha_2)\cdot x + c_1,$$ (3.10)

with c_1 given by:

$$c_1 = -\tan(\alpha_1 - \alpha_2)\cdot x_2 + y_0,$$ (3.11)

where x_2 can be calculated using the formula for a circle:

$$x_2 = \sqrt{R_2^2 - y_0^2}.$$ (3.12)

The value of x_1 can then be calculated by solving the equality of the formula of the circle with radius R_1 and the expression given by Eq. (3.10):

$$\tan(\alpha_1 - \alpha_2)\cdot x_1 + c_1 = \sqrt{R_1^2 - x_1^2}.$$ (3.13)

This expression can be solved for x_1 by using the abc formula:

$$x_1 = \frac{-2c_1\tan(\alpha_1 - \alpha_2) + \sqrt{[2c_1\tan(\alpha_1 - \alpha_2)]^2 - 4\{[\tan(\alpha_1 - \alpha_2)]^2 + 1\}\cdot -R_1^2 c_1^2}}{2\{[\tan(\alpha_1 - \alpha_2)]^2 + 1\}}$$ (3.14)

Subsequently, we can calculate α_3 using:

$$\alpha_3 = \arccos\left(\frac{x_1}{R_1}\right) - (\alpha_1 - \alpha_2).$$ (3.15)

For y^* counts with the use of Snell's law:

$$y^* = R_1 \sin(\alpha_4) = R_1 \frac{n_1}{n_0} \sin(\alpha_3). \tag{3.16}$$

A numerical calculation of y^* for arbitrary values of R_1, R_2, n_0, n_1 and y_0 gives the values showed in Table 3.1. Calculations with other values of R_1, R_2, n_0, n_1 and y_0 show that $y_0=y^*$ under all circumstances.

y0 (mm)	x2 (mm)	α1 (deg)	α2 (deg)	c1 (mm)	x1 (mm)	α3 (deg)	α4 (deg)	y* (mm)
0.00	5.00	0.00	0.00	0.00	4.00	0.00	0.00	0.00
0.50	4.97	5.74	3.93	0.34	3.97	4.91	7.18	0.50
1.00	4.90	11.54	7.87	0.69	3.89	9.86	14.48	1.00
1.50	4.77	17.46	11.86	1.03	3.75	14.88	22.02	1.50
2.00	4.58	23.58	15.90	1.38	3.54	20.03	30.00	2.00
2.50	4.33	30.00	20.03	1.74	3.26	25.35	38.68	2.50
3.00	4.00	36.87	24.27	2.11	2.90	30.91	48.59	3.00
3.50	3.57	44.43	28.65	2.49	2.43	36.82	61.04	3.50
4.00	3.00	53.13	33.23	2.91	1.81	43.23	90.00	4.00

Table 3.1: *Calculation of y^*, using the following values: $n_0=1.00$, $n_1=1.46$, $R_1=4.00$ mm, $R_2=5.00$ mm. However, under all circumstances, y^* will be equal to y_0.*

We see that the burner only slightly rotates the beam. However, since we assume cylindrical symmetry for the plasma under study, this has no influence.

3.5 The Abel inversion technique

When investigating a radiating plasma with spectroscopic emission measurements, one always measures the side-on emission intensity of the spectral lines. The measured intensity is a result of the integrated intensities along the *line-of-sight* from y_0 ($= \sqrt{R^2 - x^2}$) to $-y_0$, following the definitions shown in Figure 3.2. For optically thin lines a common used method to extract radial information from a set of lateral measurements is the *Abel inversion technique*.
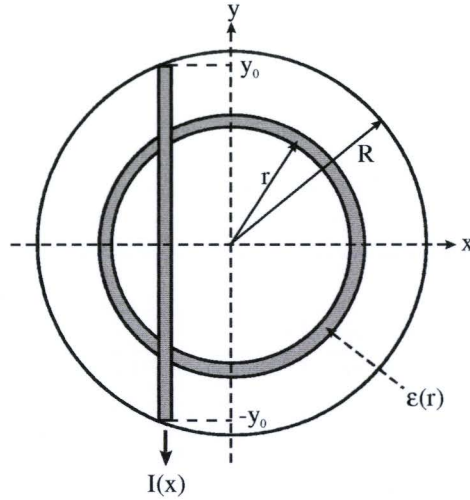
Figure 3.2: *Cross-section of the burner.*

When cylindrical symmetry of the plasma is assumed, the measured lateral *emission line intensity I(x) [Wm^{-2}sr^{-1}]* is given by:

$$I(x) = \frac{1}{4\pi} \int_{-y_0}^{y_0} \varepsilon(x, y)dy = \frac{2}{4\pi} \int_{0}^{y_0} \varepsilon(x, y)dy, \quad (3.17)$$

where $\varepsilon(x,y)$ denotes the emission line intensity emitted at position (x,y) in the plasma per unit volume. In the cylindrically symmetric case where $\varepsilon=\varepsilon(r)$ and when x is constant, $I(x)$ can be rewritten as:

$$I(x) = \frac{2}{4\pi} \int_{y=0}^{y=y_0} \varepsilon(r)\frac{dy}{dr} dr = \frac{2}{4\pi} \int_{x}^{R} \varepsilon(r)\frac{r}{\sqrt{r^2 - x^2}} dr. \quad (3.18)$$

This expression shows the relation between emission intensity $\varepsilon(r)$ and the measured lateral intensity $I(x)$. However, often only a discrete set of lateral emission measurements is available. To calculate the according $\varepsilon(r)$ the Abel inversion can be performed in different ways, i.e. numerical, analytical and direct. A previous study [36] has demonstrated that the analytical method described below is most suitable to calculate $\varepsilon(r)$ in our case.

The foreseen emission profile can be approximated very well by a 6th order polynomial function:

$$\varepsilon(r) = \sum_{n=0}^{6} c_n r^n . \quad (3.19)$$

Because we are only using positive values of radius r, the odd fitting coefficients can also be used in the fitting process. The behaviour of the fitting function for negative r is irrelevant.

The substitution of this expression in the Abel transformation integral (Eq. 3.18) gives:

$$I(x) = \frac{2}{4\pi} \sum_{n=0}^{6} c_n \int_x^R \frac{r^n \cdot r}{\sqrt{r^2 - x^2}} dr .$$
(3.20)

Calculating Eq. (3.20) for n from zero through six gives the following expression :

$$4\pi \cdot I(x) = c_0 2\sqrt{R^2 - x^2} +$$
$$c_1 \left[R\sqrt{R^2 - x^2} + x^2 \ln\left(R + \sqrt{R^2 - x^2}\right) - x^2 \ln(y) \right] +$$
$$c_2 2\sqrt{R^2 - x^2} \left(\frac{1}{3}R^2 + \frac{2}{3}x^2 \right) +$$
$$c_3 \left\{ \frac{1}{2}\sqrt{R^2 - x^2} \left(R^3 + \frac{3}{2}x^2 R \right) + \frac{3}{4}x^4 \left[\ln\left(R + \sqrt{R^2 - x^2}\right) - \ln(x) \right] \right\} +$$
$$c_4 \frac{2}{5}\sqrt{R^2 - x^2} \left(R^4 + \frac{4}{3}x^2 R^2 + \frac{8}{3}x^4 \right) +$$
$$c_5 \left\{ \sqrt{R^2 - x^2} \left(\frac{1}{3}R^5 + \frac{5}{12}x^2 R^3 + \frac{5}{8}x^4 R \right) + \frac{5}{8}x^6 \left[\ln\left(R + \sqrt{R^2 - x^2}\right) - \ln(x) \right] \right\} +$$
$$c_6 2\sqrt{R^2 - x^2} \left(\frac{1}{7}R^6 + \frac{6}{35}x^2 R^4 + \frac{8}{35}x^4 R^2 + \frac{16}{35}x^6 \right) .$$
(3.21)

In this expression the measured lateral intensity $I(x)$ is a function of the lateral position x, the burner radius R and the coefficients c_0 through c_6. This equation can be fitted to the measured lateral intensity data points by varying the coefficients c_0 through c_6 with a Levenberg-Marquardt least square method [39]. Because the natural logarithm used in Eq. (3.21) has no value for $x \leq 0$, the measured lateral intensity profile has to be mirrored around the centre of the discharge. Next only the averaged positive data points are used in the fitting procedure.

The following boundary conditions are used in the fitting procedure:

$$\frac{d}{dr}\varepsilon(0) = 0 ,$$
(3.22a)
$$\varepsilon(R) = 0 .$$
(3.22b)

The first boundary condition (Eq. 3.22a) is used to ascertain that $\varepsilon(r)$ has no sharp edge the centre of the discharge, which would be physically inaccurate. As a result the

fitting coefficient c_1 has to be set to zero. The second boundary condition (Eq. 3.22b) is used to make sure that no light originates from the burner wall.

3.6 Method to determine radial temperature profiles

In order to calculate the radial additive density profiles with Eq. (3.1), the temperature profile $T(r)$ has to be known. In this paragraph a method is presented to calculate the temperature of the plasma using the absolute intensity of an optically thin mercury emission line. Because the buffer gas does not suffer from segregation phenomena, mercury emission lines can be used for temperature determination. In section 4.3 it will be shown that the optically thin 579.06 nm Hg line is detectable with our spectrometer and suitable for this method. This method is presented because a previous study [36] showed that the *Boltzmann plot* method [3] is unsuitable for calculating the temperature of the considered plasma. When using the Boltzmann plot method, the plasma temperature is calculated using the ratio of two optically thin salt additive emission lines separated by only a small wavelength difference $\Delta\lambda$ (<~1 nm), but with a large difference in upper energy level. With the use of the Boltzmann formula, the according temperature can then be calculated. However, when only using two emission lines for this calculation, this method is very sensitive for errors in the measured line intensity and in the used transition probabilities.

For clarity, the following definitions [11] and their dimensions, following figure 3.2, are given:

- Spectral emission coefficient: $\varepsilon_\lambda(r)$, $[Wm^{-3}nm^{-1}]$ (3.23)

- Radiant power: $U(r)_{rad,579} = \int\limits_{579-\delta}^{579+\delta} \varepsilon_\lambda(r)d\lambda$, $[Wm^{-3}]$ (3.24)

- Spectral radiance: $L_\lambda = \int\limits_{-y_0}^{y_0} \frac{\varepsilon_\lambda(r)}{4\pi}dy$, $[Wm^{-2}sr^{-1}nm^{-1}]$ (3.25)

where δ is taken to be large enough to enclose the whole 579 nm emission line in the integration of Eq. (3.24). The lateral line intensity $I_{579}(x)$ $[Wm^{-2}sr^{-1}]$ of the 579 nm Hg line is then given by:

$$I_{579}(x) = \int\limits_{579-\delta}^{579+\delta} L_\lambda(x)d\lambda = \int\limits_{579-\delta}^{579+\delta} \int\limits_{-y_0}^{y_0} \frac{\varepsilon_\lambda(r)}{4\pi}dyd\lambda = \int\limits_{-y_0}^{y_0} \frac{U_{rad,579}(x,y)}{4\pi}dy. \quad (3.26)$$

In general, measurements of emission lines are executed with a spectrometer with a photosensitive CCD-area. In section 4.2 it will be shown that a 1:1 image of the cross-section of the middle of the burner is formed on the CCD of our spectrometer. Pixel column n corresponds to a certain wavelength λ, whereas pixel row k corresponds to a certain lateral position in the burner. With the use of a specially developed fitting routine fit579.ogs (Appendix A.III), the area under the emission line $A_{Lorentz}(k)$ can be

determined, using a Lorentz-fit procedure (see Eq. (3.6)). If the Lorentz-fit exactly describes the measurement data, for $A_{Lorentz}(k)$ applies:

$$A_{Lorentz}(k) = \sum_{n=500-\Delta}^{500+\Delta} C(n,k) - C_0(k), \qquad (3.27)$$

with $C(n,k)$ the measured counts per pixel, with a certain shutter time $t_{shutter}$, $C_0(k)$ the background counts per pixel row k due to a small amount of continuous line radiation (a dark background measurement has already been subtracted), and Δ large enough to enclose the total 579 nm emission line. This continuous line radiation is probably caused by not resolved rare earth radiation, Bremstrahlung and recombination radiation. The Lorentz fit procedure automatically determines the value of $C_0(k)$. In practice, the fitted Lorentz profile does not exactly describes the measurement data, but the area under the Lorentz fit will be in very good agreement with the area under the measured data points. An example of a Lorentz fit is shown in Figure 3.3.
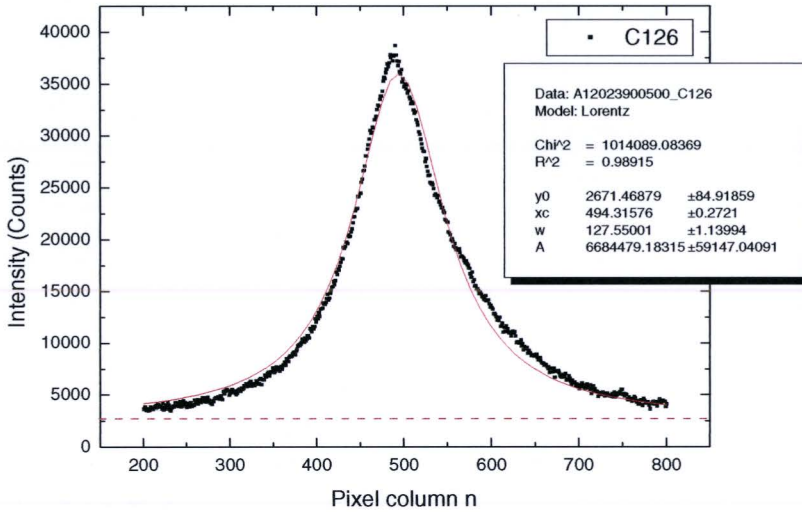
Figure 3.3: *Example of a Lorentz fit of the 579 nm Hg emission line. The small asymmetry of the emission line is possibly due to Stark shift. The fit parameter y0 is equal to the background counts per pixel row $c_0(k)$ and is visualized by the dashed red line.*

In order to calculate absolute lateral line intensities from the measured intensities in counts, a conversion parameter β is introduced:

$$\beta = \frac{L_\lambda \cdot \Delta\lambda_{pixel} \cdot t_{shutter}}{C(n,k)}, \qquad (3.28)$$

where $\Delta\lambda_{pixel}$ denotes the spectral range of one single pixel, calculated by:

$$\Delta\lambda_{pixel} = \frac{Spectral\_range\_CCD}{N_{pixelcolumnns}},$$ (3.29)

with $N_{pixelcolumns}$ the total number of pixel columns of the used CCD. The unit of the conversion parameter β is *[counts^{-1}·s·W·m^{-2}·sr^{-1}]*, and the value of β can be determined by calibrating the spectrometer with a lamp with an exact known spectral radiance. Note that β is dependent of the used optical system.

Then, according to Eq. (3.26), (3.27) and (3.28), the absolute lateral line intensity $I_{579}(k)$ at pixel row k can be calculated with:

$$I_{579}(k) = \int_{579-\delta}^{579+\delta} L_\lambda(k)d\lambda$$ (3.30a)

$$= \frac{\beta}{\Delta\lambda_{pixel} \cdot t_{shutter}} \cdot \sum_{n=500-\Delta}^{500+\Delta}(C(n,k)-C_0(k))\Delta\lambda_{pixel}$$ (3.30b)

$$= \frac{\beta}{t_{shutter}} \cdot A_{Lorentz}(k).$$ (3.30c)

To determine the absolute lateral line intensity $I_{579}(x)$ as a function of the lateral position x in mm, instead of pixel row k, the following coordinate transition has to take place:

$$x = (k-k_0) \cdot \Delta x_{pixel},$$ (3.31)

with

$$A_{Lorentz}(k_0) = \max(A_{Lorentz}(k)),$$ (3.32)

and Δx_{pixel} the corresponding spatial range of one single pixel, or more pixels, when binning of pixels is applied. Because the maximum line intensity of the 579 nm Hg line is situated in the hot center of the discharge, Eq. (3.32) relates the center of the discharge to pixel row k_0.

Now we are able to calculate the absolute line intensity $I_{579}(x)$ as a function of the lateral position for any measured lamp. In order to derive the radiant power $U_{rad,579}(r)$ as a function of the radius from a set of lateral line intensity measurements, the Abel inversion technique, as described in the previous section, is used:

$$U_{rad,579}(r) = \frac{1}{10^{-3}} \cdot AbelInversion(4\pi \cdot I_{579}(x))$$ (3.33a)

$$= \frac{\beta}{10^{-3} \cdot t_{shutter}} \cdot AbelInversion(4\pi \cdot A_{Lorentz}(x)),$$ (3.33b)

The factor 10^{-3} is introduced to compensate for the fact that the lateral position x is given in mm, and the radiant power is given in SI units. Note that due to the nature of the Abel inversion the dimension of this factor is $[m^{-1}]$.

Subsequently, with the use of Eq. (3.1) and the calculated radiant power $U_{rad,579}(r)$ from Eq. (3.33b), we are able to calculate the according temperature of the plasma. The data available [29] for the considered transition is given in Table 3.2. The partition function $Q(T)$ for mercury equals 1 for temperatures below 10000 K, which is the range of interest for the plasma under study.

λ (nm)	E_{up} (eV)	E_{low} (eV)	J_{up}	J_{low}	A (s^{-1})	f	τ_0
579.07	8.845	6.704	2	1	$2.04 \cdot 10^8$	1.71	0.00

Table 3.2: *Spectroscopic data of the 579 nm Hg emission line.*

The optical thickness τ_0 of this emission line is calculated with Eq. (3.3) to show that the use of Eq. (3.1) is allowed, i.e. that the considered emission line is optically thin. The following assumptions are used for the calculation of the optical thickness τ_0:

- $<n> = 2.5 \cdot 10^{25}$ m^{-3}
- $R_{eff} = 2$ mm
- $\delta v = 580$ GHz
- $T = 3000$ K

The average density $<n>$ is calculated with a mercury dose of 10 mg present in the used burner volume. The line width δv is known from high resolution spectra.

The pressure of the mercury gas p_{Hg}, used in Eq. (3.1), can be calculated by using the ideal gas law:

$$p_{Hg} = \frac{n_{Hg} k T_{eff}}{V} = \frac{m_{Hg} N_A k T_{eff}}{200.6 \cdot \pi R^2 h},$$

(3.34)

with n_{Hg} the total number of mercury atoms present in the discharge, m_{Hg} the effective mercury dose in the discharge in grams, and R and h respectively the radius and the height of the burner. T_{eff} represents the effective temperature and can be calculated using:

$$T_{eff} = \frac{p_{Hg} V}{n_{Hg} k}.$$

(3.35)

This expression can with

$$n_{Hg} = \int \frac{n_{Hg}}{V} dV = \frac{p_{Hg}}{k} \int \frac{1}{T(r)} dV \qquad (3.36)$$

be written as

$$T_{eff} = \frac{V}{\int \frac{1}{T(r)} dV} = \frac{R^2}{2 \int_0^R \frac{r}{T(r)} dr}, \qquad (3.37)$$

for our cylindrical shaped burner volume.

Now we know all the parameters used in Eq. 3.1, except of course the temperature profile $T(r)$ and as a result T_{eff}. So at first, we assume $T_{eff} = 3000$ K, and calculate $T(r)$. However, Eq. 3.1 is not analytically solvable for the temperature. Consequently a numerical calculation has to be carried out to calculate the plasma temperature $T(r)$ from a given set of $U_{rad,579}(r)$ values. Subsequently a new effective temperature T_{eff} can be calculated, and with this T_{eff} a new temperature profile $T(r)$ can be computed. This iteration is repeated several times until the difference in the calculated T_{eff} is small enough. We now have a plasma temperature profile $T(r)$, calculated from the calibrated measured intensity of an optically thin mercury emission line.

3.7 Construction of radial density profiles

With the temperature profile of the discharge known, the additive density profile can be calculated using:

$$n_{Dy}(r) = \frac{U_{rad}(r)}{g_{up} A h \nu} \frac{Q_{Dy}(T(r))}{\exp(-E_{up}/kT(r))}, \qquad (3.38)$$

with $U_{rad}(r)$ the measured intensity profile of an optically thin dysprosium emission line.

4 The ARGES experiment

In this chapter the ARGES measurement setup is presented, which is originally developed as a prototype for the final space experiment. The integrated Echelle-type emission spectrometer is discussed in more detail in section 4.2. Furthermore the total measurement plan is presented as well as the solving of some problems encountered during the previous parabolic flight campaign (PFC) in April 2003.

4.1 Integrated diagnostics

In order to investigate the radial additive density profiles, the axial segregation and the helical instabilities [16] under micro gravity conditions, a measurement setup has been developed containing three types of diagnostics. A high resolution spectrometer, a laser absorption spectroscopy setup and a digital color camera system are successfully integrated into one robust and very compact measurement system [36][1]. This because the requirements for experiments operated in the ISS are extremely high, and one of the main requirements concerns the weight and size of the experiment. The resulting optical measurement setup is schematically visualized in Fig. 4.1. The density distribution of the radiating excited atom can be calculated (assuming LTE) with the emission measurements of the spectrometer, while the aim of the laser absorption setup is to directly measure density distributions of the atoms in the ground state. The combined results of these two measurement techniques can give information about the chemical and physical processes inside the plasma. However, the problems encountered during the previous PFC concerning the laser absorption setup, among with some other technical difficulties and weight limitations, caused this diagnostic technique to be removed from the final space version of the experiment. Results obtained with the laser absorption technique during the PFC are expected to be presented in [26].

In the ARGES setup, twenty lamps are placed in a carrousel, that can put one of these lamps in the measurement position, indicated by number (4) in Fig. 4.1. When a lamp is in the measurement position, all three diagnostics can examine the lamp. The spectrometer and the laser absorption system, however, perform measurements alternating, to prevent the laser light from disturbing the spectroscopic measurement.

1) diode laser
2) lens laser setup
3) colour camera
4) experiment lamp
5) beamsplitter
6) lens emission setup
7) mirror
8) filter wheel
9) entrance slit
10) Echelle grating
11) interference filter
12) diode array
13) CCD camera
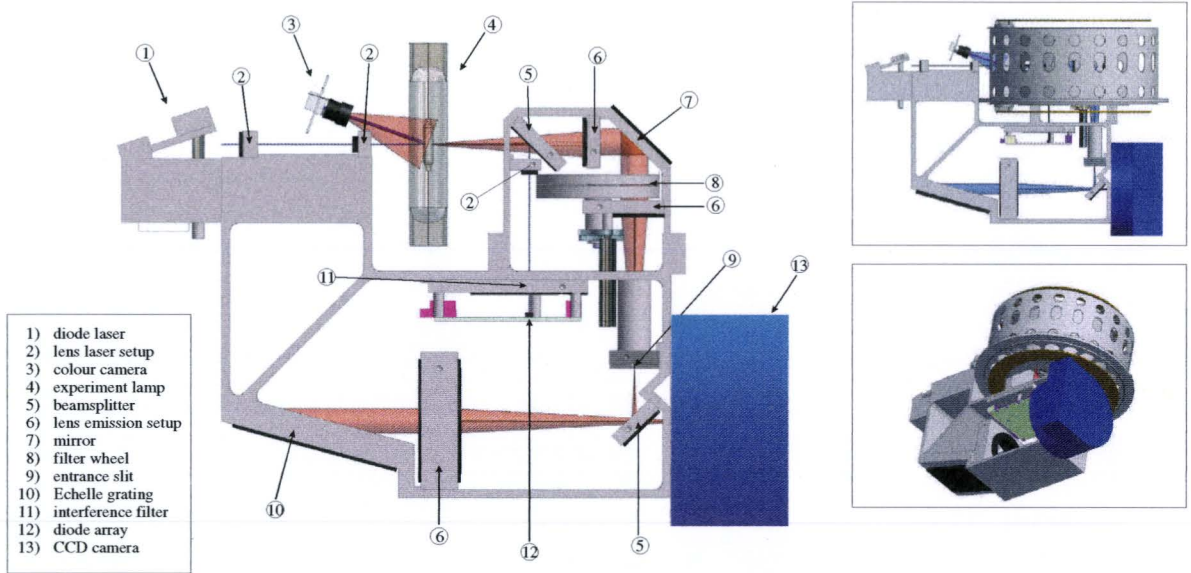
Figure 4.1: *Schematic drawing of the optical frame containing the spectrometer, the laser absorption setup and the camera observation. The insets show the frame including the lamp carrousel.*

The images produced by the digital color camera are used to confirm the burning of the lamp in the measurement position and to see the qualitative effects of axial de-mixing in the different gravitational situations during a parabolic flight. For the study of the helical instabilities [16], the color camera is the main diagnostic tool.
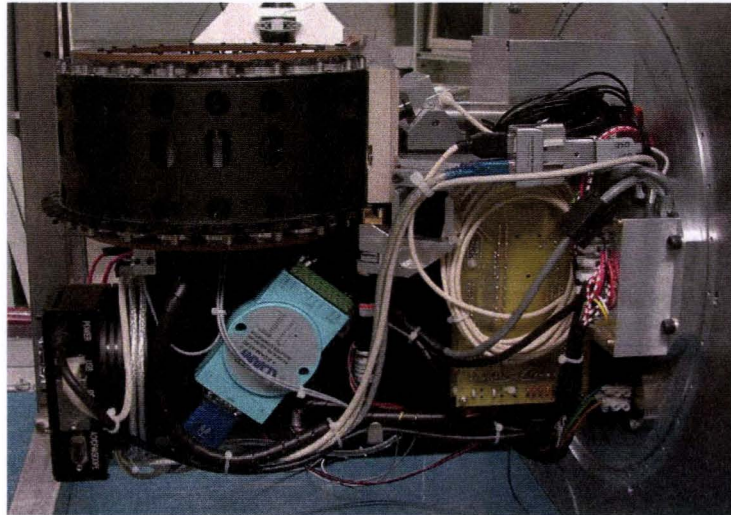
Figure 4.2: *Photograph of the optical setup. The carrousel filled with lamp is clearly visible. In the lower left part of the image the CCD-camera can be seen, while to the right of the carrousel the webcam is visible. The electronics visible in front of the optical frame control the several motors in the setup. Note that this photograph shows the other side of the optical frame with respect to Fig. 4.1.*

Fig. 4.2 shows a photograph of the optical setup. As can be seen, the setup is mounted to a vertical *base plate*. Because the lamp contains a small amount of (toxic) mercury, the part of the setup containing lamps has to be contained by an extra envelope. For this extra containment is taken care by confining the optical setup inside a dome, which will be mounted to the vertical base plate. This is shown in Fig. 4.3.
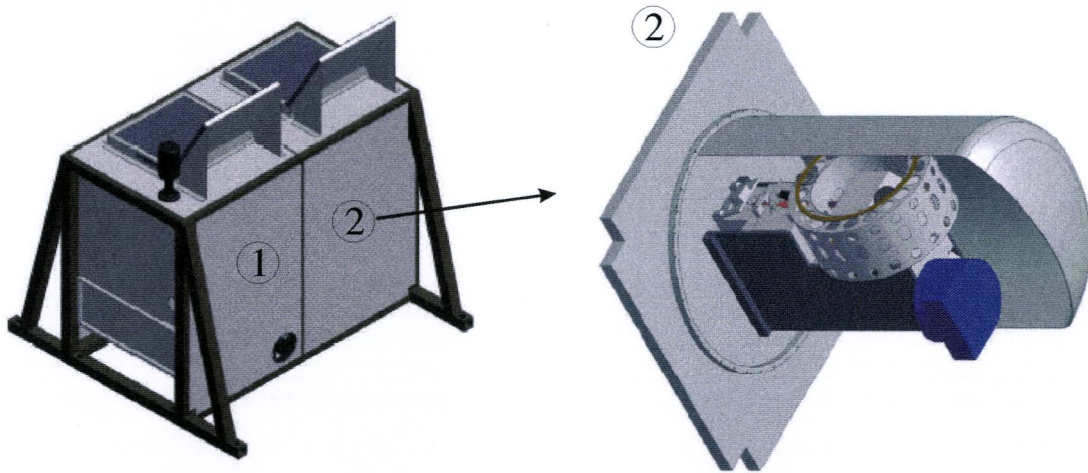
Figure 4.3: *Drawing showing the position of the optical frame in the total measurement setup. In part (1) the power supply and the electronics needed for the laser absorption are positioned. The two laptop computers placed on top control the whole experiment.*

The heat produced by the burning lamp is transported to the base plate by a forced air flow from the lamp to the cool ribs mounted on the base plate. On the other side of the base plate, the heat is removed by a similar forced air flow. In part (1) in Fig. 4.3 the power supply and the electronics needed for the laser absorption system are placed. Furthermore two laptop computers are placed on top of the setup. One laptop computer is used to control the experiment, i.e. move the carrousel, control the lamp, and control the spectrometer. Besides this, the laptop stores the images produced by the color camera system. The second laptop computer acquires the data from the spectrometer and the laser absorption setup and stores the data on its hard disk drive. Furthermore the measurement sequence and laser absorption electronics are governed by this computer. A photograph of the experiment mounted inside the zero-g airplane is shown in Fig. 4.4.
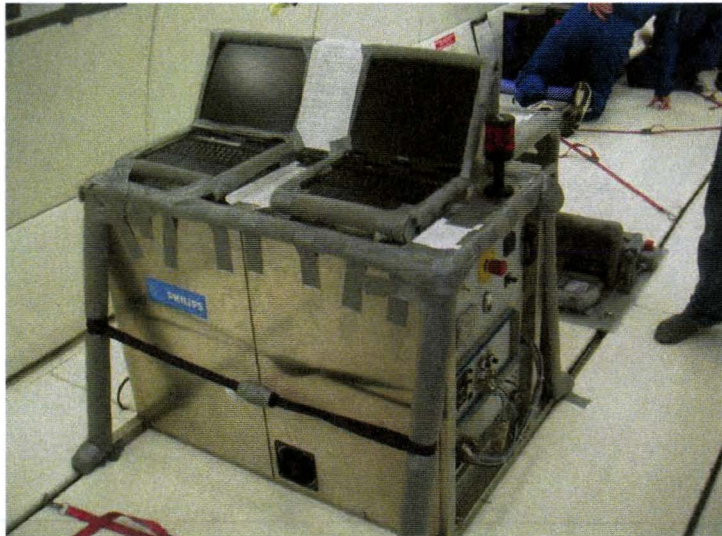
Figure 4.4: *Photograph of the measurement setup placed inside the zero-g airplane. All the sharp edges are covered with plastic foam to prevent someone from getting hurt while free floating.*

4.2 The Spechelle emission spectrometer

The spectrometer used in the ARGES measurement setup is exclusively designed for the measurements on the plasma of metal halide lamps within the ARGES project [3]. Accordingly, the spectrometer had to be small, light weighted, and robust. Robustness is usually not the case with ordinary spectrometers, which make use of the accurate movement of a dispersion grating for wavelength selection. Usually also lenses with large focal lengths are used, causing the spectrometer to be very bulky. The requirement for compactness is solved by using an Echelle grating with a high blaze angle (74°). Because of the high dispersion, due to the high angle of incidence and the high orders used, the focal length of the main lens can be relatively small, and consequently the spectrometer can be very compact. A disadvantage of Echelle-type spectrometers is however that they have a small free spectral range (FSR) at high orders, which results in wavelength overlapping of adjacent orders at a fixed position on the detector. By installing an interference filter [2] in the optical system for selecting a small wavelength interval, the problem of overlapping orders can be avoided. When the possibility to select different interference filters is added to the system (see (8) in Fig. 4.1), these filters can be used for wavelength selection, and the angle of the grating can remain fixed. In this way the requirement for robustness is also fulfilled, because in this case no critically moving parts exist inside the spectrometer. Furthermore the spectrometer has to be able to obtain both spectral and spatial information simultaneously.

A schematic overview of the optical path of the used spectrometer is visualized in Fig. 4.5. Because of the use of an **Echelle** grating in a spectrometer developed for doing measurements in **sp**ace, this spectrometer has been baptized "The Spechelle".

Figure 4.5: *Schematic view of the Spechelle emission spectrometer. The Spechelle is an Echelle type spectrometer in Littrow configuration, meaning that the imaging lens (III) is used for the collimation of both the undispersed beam of light as well as the reflected dispersed beam of light.*
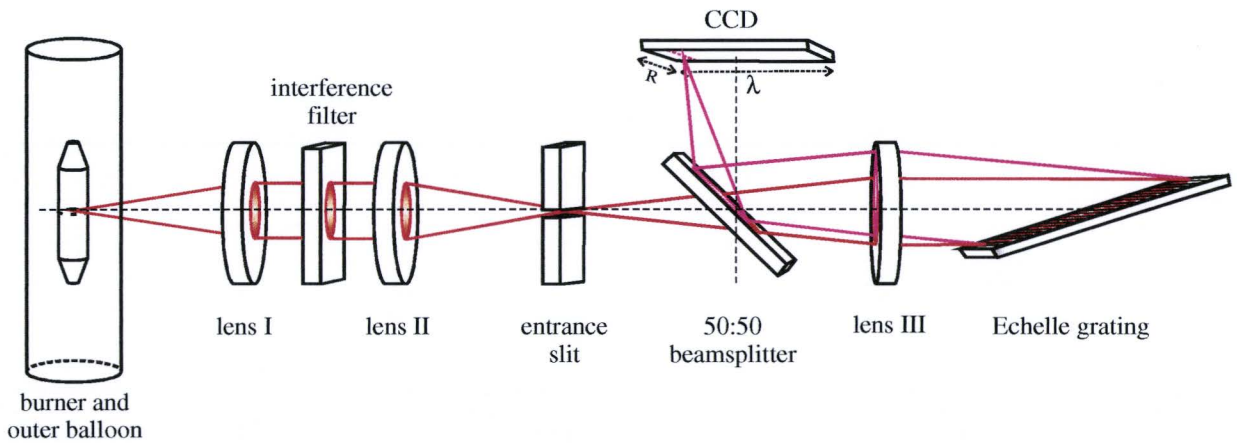
The light originating from the plasma inside the lamp first reaches lens I (100 mm focal distance) and after that forms a parallel beam. A parallel beam is necessary for the proper functioning of the wavelength selection by the interference filter, which is situated between lens I and lens II (also 100 mm focal distance). Lens I & II combined with the interference filter are called the *entrance optics* and form a 1:1 image of the burner on the horizontally placed entrance slit (10 mm x 10 μm). The image consists only of light with the desired small wavelength interval. The entrance slit acts as source for the actual spectrometer, by 'selecting' a narrow horizontal slice from the burner of the vertical lamp. The light originating from the entrance slit passes a 50:50 beam splitter and after being collimated by an achromatic doublet (Lens III), the light reaches the Echelle grating (96 x 46 mm) having 79.01 lines/mm and a 74° blaze angle. Lens III is positioned at its focal distance (150 mm) from the entrance slit to create a parallel beam of light on the Echelle grating. Then the light is back-reflected and dispersed with conservation of the spatial information. The angle of the reflected light with the optical axis of the system is dependent on the wavelength of the light. The reflected light is collimated by the same doublet (Lens III) and focused via the 50:50 beam splitter on the CCD-surface of the camera (SBIG 2000XM). This optical system creates a 1:1 dispersed image of the burner on the CCD-surface (1600x1200 pixels of 7.4x7.4 μm each), with wavelength information due to dispersion of the grating in one direction, and spatial information in the other direction. The CCD is positioned in such a way that the wavelength information is imaged in the '1600-pixel' direction, and the spatial information in the '1200-pixel' direction.

The used CCD-camera has the possibility of binning the pixels before read-out, resulting in a faster readout and smaller data-files. All our measurements are performed with a binning factor 6 in the spatial direction. In this way the number of measurements performed during the ~20 s. micro gravity is increased due to the shortening of the read out time of the camera. The resulting data files are images with 1200x200 pixels. Because a 1:1 image is formed on the CCD-surface, the binning factor 6 results in a reduction of spatial resolution from 7.4 μm (one single pixel) to 6 x 7.4 = 44.4 μm. This

results in approximately 180 data points over the burner diameter (8 mm), which should be sufficient. The spectral resolution is proven to be ~0.024 nm around 640 nm, where the Spechelle is optimized for. This is sufficient for the distinction of the spectral additive lines which are situated around 640 nm (see section 4.3). The detectable spectral range is approximately 7 nm for order 38, corresponding to wavelengths around 640 nm. However, the detectable spectral range becomes smaller when going to higher orders, i.e. smaller wavelengths. For instance, the detectable spectral range for order 60 (around 406 nm) is ~4.4 nm.

The choice of a spectrometer with a grating at a fixed angle and order selection by means of interference filters, combined with a limited size of the CCD-area, has however one disadvantage: some wavelengths are not detectable. In a certain configuration roughly half the wavelengths are not detectable with this spectrometer. By deviating the angle of the Echelle grating somewhat from the ideal angle, which is equal to its blaze angle (74°), the detectable wavelength intervals can be shifted. The selection of emission lines to be measured and the adjustments of the Spechelle necessary for measurement of those lines are discussed in the next paragraph.

4.3   Selection of measurement lines and grating angle

Besides the optically thin emission lines suggested for measurement by Bax [3], we wanted to select some other emission lines to extract more information from the plasma. In section 3.6 it is stated that the measurement of an optically thin mercury emission line is needed for reliable determination of the plasma temperature. The optically thin mercury emission lines at 577 and 579 nm are considered as possible measurement lines. In order to have an extra possibility for determination of the plasma temperature with a different method, also three optically thick mercury emission lines (405, 436 and 546 nm) are selected as possible measurement line. This because the plasma temperature can also be estimated from the absolute intensity of self-reversed emission lines by use of the *Bartels' method* [10]. Because this method is indirect and laborious, this method is not chosen as primary method to determine the plasma temperature.

An extended goal formulated in the ARGES project, besides the determination of atomic additive density profiles, is the determination of ionic additive density profiles. For this purpose several optically thin, well separated and relatively isolated ionic emission lines of dysprosium and cerium are selected. All possible measurement lines and their upper energy level are presented in Table 4.1.

With the use of the grating equation [34]:

$$m\lambda = d(\sin\alpha + \sin\beta) \qquad (4.1)$$

where m denotes the diffraction order, λ the wavelength of the diffracted radiation, d the line spacing of the grating, and α and β respectively the angle of incidence and diffraction with respect to the grating normal, we can calculate the position of light with a certain wavelength on the detector. For that, we take angle of the incidence beam α equal to the angle of the grating normal with the optical axis of the system, and β varying

from α-$\Delta\beta_{max}$ to α+$\Delta\beta_{max}$, with $\Delta\beta_{max}$ the angle of a diffracted beam just reaching the edge of the CCD-area. $\Delta\beta_{max}$ can be calculated with:

$$\Delta\beta_{max} = \tan^{-1}\left(\frac{1600 \cdot 7.4 \cdot 10^{-6}\, m/2}{f_{lensIII}}\right) \tag{4.2}$$

where 1600 is the number of pixels (7.4x7.4 µm) in the wavelength direction, and f_{lens} the focal distance of lens III in meters which equals the length of the optical path between lens III and the CCD-surface. When the CCD-surface is imaginary divided into ten equal areas, we can see what the position of a certain emission line on the detector will be with a certain angle of the grating. This can also be seen in Table 4.1.

Species	λ(nm)	E_{up}(eV)	angle grating + pos. op CCD (1..10)		
			74.0°	74.6°	75.45°
Dy I	642.19	1.93	6-7	4	0-1
Dy I	642.73	2.44	8-9	6	2-3
Dy I	643.67	3.94	10	7-8	4
Dy II	400.05	3.20	8	5-6	2
Dy II	430.86	2.88	x	x	7-8
Ce I	643.44	1.95	9-10	7	3-4
Ce I	643.64	2.39	10	7-8	4
Ce I	644.61	3.66	x	8-9	5-6
Ce II	462.82	3.19	x	x	6-7
Ce II	401.24	3.65	x	8	4-5
Ce II	399.92	3.39	7-8	5-6	1-2
Ce II	401.49	3.62	x	8-9	5
Hg	404.66	7.73	3-4	1-2	x
Hg	435.83	7.73	8	5-6	2
Hg	546.07	7.73	x	x	8
Hg	576.96	8.85	2-3	x	x
Hg	579.07	8.84	5	2-3	x

Table 4.1: An overview of the possible emission lines and their position (1..10) on the CCD of the camera with three different grating angles. A 'x' indicates that the concerned emission line is not detectable. The marked lines are chosen as measurement line with the angle of the grating being 74.6°.

For safety, we wanted to avoid choosing measurement lines positioned very close to the edge of the detector. A small deviation in the optical system could then cause the measurement line to be not detectable. In this way, the final set of measurement lines is chosen. This final set of lines is indicated by the marked cells in Table 4.1. The angle of the grating enabling the measurement of these emission lines is 74.6°.

The interference filters necessary for the measurement of these emission lines are presented in Table 4.2. Because the filter wheel of the ARGES setup has the capacity of five filters, we can only select five filters. The filters needed for the measurement of the

mercury lines are off-the-shelf filters, the other filters are custom made, and therefore more expensive.

filter specifications		Selected lines (nm)		
CWL (nm)	**FWHM (nm)**	**Dy**	**Ce**	**Goal**
640.0	10.0	642.19, 642.73, 643.67	643.44, 643.64, 644.61	Determine radial salt-densities
400.1	5.0	400.05 (ion-line)	401.24, 399.92 (ion-lines)	Determine radial salt-densities
580.0	10.0	579.06 (optically thin Hg-line)		Determine temperature-profile
404.4	2.0	404.66 (self-reversed Hg-line)		Determine temperature-profile
435.8	5.0	435.83 (self-reversed Hg-line)		Determine temperature-profile

Table 4.2: *The chosen interference filters and their objectives. CWL stands for Central Wave Length.*

The large difference in FWHM of the chosen filters is caused by the different free spectral range for different orders. As mentioned before, the free spectral range of the Spechelle decreases with smaller wavelengths. In order to prevent wavelength overlapping, the FWHM's of the filters have to be small enough. Combined with the availability of certain interference filters, the final set of interference filters was chosen.

In this study, the 642.19 nm dysprosium emission line will be used for calculation of the additive density distribution. The according spectroscopic data is presented in Table 4.3.

$\lambda(nm)$	$E_{up}(eV)$	$E_{low}(eV)$	J_{up}	J_{low}	$A\ (s^{-1})$	f	τ_0
642.19	1.93	0.00	8	8	$1.62 \cdot 10^5$	$9.98 \cdot 10^{-4}$	0.5

Table 4.3: *Spectroscopic data of the 642.19 nm Dy emission line.*

The optical thickness τ_0 of this emission line is calculated with Eq. (3.3) using the following assumptions [13]:

- $<n> = 2.0 \cdot 10^{21}\ m^{-3}$
- $R_{eff} = 2$ mm
- $\delta v = 22$ GHz
- $T = 3000$ K

4.4 CCD-Saturation issues

An other problem encountered during the previous PFC in April 2003, is the problem of saturation of the CCD [36]. If the amount of light falling on the surface of the CCD is above a certain level, the individual pixels can reach a saturated state. With our CCD-camera the readout of ~64.000 counts represents a saturated state and in that case the information given by that pixel is useless, because the line intensity of an emission line cannot be determined any more. Because the shutter time was kept

constant to the camera's minimum (0.12 s.) for all measurements performed during the previous PFC, a significant part of the measurements contained saturated pixels. Especially measurements of lamps at higher powers were saturated.

In order to prevent measurements with saturated, and thus useless, pixels, we have to adjust the measurement system in such a way that the light intensity on the CCD can be reduced if necessary. The common way of using a diaphragm for reducing the light intensity is however not desirable for our spectrometer. Installing a diaphragm in the optical path of the Spechelle would cause the number of illuminated grating lines to decrease, and hence the spectral resolution to decrease. This is not desirable, because the maximum spectral resolution is needed to resolve the additive emission lines. The alternative is to use neutral density filters for reducing the light intensity. Because the measurement setup and boundary conditions for the PFC and the space mission are rather different, two different solutions were developed. These solutions are discussed in the following two paragraphs.

4.4.1 Parabolic flights

First we have to realize that the micro-gravity measurement time during the PFC is very short, because each parabola provides only ~20 s. of micro-gravity. Because the lamp is not fully stabilized after those 20 s., we want to do multiple measurements during that short period, to get an idea of the degree of stabilization. Therefore the shutter time may not exceed a few seconds. The minimum value of the shutter time of the used CCD-camera is however 0.12 s.. So varying the shutter time within the given limits only gives us a factor 10-20 for adjusting the light intensity to, in one way, prevent saturation, and in another way, fully use the dynamic range of the detector. There is however a larger difference in light intensity between the chosen measurement lines. Consequently, we have to make use of different types of neutral density filters [2].

The experimental setup used for measurements during the PFC is equipped with two filter wheels. These filters wheels are indicated by the number (8) in Fig. 4.1. Only one filter wheel is used for placing different wavelength filters in the optical path of the Spechelle. The other filter wheel could thus be used for installing neutral density filters in the optical path of the Spechelle. The neutral density filters installed in the second filter wheel are presented in Table 4.4.

Filternr.	Transmission (%)
1	0.01
2	0.10
3	1.00
4	3.16
5	10.00

Table 4.4: *The neutral density filters installed in the second filter wheel of the ARGES setup to prevent saturation of the CCD.*

The experiment control software, developed by the TU/e, was upgraded in such a way that the experimenter is able to directly select a wavelength filter and a neutral

density filter by pressing the accompanying buttons on the keyboard of the laptop computer. Measurements performed before the PFC in normal gravity conditions are used to estimate the suitable combination of shutter time and neutral density filter for every lamp and interference filter. Furthermore, the measurement software is extended with an extra display window, which displays the last measured spectrum of the center of the discharge. By looking at this display during measurements in the airplane, the occurring of saturation of the CCD can be monitored, and the shutter time of the CCD-camera can be adjusted or a different neutral density filter can be selected.

4.4.2 Space mission

Unlike the situation of the very short periods of micro-gravity in the PFC, with measurements performed in the International Space Station (ISS) the micro-gravity time will be very large. The power consumption and the amount of data generated are in this case the limiting factors for the measurement time. But, also unlike the PFC, there is no experimenter present during measurements. A cosmonaut will start up the experiment, but has no time to perform all the measurements. The emission measurements will have to be performed automatically by a built-in computer. Furthermore, the ARGES space setup is due to historical reasons only equipped with one filter wheel. This filter wheel is used to house the five interference filters.

To eliminate the possibility of saturation during measurements in space, the measurement software is equipped with an *autoranging procedure*. This procedure starts a measurement with the minimum shutter time of 0.12 s. Then it doubles the shutter time, until saturation of several pixels occurs. Then, by using the data of the previous measurement, the final shutter time is chosen in such a way that approximately 70% of the dynamic range of the CCD is used. This final measurement is then stored to the internal disk drive. To prevent infinite measurement time if something is wrong, the maximum shutter time is set to 30 s. If we make sure that the CCD has no saturated pixels when the shortest shutter time is used, this procedure is a perfect solution to prevent saturation. The only drawback of this method is the time consuming character of the autorange procedure.

During test measurements on the final space optical system, it appeared that even with the shortest shutter time, most of the measurements were already saturated. Apparently the transmission of the optical system is much higher than the transmission of the prototype used in the PFC. This is probably caused by a better alignment of the optical elements. Nevertheless, without the installation of extra neutral density filters, most of the measurements will be useless. Therefore, tests have been performed [27] with different combinations of neutral density filters available, to avoid saturation under all circumstances. The resulting combination of neutral density filters and interference filters is presented in Table 4.5.

CWL filter (nm)	Transmission grey filter (%)
640.0	-
400.1	-
404.4	50.12
435.8	10.00
580.0	31.62

Table 4.5: *The used interference and neutral density filter combinations in the space setup to prevent saturation of the CCD under all circumstances.*

These neutral density filters are mounted together with the corresponding interference filters in the filters wheel. An extra neutral density filter with a 1.00 % transmission in placed in the vicinity of the entrance slit in the optical path of the Spechelle. The combination of these neutral density filters will prevent the saturation of the CCD under all circumstances [27].

4.5 Measurement plan

In this paragraph the lamps to be measured and the measurement sequence are presented. Again, due to different boundary conditions, the measurement plans for the PFC and the space mission are discussed separately.

4.5.1 Parabolic flights

First we have to determine which type of lamps are interesting to measure in micro-gravity conditions. Of course, for spatially resolved spectroscopic measurements, the lamps under study have to have a quartz burner, because a PCA burner will geometrical average the spatial information, due to the diffuse character of the PCA.

The quartz lamps used in the previous PFC [36] contained dysprosium and cerium as additive, combined with a mercury buffer gas filling of 3 to 10 mg. These lamps showed the expected behavior for transitions to micro- and hyper-gravity. Due to the "cigar" shape of the used burners (see Fig. 4.6), the gradient in wall temperature profile is small, and the liquid salt moved upwards along the burner wall. To eliminate the chance that some of the liquid salt reached the position of the burner that is imaged on the entrance slit of the Spechelle, and thus disturbing the measurement, a new burner design was chosen. This new cylindrically shaped burner design is also shown in Fig. 4.6. The well defined sharp edge of the cylindrical burner will be the coldest spot of the burner, thus creating a well localized position for the liquid salt. As a result of the expected lower temperature of the salt pool with this new burner shape, the amount of additives present in the discharge will also be smaller. Therefore the expected additive radiation will decrease. To make sure that the additive radiation stays well detectable, all the measurement performed in the PFC will be performed at the highest power possible, i.e. 150 W. In that case, the cold spot has the highest temperature possible.
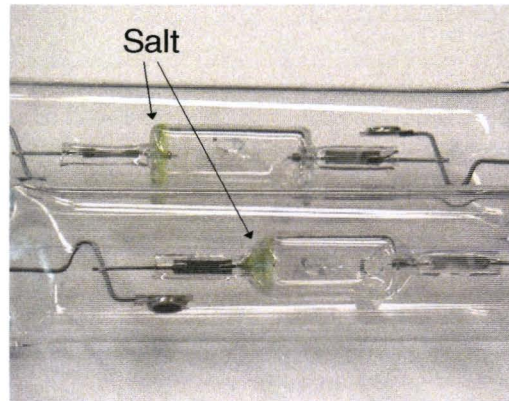
Figure 4.6: *Two types of quartz burners used for the Arges experiments. The upper one will be called "cylinder" and the lower one "cigar" shape. It is clearly visible that both lamps were burned in a vertically position before, because of the position of the (yellow) DyI_3 at the bottom of the burner.*

The chosen lamps for the PFC of October 2003 are presented in Table 4.6. To overcome the possible failure of one lamp, every lamp is put twice in the measurement carrousel. Because for plasma temperature determination the absolute intensity of the 579 nm mercury emission line has to be known, the Spechelle has to be calibrated with a lamp with a known spectral radiance. In general a tungsten ribbon lamp is used to calibrate spectrometers, but this lamp cannot be placed in the measurement position of the Spechelle due to its dimension. A lamp with a pure mercury vapor discharge is therefore placed in the measurement setup, and is used as reference lamp. Because the light output of a lamp without additives is very stable, this type of lamp can be used as reference lamp. The reference lamp was calibrated with a tungsten ribbon lamp with a Jobin-Yvon HR 640 spectrometer at Philips CDL.

Carrousel position	Lamp number	Hg dose (mg)	Salt	Burner shape
11	23	10.0	CeI_3	cylinder
12	45	10.0	CeI_3	"cigar"
13	50	10.0	--	cylinder
14	29	10.0	DyI_3	cylinder
15	38	5.0	DyI_3	cylinder
16	26	10.0	CeI_3	cylinder
17	48	10.0	CeI_3	"cigar"
18	52	10.0	--	cylinder
19	30	10.0	DyI_3	cylinder
20	41	5.0	DyI_3	cylinder

Table 4.6: *Overview of the selected lamps for the parabolic flight campaign. The carrousel positions 1-10 are occupied by PCA lamps for the study of helical instabilities [16].*

During a parabolic flight, each of the five breaks offered will be used to start a next lamp. In this way, the lamp has the time to warm up before the first of five parabolas. Between two parabolas, the next interference filter and the needed neutral density filter are selected. The shutter time of the CCD-camera is also adjusted if necessary.

The acquiring of useful and unsaturated measurements of atomic additive and mercury emission lines was emphasized in the PFC. The measurement of the ionic emission lines was given a lower priority and not performed due to time limitations during the PFC.

4.5.2 Space mission

After measurement of the selected lamps in the PFC, there was no reason for replacing one of the lamps for the space mission. The lamps selected for the space mission are thus identical to the ones presented in Table 4.6. The positions of the quartz lamps in the carrousel of the space experiment are however position 1-10 in stead of 11-20.

Because the micro-gravity measurement time in space is much larger, it is possible to do measurements with all the selected interference filters, including the "ion"-filters. Moreover, all the lamps will be measured at different power levels.

5 Design of the Parabolamp experiment

In this Chapter the objectives for an extra experiment to measure the influence of gravity on the visible light output of metal halide lamps are presented. The design process of this additional Parabolamp experiment is shown, as well as the measurement plan for the PFC.

5.1 Motivation

It is believed that the convection flows present in a burning metal halide lamp under normal gravity conditions have great influence on the amount of additives in the discharge, and thus on the lamp efficiency. This has been discussed in section 2.5. The quantitative effect of this convection flows on the overall efficiency of the lamp is however difficult to assess, since in the presence of gravity the convection velocities can only be influenced by indirect means (e.g. the buffer gas pressure) which also influence the energy balance of the lamp in other ways.

To be able to vary the convection velocity by varying gravity without having to change anything else in the lamp, poses a unique possibility to assess the effect that convection mixing has on the efficiency of the discharge. In order to separate the slowly changing effects of gravity (e.g. the cold spot temperature and thus additive pressures) and faster changing effects (atomic additive partial pressures in the discharge) measurements have been performed during gravity transitions.

In a sense these measurements are complementary to the ARGES experiments in which the details of transport phenomena are investigated. With the Parabolamp experiment the quantitative consequences of radial and axial segregation on the visible light output of several types of metal halide lamps have been evaluated.

5.2 Design requirements

For the design of a measurement setup capable of performing the desired measurements, the following scientific requirements were defined:

- Continuous measurement of the integral visible light output of a lamp as a function of time.
- The measurement data should be stored on disk.
- The possibility to measure both vertically as well as horizontally burning metal halide lamps.
- The possibility to change lamps during flight, to be able to measure several type of lamps during the PFC.

Moreover, when designing an experiment for performing measurements in a parabolic flight, the following 'parabolic flight' safety requirements have to be complied with:

- An emergency electric shutdown mechanism has to be present.
- All the touchable parts of the experiment are not allowed to have a temperature above 40°C.
- The experimental setup has to be robust and with a center of mass point as low as possible, with a maximum of 90cm above the airplane floor.
- The experiment is not allowed to have sharp edges, for obvious reasons.

With these requirements in mind, we try to develop a suitable measurement setup.

5.3 Ullbricht sphere

The common used method to measure the integral visible light output of a lamp is to make use of an Ullbricht sphere. An Ullbricht sphere is a hollow sphere with the inner surface coated with a material which is highly diffusive-reflective. From the theory of the radiation exchange within an enclosure of diffuse surfaces, it can be proven that the flux of diffuse reflected radiation received by a surface element of the inner wall of a sphere is equal to its fraction of the total inner surface of the sphere [30]. In other words: every surface element on the inner surface of the sphere is illuminated by the same amount of radiation originating from the reflections on the inner surface. The sphere spatially integrates the light if the inner wall is illuminated by a light source placed inside the sphere. If a small photo detector is placed on the inner surface of the sphere, and direct light from the lamp is prevented from entering the detector by means of a small screen, the measured light intensity by the detector is equal to the relative integral light output of the lamp inside the sphere. Therefore, after proper calibration, an Ullbricht sphere is thus a suitable for measuring the integral light output of a lamp. Because we are only interested in the relative variations of the integral light output with respect to the 1g situation, we did not calibrate the sphere.
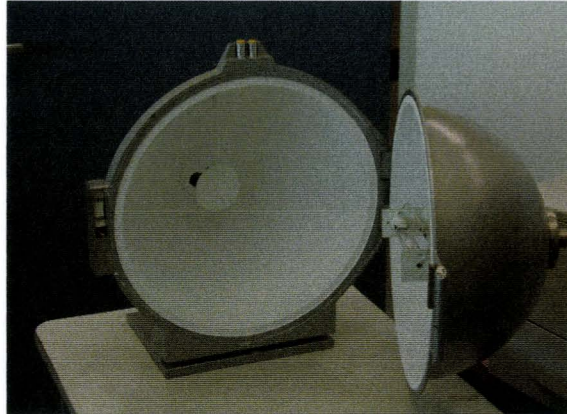
Figure 5.1*: An Ullbricht sphere with a high reflective diffuse coating on the inner surface for geometrical averaging of the light. The photo detector is positioned at the back of the sphere with a disk in front of it, to prevent direct light from the lamp illuminating the detector.*

A photograph of the used Ullbricht sphere with a lamp inside it is shown in Fig. 5.1. Due to the limited space available in the zero-g airplane, only a relatively small sphere can be used. The Ullbricht sphere for the Parabolamp experiment is used in combination with a PIN-10AP detector/filter combination from United Detector Technology. The spectral response of this detector/filter combination matches the spectral response of the human eye with an inaccuracy of less than 2%, compared to the area under the human spectral sensitivity graph. In this way, the output voltage of the detector equals the relative integral visible luminous output of the lamp placed inside the sphere.

5.4 Electronics & software

In order to satisfy the first two scientific requirements, concerning continuous measurement and storage of the integral visible light output of a lamp, a measurement system has to be developed to continuously read the output voltage of the photo detector in the Ullbricht sphere and to store these values. It is decided to make use of the TUeDACS measurement system [24], which is frequently used at the TU/e. Standard components like Analogue Digital Converters (ADCs) and computer interfaces are directly available with *The Physical & Technical Laboratory Automation Group (BLN)* [22], which produces these components and is situated at the TU/e. The ideal input signal for the standard type of ADC has to be in the range of −10 V to +10 V. Because the typical output voltage of the used photo detector in our application is in the microvolt range, an amplifier was built to amplify the detector signal. BLN has developed and produced this amplifier, with an electric scheme as visualized in Fig. 5.2.
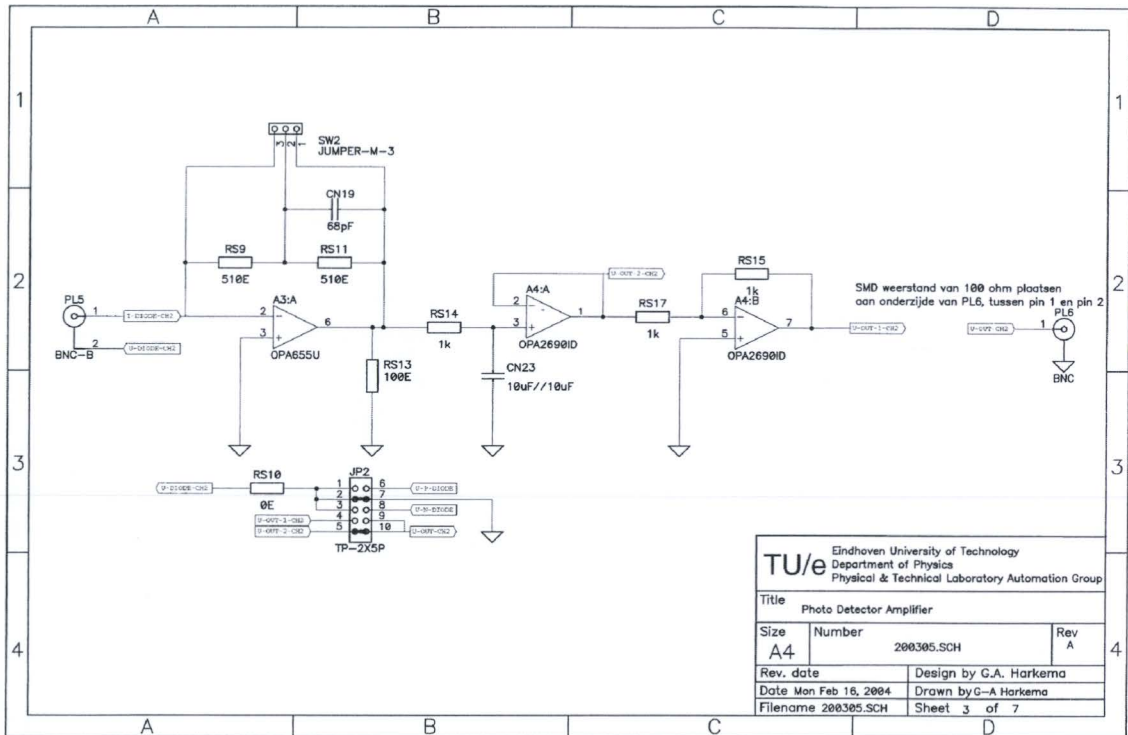
Figure 5.2: *Electric scheme of the designed amplifier for the photo detector. The operational amplifier circuit drawn most to the left boosts up the voltage from the photo detector. Together with a 20 μF capacitor and a 1 kΩ resistance the second operational amplifier acts as a low band pass filter (50 Hz) to infer the average light output. The third operational amplifier is not used.*

A 16-bit ADC (TUeDACS/1 Analog Input Unit [24]), combined with an PCMCIA Serial Highway controller [24] offer the measurement signal to a computer. The computer is equipped with a software program, developed by the BLN, which acquires the measurement signal and stores the measured values to the internal hard disk drive. The sampling frequency is set to 10 Hz, and every minute a new txt-file is created, in which the measured values are written. The software also displays the measurement values of the last 10 seconds graphically on the computer screen to evaluate the burning of the lamp by the experimenter, and to see the effects of the gravity transitions on the light output during flight. A screenshot of the measurement software is shown in Fig. 5.3.
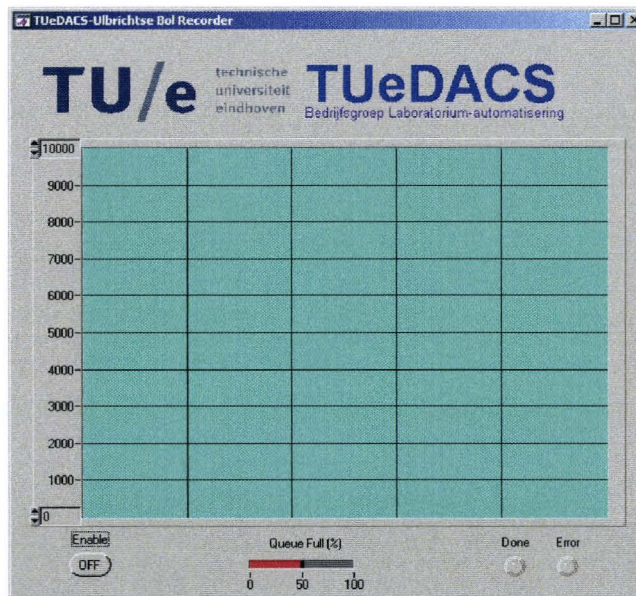
Figure 5.3: *Screenshot of the developed software for measuring of the integral visible light output of the lamp inside the Ullbricht sphere. (no signal is visible in the picture)*

5.5   Mechanical construction

The experimental setup preferably has to consist of one piece, with a center of mass as low as possible. The most easy way of fulfilling these requirements is by using a strong base plate, and mounting all the necessary components of the measurement setup on this plate. Therefore, a 10 mm thick aluminum plate (700 x 1100 mm) is chosen as base plate. Aluminum is chosen to reduce weight and to withstand oxidation by comparison with an iron base plate.

Preliminary test measurements showed that the outer wall temperature of the Ullbricht sphere would exceed 40°C, if the lamps to be measured were burned inside. That is why the Ullbricht sphere had to be enclosed by a "cage", to prevent the sphere from being touched by the experimenter during flight. To prevent the sphere from reaching even higher temperatures, what would harm the inner high reflective coating, this protection cage is made of perforated metal plates, to allow a convective airflow to cool the outer wall of the sphere. The frame of the cage is built of standard Bosch profiles, giving the cage enough strength to withstand a falling person. Photographs of different stages of the construction process are shown in Fig.5.4. The experiment is constructed by the Philips CDL workshop (WOCOL).

To fulfill the requirement to be able to measure both vertically as well as horizontally burning lamps, without having to touch the hot lamp or sphere, a lamp holder with a rotating principle was designed cooperation with the WOCOL. The rotating arm was made long enough to protrude the protection cage. This construction is best seen in Fig. 5.4b and 5.4c.
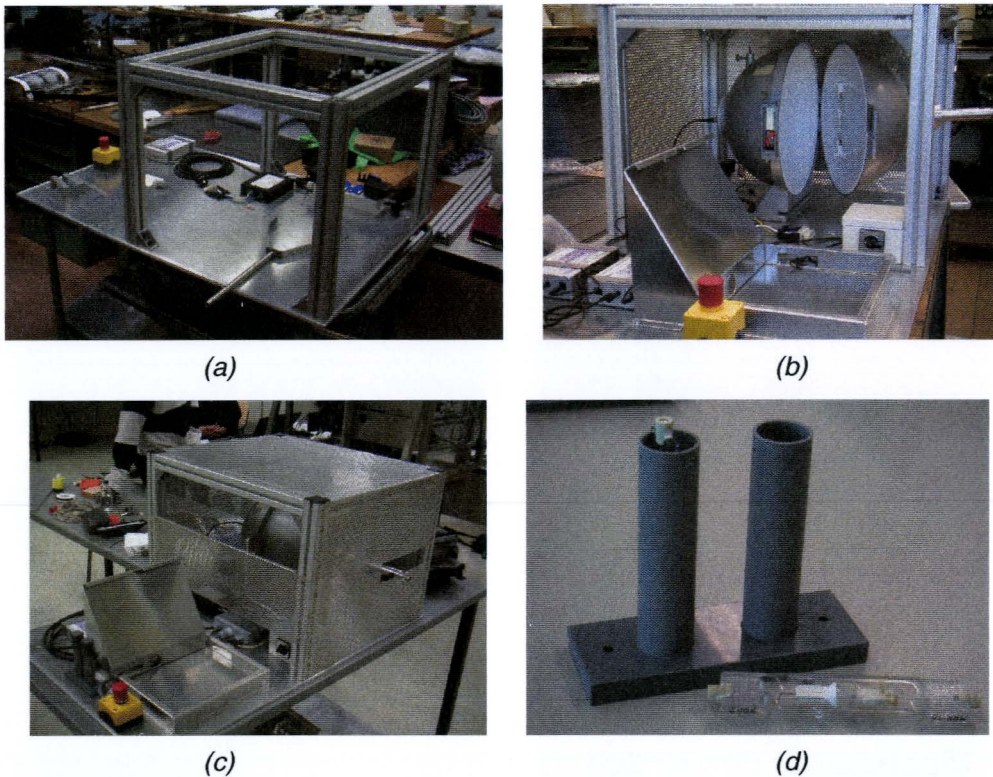
(a)   *(b)*

(c)   *(d)*

Figure 5.4: *Photographs of the construction of the Parabolamp experiment. The "cage" around the sphere is necessary because surfaces with temperatures above 40 °C have to be protected against accidental touching. A PVC lamp container (d) is constructed for safe storage of the second lamp during flight. The final version of the lamp container has a PVC screw top.*

Because it is desired to measure more than one lamp on each flight day of the PFC, the possibility to change a lamp during flight had to be created. For that, a PVC lamp container was constructed (see Fig. 5.4d). This container was mounted to the base plate and is supplied with PVC screw tops, for safe storage and easy changing of the lamp. Because the PVC is softer than the quartz of the outer balloon of the lamps, the possibility of lamp breakage is minimal. With a second lamp placed in the container, this lamp can be exchanged with the lamp inside the sphere during flight.

Furthermore an emergency button was added to the electrical circuit, to electrical shut down the experiment in case of an emergency. Also for safety, a microswitch was installed in the closing mechanism of the sphere, which interrupts the power to the lamp if the sphere is opened. In this way, the lamp always extinguishes when the sphere is opened, and there is no possibility that the experimenter gets an electric shock. Of course all the metal components present in the setup are well grounded.

5.6   Measurement plan

Because no spectroscopic measurements were to be performed on the lamps selected for the Parabolamp experiment, the requirement of a fully transparent burner material could be dropped. Modern metal halide lamps, which are not used in optical applications (beamers etc.), make use of a ceramic (PCA) burner. This PCA can withstand higher temperatures than quartz, and usually these type of lamps are designed in such a way that the cold spot temperature is higher. Because we wanted to perform experiments on lamps which are very close to commercial lamps (CDM) or which are considered to be promising for the future (Helios) the following lamp choice was made.

To be able to quantify the effects of lamp efficiency change as a function of gravity, as qualitatively described in section 2.5, for two extremes in lamp design, we selected two types of burners. The first burner is a *CDM-type burner,* which is characterized by an aspect ratio of 1. The aspect ratio is the ratio of the discharge length (=electrode distance) and the burner diameter. Combined with a relatively high buffer gas pressure (~10 Bar), the convection flows present in this burner type are expected to be strong, resulting in little axial segregation. It is expected that this type of lamp is positioned at the top or on the right hand side of the Fischer curve (section 2.3).

The second type of burner selected is a *Helios* type of burner. The aspect ratio of this burner is 4. This lamp is expected to suffer severe from axial segregation. Based on the mercury pressure and internal diameter, its position on the Fischer curve is expected to be just at the left of the maximum of the Fischer curve. The electrode distances of the CDM and Helios type burners are ~6 and ~16 mm respectively. A photograph of both burner types is shown in Fig. 5.5.
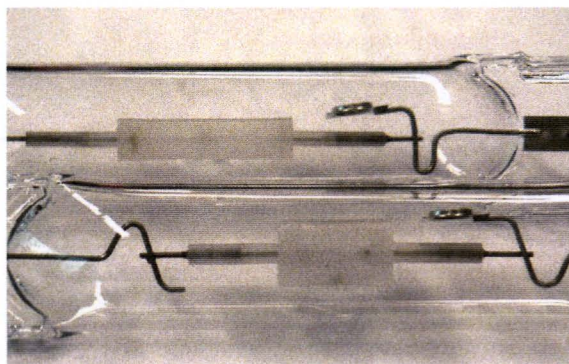
Figure 5.5: *Two different types of PCA burners used in the Parabolamp experiment. The upper one is called "Helios", and the lower one is a CDM-type of burner.*

For consistency, we want to measure the integral visible light output change during several parabolas per orientation per lamp. With the warm up and cool down time of several minutes in mind, we can determine that we are able to measure 2 lamps per flight, both vertically and horizontally. Therefore we selected 6 lamps for measurement during the PFC. The selected lamps and their additives are presented in Table 5.1. The

chosen salt combinations are promising additives for the according type of burner, and therefore interesting to investigate.

nr.	Burnertype	Salt	Hg dose (mg)
43	CDM 70W/R	NaTlDy	9.00
46	CDM 70W/R	NaDy	9.00
50	CDM 70W/R	NaTlCa	9.00
52	CDM 70W/R	NaTlCa/Ce	9.00
H1	Helios	NaCe	3.46
H2	Helios	NaCe	3.46

Table 5.1: *Overview of the used lamps for the Parabolamp experiment in the parabolic flight campaign. The start gas used in the CDM and Helios type of burners is 240 and 300 mBar ArKr respectively.*

The electronic lamp driver, mounted on the base plate, keeps the power of the lamp constant to 75 W during flight. In this way, the measured change in relative integral visible light output of the lamp represents the change in efficiency.

A photograph of the Parabolamp experiment mounted in the zero-g airplane is shown in Figure 5.6.

Figure 5.4: *The Parabolamp experiment mounted in the zero-g airplane. To the left of the Parabolamp experiment, the ARGES measurement setup is visible.*

6   Results and discussion

6.1   ARGES

In this section the results of the measurements performed with the ARGES setup are presented and discussed. Because the main objective of this study was the development of a solid procedure for analyzing of the spectroscopic measurements, the analysis of one lamp is presented step by step. The performed measurement sequence of the PFC in October 2003 can be found in Appendix B for both the ARGES measurements as well as the Parabolamp experiment. The used shutter times and neutral density filters are also presented in Appendix B. Because we concentrated on the acquisition of good measurements of atomic additive and mercury emission lines, there was no flight time left to also measure ionic emission lines. The measurement of these ionic lines has to be performed during the ISS space mission in April 2004.

In the next paragraphs the following data analysis steps are discussed:

- The acquisition and interpretation of a Spechelle measurement.
- The subtraction of a dark background measurement.
- The straightening of the emission lines.
- The emission line fit procedure.
- The correction for slit imperfections.
- The calibration of the mercury emission lines.
- The Abel inversion of the measured lateral line intensities.
- Calculation of the plasma temperature profile.
- Calculation of the radial additive densities with the calculated temperature profile and the Abel inverted lateral additive emission line intensity.

Furthermore an estimation of the possible errors of this data analysis procedure is presented in section 6.1.5.

6.1.1 A Spechelle measurement

A typical Spechelle measurement with the 640 nm interference filter is shown in Fig. 6.1. In one direction the spectral information is given, while the other direction the spatial information is given. Because the spatial binning factor was set to 6 for all our measurements, this image consists of 1600 (λ) by 200 pixels (x). The picture shown in Fig. 6.1 is stretched 6 times in the spatial direction, to obtain the original dimensions of the CCD.

The significant curvature of the emission lines is caused by the relatively large entrance slit length. The "off-axis" light, originating from the edge of the slit, reaches the Echelle grating under an angle. This causes the spectral line to be imaged on a different position of the CCD than radiation with the same wavelength originated from the center of the slit, and thus creating a curvature. Especially with the use of gratings with a high angle of incidence, this curvature is significant. The resulting emission lines have a parabolic shape [36], and we will correct for this curvature.

x

λ
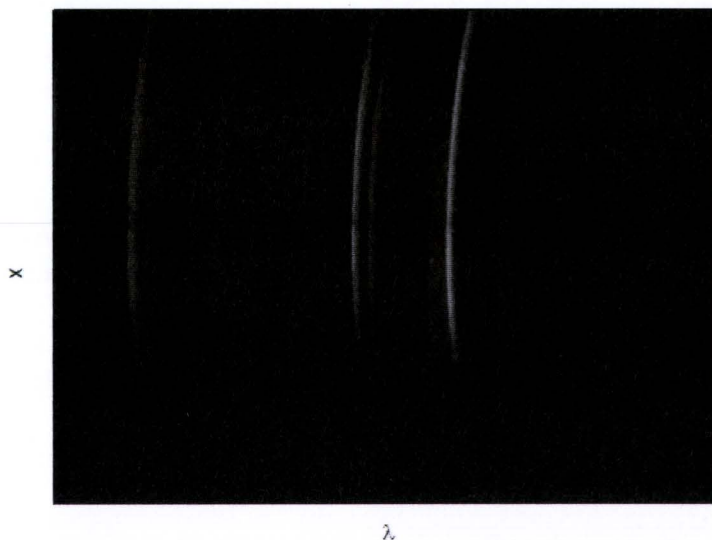
Figure 6.1: *A Spechelle CCD-image of a burning Dy lamp with the 640 nm interference filter. Horizontally and vertically we obtain respectively spectral information (λ) and spatial information (x). The middle of the burner corresponds to a line somewhat above the actual middle of the CCD.*

If the measured light intensity at a certain pixel row (=lateral position) is plotted as a function of the wavelength, a typical spectrum as showed in Fig. 6.2 is the result. The 642.19 and 642.73 nm emission lines are assigned.

Figure 6.2: Measured spectrum of a Dy lamp at a certain lateral position during micro gravity phase.

6.1.2 Construction of lateral profiles

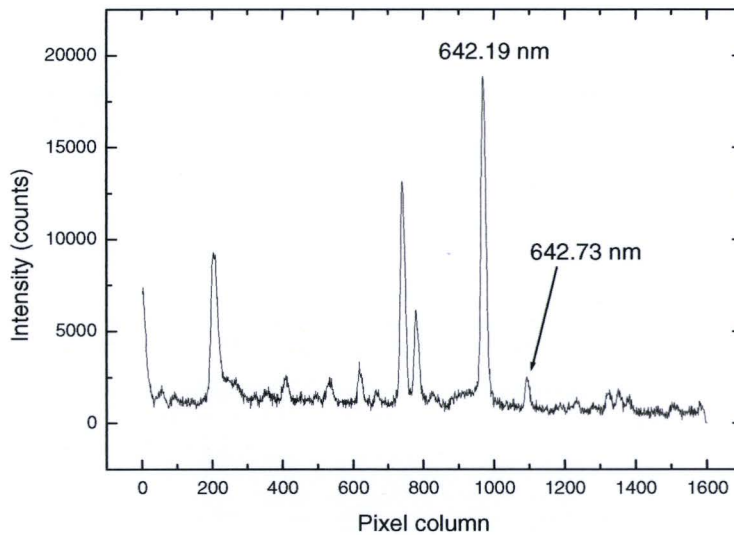The analysis of the measurement data starts with the pixel by pixel subtraction of the dark background measurement. The automatic measurement sequence used during the PFC, performs a dark measurement every 9 illuminated measurements. When a dark measurement is performed, the shutter of the CCD-camera is kept closed, but the CCD is read out after the same time as the shutter time of the illuminated measurements. The readout of the dark measurement has to be subtracted from the readout of an illuminated measurement. To speed up this operation, a software program "Background Subtracter" (Appendix A.I) is written. This program automatically subtracts a selected dark background measurement from the selected measurement file(s). Multiple measurement files can be selected, to accelerate this data processing step. The graphical representation of a typical background measurement is shown in Fig. 6.3.

The second step in the data processing procedure is the straightening of the emission lines. Because we are going to use an automatic fitting routine to determine the measured lateral line intensities, the emission line preferably has to be in a constant pixel column interval for every lateral position. Due to the considerable curvature of the emission lines, this is not the case. Therefore, the curvature of the 642.19 nm emission line is determined and fitted with a polynomial fit. The values of this fit are used by the developed software program "Emission line straightener" (Appendix A.II), which automatically straightens the emission lines of the selected measurement file(s). This program shifts the pixel rows in such a way, that the emission line curvature will be compensated. The straightening is however not completely perfect for all emission lines in a measurement, because the emission line curvature slightly differs for different wavelengths. Again, to speed up this operation, multiple measurements files can be selected. The result of this emission line straightening for an arbitrary measurement is shown in Fig. 6.4.
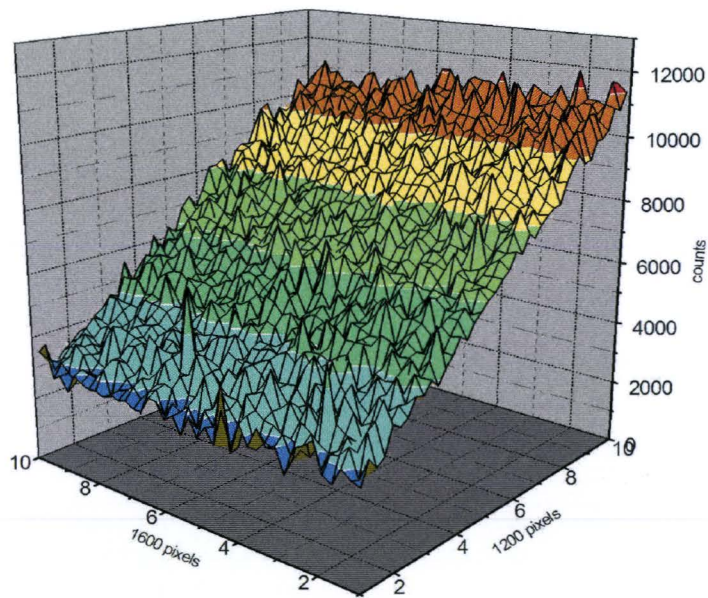
Figure 6.3: *Illustration of a typical background measurement. Note that the slope in the 1200-pixel-direction is visible in every background measurement.*
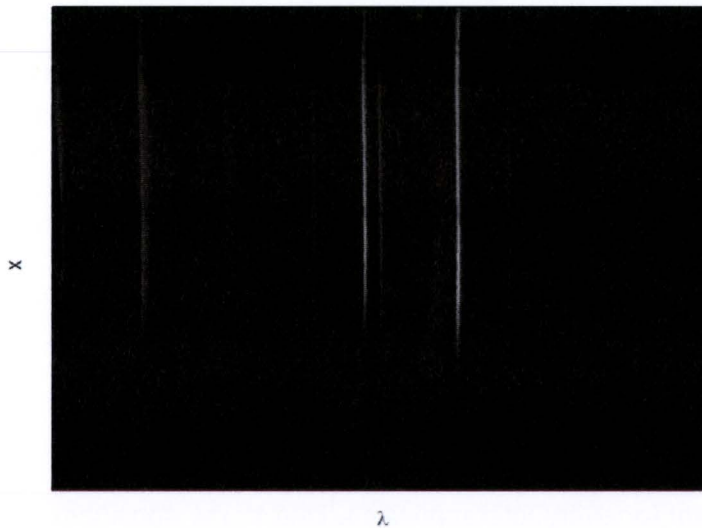
Figure 6.4: *A Spechelle CCD-image after being straightened by the special developed image straighten software (Appendix A.II). The curvature visible on the left hand side of the image is caused by the extra insertion of zeros, needed to shift the pixel rows.*

Now the emission lines are positioned in the same pixel column interval over the burner diameter, the emission line intensity can be determined with an automatic fitting routine, which automatically determines the area under the emission line. Because the line profile of the emission lines is a Lorentz shaped profile, and the software package Microcal Origin [39] is equipped with an Lorentz-fitting routine and the possibility to

automate fitting processes, Microcal Origin is chosen as a software tool to determine the emission line intensities. The Lorentz-fitting routine is part of the *non-linear least square fitter* of Origin. This fitter uses Levenberg-Marquardt iterations to find the best fit to the measured data points. The success of these iterations is strongly dependent of the used initial fit values, and the amount of noise in the data points.

Origin features the possibility to automate every operation with the use of the built in programming language LabTalk [33]. The developed fitting routine "fit642.ogs" (Appendix A.IV) is written in the LabTalk programming language, to determine the emission line intensities as a function of the lateral position. Next, the working of this fitting routine is described.

First, the fitting routine creates a new worksheet to store all the resulting fitting parameters in. Then, for each pixel row (=lateral position) in a given pixel row interval, a Lorentz fit is performed on the data points between pixel column 950 and pixel column 1050 (=wavelength interval). The 642.19 nm dysprosium emission line is after to the emission line straightening always situated in this range. Outside this range other emission lines appear in the spectrum, which would disturb the fitting process if they were present in the pixel column range used for fitting. An example of a performed Lorentz fit with the calculated fit parameters is shown in Fig. 6.5.
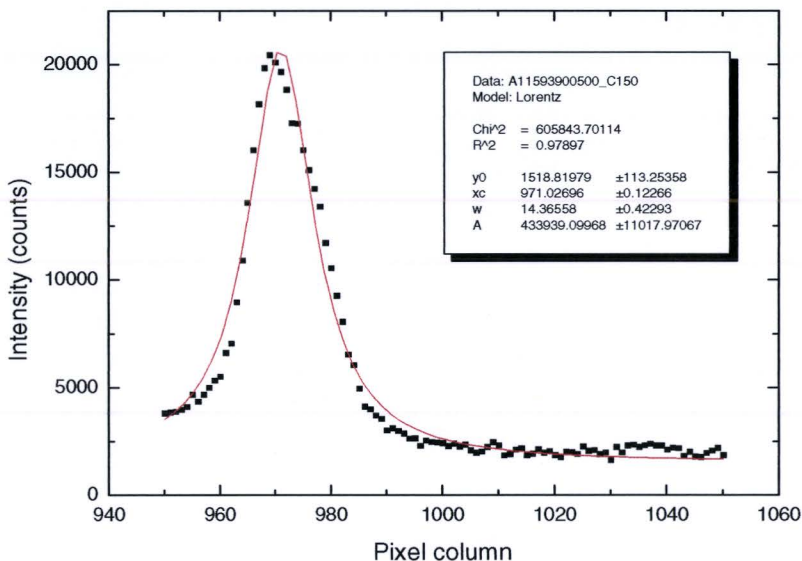
Figure 6.5: *A Lorentz fit is used to determine the line intensity of the 642.19 nm Dy line. The fit parameters are presented in the graph.*

If a standard Lorentz fitting session is started and closed for every pixel row, this standard fitting session automatically determines the initial values for the fitting session. If the emission line is strong enough, this standard fitting session will find the correct fitting parameters for this emission line. However, if the emission line is not so strong, the fitting session may result in fitting parameters which are not useful, like Lorentz profiles with almost infinite widths and wrong center wavelengths. To avoid this problem, the Lorentz fitting session has to be controlled carefully, and the following procedure has

to be used. If a pixel row interval is given, the fitting routine fit642.ogs starts the fitting of the emission line in the center of this pixel row interval. Usually the center of the lamp corresponds more or less with this pixel row, and therefore at least the expected line intensity is large. The Lorentz fit procedure generally has no problem in finding the right fit parameters for this emission line when the initial fit parameters (p1 t/m p4 in Appendix A.IV) are given roughly. Subsequently, the resulting fit parameters of the first Lorentz fit, are used as initial fit values for the fit of the data in the next pixel row. Because the emission line shape of the next pixel row is only slightly different, the right fit values can be found very fast by the Levenberg-Marquardt iterations. These values are now used as initial fit values for the next pixel row. This is repeated until the pixel row at the end of the given interval is reached. Then, the fitting routine calculates the fitting parameters for the other half of the pixel row interval in the same way. The big advantage of the determination of the fitting values in this way, is that the very weak line intensities near the edge of the burner are also automatically fitted in the right way.

At the end of the fit642.ogs fitting routine, the calculated areas under the fitted Lorentz profiles (fit parameter A in Fig. 6.5) are presented graphically as a function of the pixel row. An example of three normalized automatically generated mercury emission line intensity profiles (with fit579.ogs) is shown in Fig. 6.6.

6.1.3 Slit imperfections

Now we have a method for determination of the lateral line intensities of the 642.19 nm dysprosium emission line. With only a small change in the source code of the fit642.ogs fitting routine, the fit579.ogs fitting routine (Appendix A.III) was developed, to determine the lateral 579.07 nm mercury emission line intensity profile. With this profile the temperature profile can be calculated, following the procedure presented in section 3.6. The operations performed within the fit579.ogs routine are identical to the operations performed by fit642.ogs, except the use of different initial fit values for the first Lorentz fit, and an other pixel column interval (=wavelength interval) in which the 579.07 nm mercury emission line is situated. The used pixel column interval for the 579.07 nm mercury emission line was 200-800. Before the determination of the lateral line intensities is started, a dark background measurement is subtracted with the use of the program Background Subtracter, and the emission lines are straightened with the program Emission line straightener. The curvature of the mercury emission line is due to a different wavelength and thus a different angular dispersion, not identical to the curvature of the of the 642 nm emission line. But due to the relative isolated position of the mercury emission line, and the relatively large FWHM, the fitting routine has no problem in fitting the emission line, even if it shifts a little with respect to the previous pixel row. This is why no special straightening procedure has been created for the mercury emission line.

When three different lamps are analyzed with the use of fit579.ogs, and their line intensity profiles are normalized, we see something remarkable, like is shown in Fig. 6.6. In all three examined lamps, there are several dips clearly visible. Furthermore we see that the centers of the discharges, located at the lateral position with the highest line intensity, are not located at the same position. This is due to a little deviation in the horizontal position of the burner in the outer balloon. But we do see, in spite of a different position of the discharge on the detector, that the dips occur at exactly the same pixel

rows, and thus at exactly the same lateral position. This effect is very likely caused by imperfections of the entrance slit in the Spechelle. Probably some regions of the entrance slit are narrower, and therefore less light is transmitted at these regions of the entrance slit.
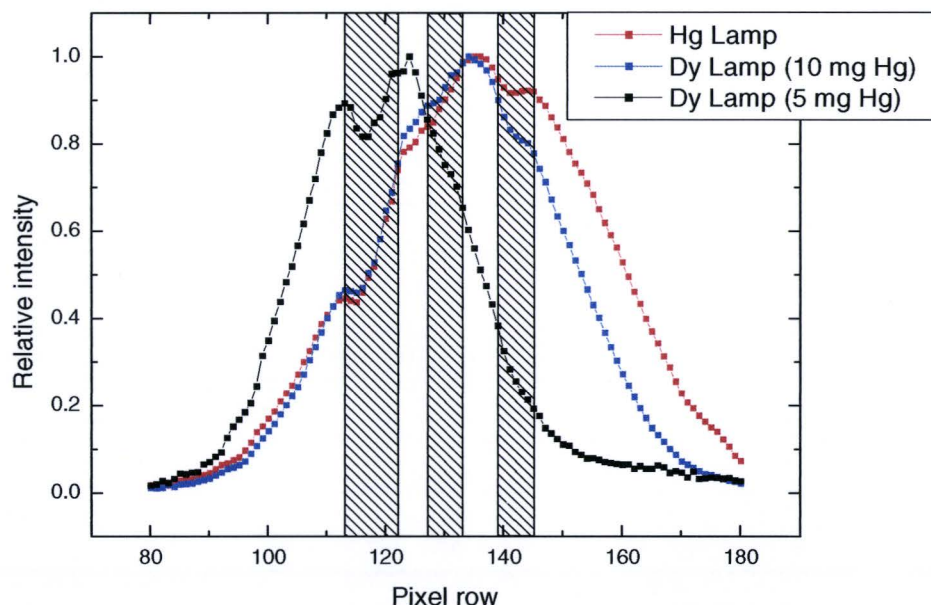

Figure 6.6: *Normalized measurements of different lamps show identical "dips" in the line intensity of the 579.07 nm Hg line. The dips are indicated by the cross-hatched areas. Slit imperfections are likely the cause of the reduced light intensity at certain lateral positions.*

In order to correct for these slit imperfections, we have to exactly distinguish the pixel row intervals with lower intensities. For that, the mercury lamp with no additives is used, because the discharge channel of a pure mercury discharge is more wide than the discharge channel of a metal halide lamp. With a more wide discharge, the real line intensity distribution can be determined in a better way. To be able to construct the original line intensity distribution, the measured lateral line intensities of the mercury discharge are plotted graphically. This is shown by the black dots in Fig. 6.7. Subsequently, the data point situated in the clearly distinguishable dips are deleted, and the remaining data points are used for fitting. The data point intervals excluded from the fitting process are also presented in Fig. 6.7.

It appeared, after the trying of several fit functions, that the line intensity distribution can be perfectly described by a Gaussian shaped profile. A Gaussian fit to the non-excluded data points is shown by the black line in Fig. 6.7. Next, the data points of the Gaussian profile are calculated for the pixel rows which were excluded from the fitting process. These points are indicated by the red dots in Fig. 6.7. The ratio of the calculated (actual) line intensity and the measured line intensity is set as correction factor for further analysis of the measurements. The correction factors calculated in this way are presented in Table 6.1, and are used in the analysis of all other measurements, to correct for the appeared slit imperfections.
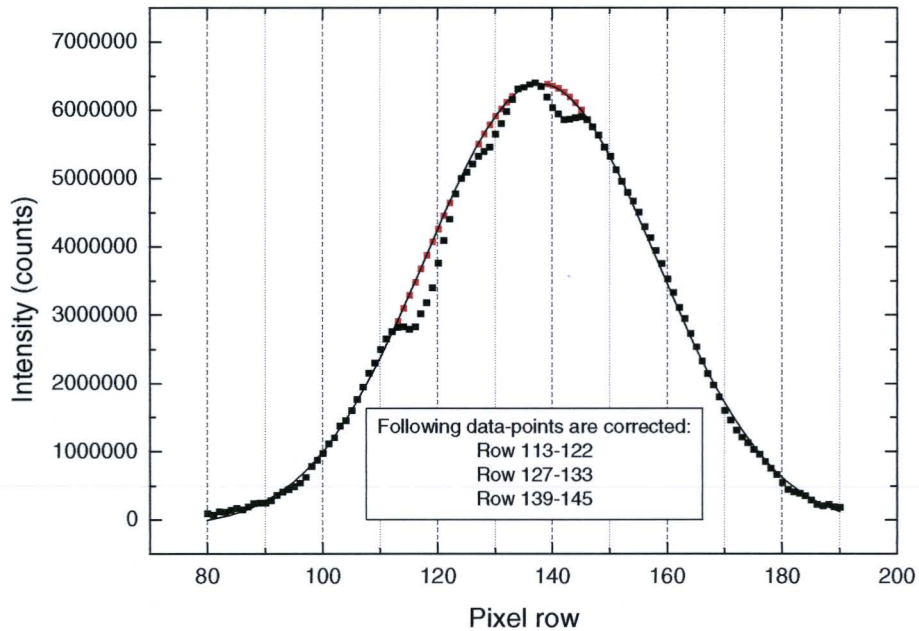
Figure 6.7: *With a pure Hg lamp the correction factors can be calculated for the region of reduced light intensity. The black dots denotes the measured line intensities, the red ones the corrected data points. Three regions are defined as presented in the graph.*

Pixel row	Cor. factor	Pixel row	Cor. factor
113	1.029	129	1.060
114	1.094	130	1.046
115	1.177	131	1.037
116	1.230	132	1.022
117	1.218	133	1.008
118	1.217	139	1.031
119	1.195	140	1.054
120	1.134	141	1.063
121	1.088	142	1.068
122	1.054	143	1.055
127	1.034	144	1.036
128	1.047	145	1.017

Table 6.1: *The calculated correction factors for each pixel row. Note that the list of pixel row numbers is not continuous.*

6.1.4 Temperature profiles

The next step in the measurement analysis procedure is the calculation of the plasma temperature $T(r)$ as a function of the radius. For that, we follow the procedure presented in section 3.6 to calculate the plasma temperature from the absolute line intensity of the 579.07 nm mercury emission line. Lamp 19 (10.0 mg Hg with DyI_3) is

chosen to be fully analyzed to show the validation of the method presented in section 3.6, because the best measurements were performed on this lamp.

First, after the subtraction of the dark background and the straightening of the emission line, the lateral line intensities are determined with the use of the fitting routine fit579.ogs. After that, some data points are corrected for the slit imperfections with the correction factors calculated in the previous paragraph. This is visualized in Fig. 6.8.
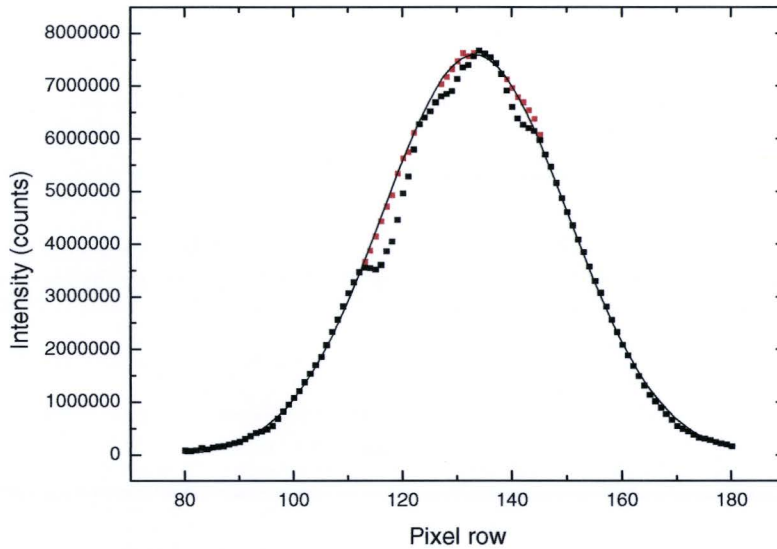

Figure 6.8: *Lateral line intensity of the 579.07 nm Hg line of a Dy lamp with 10.00 mg Hg. (lamp 19) during a micro gravity phase. The red points again are the corrected data points.*

In Fig. 6.8 we can clearly see that the correction factors are very well determined. The correction factors determined with the pure mercury lamp applied on the data points of lamp 19, give a very smooth line intensity profile. Again a Gaussian fit is used to fit the corrected data points, visualized by the black line in Fig. 6.8. This fit also gives us the pixel row corresponding to the center of the discharge (i.e. the highest mercury line emission), which in this case is pixel row 137.

To convert the (corrected) measured lateral line intensities to absolute lateral line intensities in $[Wm^{-2}sr^{-1}]$, the conversion parameter β (Eq. 3.28) has to be determined. Therefore, the pure mercury lamp which was measured with the Spechelle (lamp 18), was calibrated with a tungsten ribbon lamp with a known spectral radiance employing the Jobin-Yvon HR 640 spectrometer at Philips CDL, using the exact same lamp driver and lamp power as used in the PFC. The top of the 579.07 nm mercury emission line from the center of lamp 18 proved to have a spectral radiance of 3138 $Wm^{-2}sr^{-1}nm^{-1}$. With Eq. (3.28) and the following values, valid in the center of the discharge, the conversion parameter β can be calculated.

- $L_{top\ of\ 579.07}$ = 3138 $Wm^{-2}sr^{-1}nm^{-1}$
- $\Delta\lambda_{pixel}$ = 4.024·10^{-3} nm (order 42, 576.709 - 583.148 nm)
- $t_{shutter}$ = 0.500 s.
- *Fitted top of the 579.07 nm line* = 34080 counts

The value of β determined in this way is $2.964 \cdot 10^{-4}$ counts^{-1}sWm^{-2}sr^{-1}. Note that this value is calculated with neutral density filter 3 (1.00 % transmission) used for the Spechelle measurement of the pure mercury lamp. Because this filter is also used with the lamp under study (lamp 19), no correction has to be made. However, when an other neutral density filter is used for Spechelle measurements of other lamps, the conversion parameter β has to be corrected accordingly.

With the use of Eq. (3.30c), (3.31) and (3.32), the graph presented in Fig. 6.9 can be obtained from the fit of the corrected measurements shown in Fig. 6.8. Because the Gaussian profile is symmetric, only positive lateral positions are shown.

This absolute line intensity profile is then Abel inverted, following the procedure presented in section 3.5. The resulting Abel fit (Eq. 3.21) of the measurement data is also visible in Fig. 6.9. Note that because the measured intensities should be zero for $x > \sim 2.25$ mm, the Abel fit had to be forced to be zero in this region by adding extra "zero's" for $3.0 < x < 4.0$ mm. Otherwise the Abel fit can have negative values in that region, which is, of course, physically not possible.
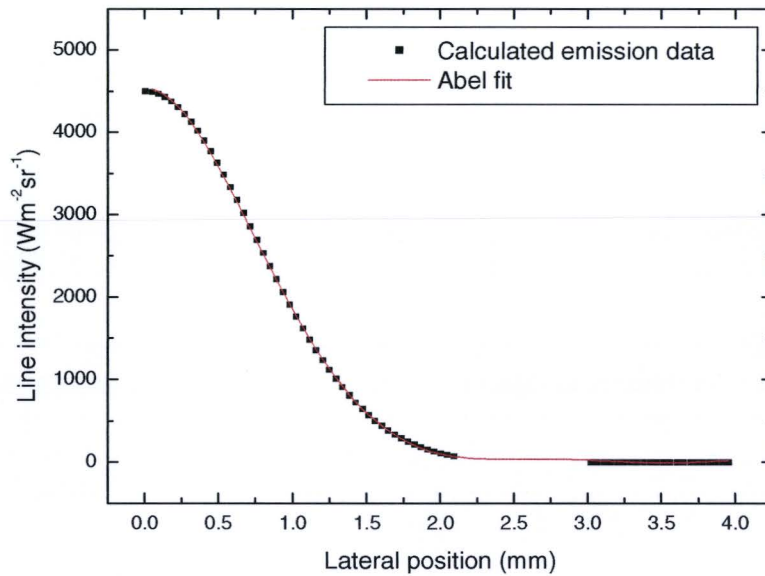
Figure 6.9: *Calculated absolute line intensities of the 579.07 nm Hg line of lamp 19 during micro gravity phase as a function of the lateral position. Extra zeros are added to the data points in the outer region of the burner to force the Abel fit to be zero after ~2.25 mm.*

Subsequently, with the use of Eq. (3.33a), the radiant power $U_{rad,579}(r)$ of the 579.07 nm mercury emission line as a function the radius can be calculated. This is shown in Fig. 6.10.
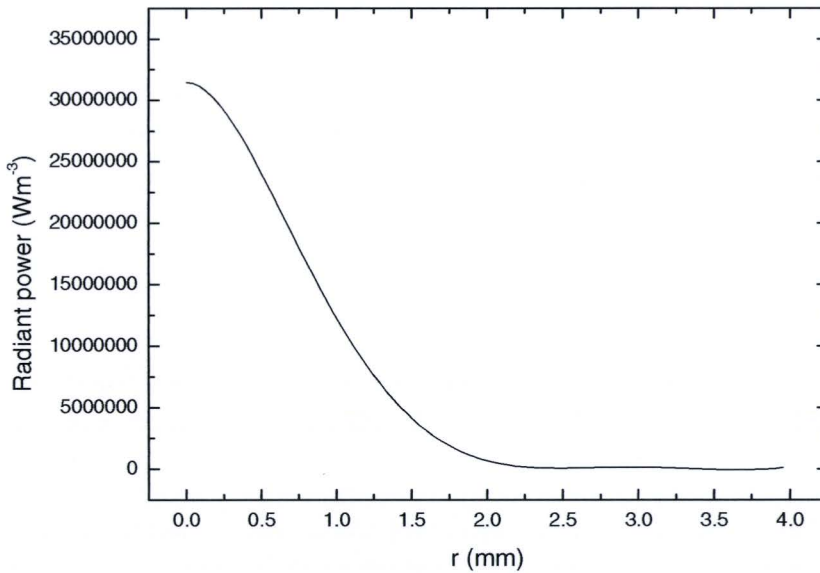
Figure 6.10: Result of the Abel inversion of the data shown in fig. 6.9. Note that the corresponding shape of this graph and the graph in fig. 6.9 is only because of the monotonically descending value of the data.

Again, when following the procedure presented in section 3.6, we are able to calculate the according plasma temperatures. To facilitate the numerical calculation of the plasma temperatures, including the iterative process of calculating a new effective temperature each iteration, a new software program has been developed. The program is baptized the "T-profile Calculator", and its source code and appearance can be found in Appendix A.VI. Next, the use of this program and the way of calculating a temperature profile with the program is discussed.

First, with the found fit coefficients c_0 through c_6 (Eq. 3.19) for the emission as a function of the radius, a set of discrete values is generated for a radius interval for which significant radiant powers are calculated. Because at every temperature some radiation is emitted (however very little at lower temperatures), the calculated values of the radiant power close to zero, cannot be used. This would introduce major errors in the calculation of the corresponding temperature, due to the inaccurate determination of very small line intensities beyond r=2.0 mm. This is why the r-position of the last used data point has to be given to the program. The amount of data points for the used radius interval presented to the program is in this way free to choose. We chose the last significant radiant power measurement for lamp 19 at r=1.64 mm.

Furthermore, the effective mercury dose and the initial effective temperature have to be entered in the program. The effective mercury dose is not equal to the actual mercury dose in the burner, because the total burner volume is larger than the actual discharge volume, which is situated between the electrodes. A calculation of the effective mercury dose is presented in Appendix C. The calculation shows that a percentage of 62% of the actual mercury dose is a good estimate for the effective mercury dose in the discharge volume. The initial effective temperature is set to 3000 K. The resulting mercury

pressure is automatically calculated by the program using Eq. (3.34) and presented on the screen.

So, when an input file (with the discrete values of $U_{rad,579}(r)$ in the chosen radius interval) is selected, the effective mercury dose is set, the right radius for the last used data point and the initial effective discharge temperature are set, the calculation of the corresponding temperatures can be started by clicking the "Calculate T(r)"-button (again, the screen layout of the program can be found in Appendix A.VI). The temperatures are calculated with Eq. (3.1) and a numerical procedure called the *Bisection method.* This simple numerical method calculates the corresponding temperature with an iteration process. In every iteration step the radiant power is calculated for a certain temperature. A certain step size is then added to this temperature every iteration, until the calculated radiant power exceeds the measured value. Then the step size is multiplied by 0.5, and the iteration process calculates the radiant power for decreasing values of the temperature. If the calculated radiant power is lower as the measured value, the step size is again multiplied by 0.5. This process is repeated until the temperature step size is below a certain value. With this method, the temperatures corresponding to all the given radiant powers are automatically calculated by the program and presented graphically by a red line on the screen.

The major disadvantage of the calculation of the plasma temperature profile from the absolute intensity of a mercury emission line, is, however, that the 579.07 emission line is not detectable for x>~2 mm. This is clearly visible in Fig. 6.9. Consequently, this method only gives us information about the plasma temperature for a small region of the burner radius.

Therefore, for the temperatures in the outer part of the burner, the calculated temperature profile has to be extrapolated. Fischer [8] introduced a temperature profile expression for high pressure discharges:

$$T(r) = T_{wall} + T_1(1-r^2) + T_2(1-r^2)^\gamma,\qquad(6.1)$$

where γ denotes the amount of *contraction* of the discharge, and T_1 represents the temperature where the contracted and parabolic profile connect. T_2 then determines the maximum temperature in the center of the discharge ($r=0$). This expression is used to extrapolate the calculated temperatures of the inner part of the burner. The meaning of the contraction of the discharge is explained later in this section. If the value of γ is 1, the discharge has a parabolic shape, which means that the discharge is not contracted.

The program T-profile Calculator is equipped with the temperature model of Fischer and is able to show this temperature profile graphically on the screen with a green line. The wall temperature is set to 1200 K, which is a real value, and the axis temperature is deduced from the calculation of the temperatures in the inner part of the burner. Because the user is able to vary the contraction parameter γ and the ratio of T_1 and T_2, the user is able to change the temperature profile in such a way, that it overlaps the calculated temperatures given by the red line. The program automatically calculates the effective temperature corresponding to the model parameters, if one of the parameters is changed, and shows this value on screen. If this effective temperature differs from the initial estimated 3000 K, used for the calculation of the temperatures, the chosen

effective temperature has to be adjusted. If this effective temperature is changed, immediately all the calculations are performed again by the program. The effective temperature has to be adjusted until it corresponds with the effective temperature derived from the Fischer temperature profile model. With the use of the T-profile Calculator, the temperature profile of a lamp can be determined very easily when a set of radiant powers as a function of the burner radius is given.

An example of the in this way determined temperature profile of lamp 19 is shown in Appendix A.VI.

When this procedure is performed for lamp 19 in a micro-gravity and hyper-gravity (2g) situation, and a "cigar" shaped Ce lamp during micro-gravity, the temperature profiles as shown in Fig. 6.11 can be obtained.
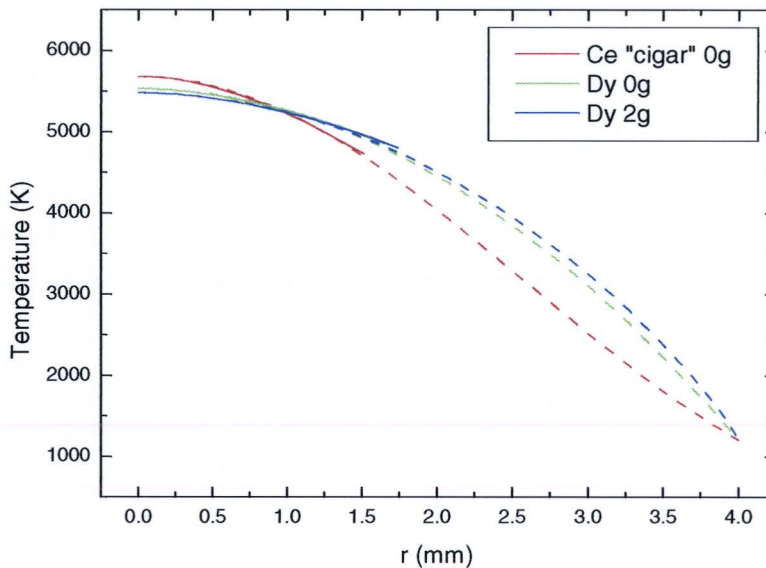

***Figure 6.11**: Calculated temperature profiles of a 0g and 2g situation of lamp 19 (Dy), and a 0g situation of lamp 12 (Ce). The solid lines indicate the calculated temperatures corresponding with the absolute line intensity of the 579.07 Hg line. The dashed lines indicate the estimated temperatures from continuation of the solid lines with the temperature model of Fischer.*

The difference in temperature profile between the Dy lamp and the cigar shaped Ce lamp can be explained by the explanation of the contraction of the discharge. Because in a cigar shaped burner the cold spot temperature is much higher as compared to a cylindrical shaped burner, the additive pressure above the salt pool is also much higher. As a result, the partial atomic additive pressure in the discharge is higher, and therefore much more radiation is leaving the plasma. Because of the extra loss of energy by means of the emission of radiation, the temperature will be slightly reduced, and the discharge becomes contracted. This is visualized in Fig. 6.12.

Because the conducting plasma channel becomes narrower in a contracted discharge, the conductivity of the channel decreases, which results in a larger energy dissipation in the center of the discharge. This is why the axis temperature is slightly higher in a contracted discharge. This is also visible in Fig. 6.11.
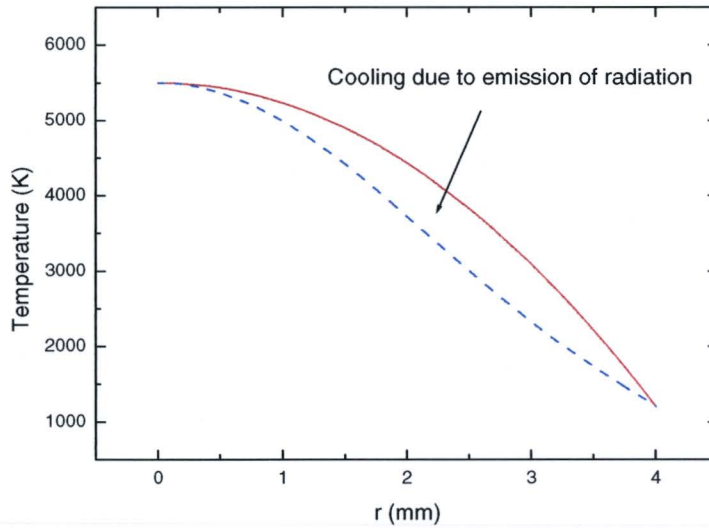
Figure 6.12: *Contraction of the temperature profile due to escape of radiation.*

The calculated temperature profiles of the Dy and Ce lamps correspond to the expected temperature profiles, being slightly colder than the temperature profile in a pure mercury discharge as calculated by Elenbaas [5].

6.1.5 Calculation of relative salt densities

Now the plasma temperature profile can be determined, we are able to construct the radial additive density profiles, if the additive line emission intensity as a function of the radius is known. To obtain the additive line intensity as a function of the radius, we start to analyze the Spechelle measurement performed with the 640 nm interference filter. With the use of fit642.ogs, as discussed in section 6.1.2, we can obtain the lateral line intensity of the optically thin 642.19 nm dysprosium emission line as a function of the lateral position. The correction factors, as discussed in section 6.1.3 are again used to correct for the entrance slit imperfections. This is visualized in Fig. 6.13, where the black dots represent the determined line intensities, and the red dots represent the corrected data points. Unlike the measurements of the 579.07 nm mercury emission line intensities, the dysprosium emission line intensity profile is not a very smooth profile. The corrected data points only correct the clearly visible dips partially.

Because the center of the discharge of a lamp can be accurately found by the maximum emission line intensity of the 579.07 nm mercury line, the pixel rows can easily be transformed to lateral positions, which is already done for the graph in Fig. 6.13.
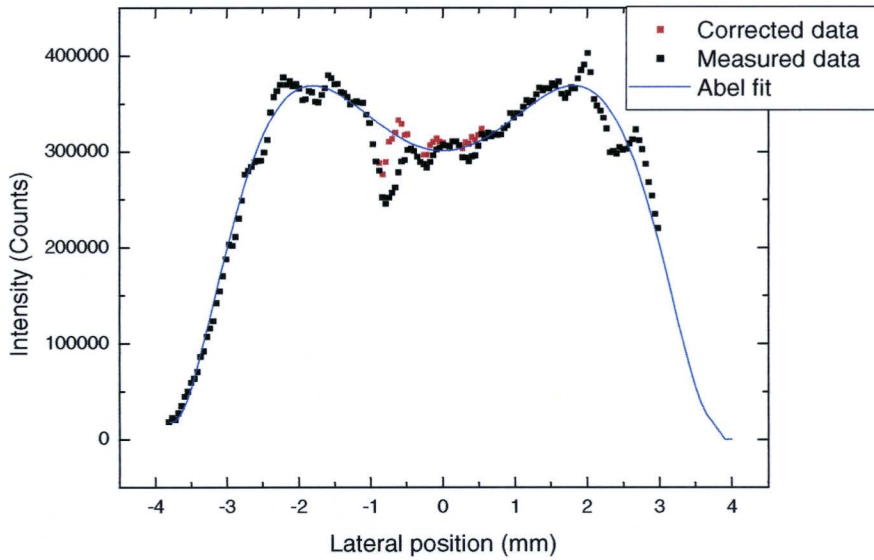
Figure 6.13: *Lateral line intensities of the 642.19 nm Dy line over the burner diameter during microgravity. The red points represent the corrected data points.*

The data points are averaged around the center of the discharge by fitting the data points with a polynomial fit with only even factors. This fit is visualized by the blue line in Fig 6.13. Because the Abel fit can follow this polynomial fit very accurately, this blue line is called Abel fit. For the actual Abel fit, only fitted values for the positive lateral positions are used.

The resulting additive emission line intensity as a function of the burner radius for a micro-gravity and a hyper-gravity situation of lamp 19 is presented in Fig. 6.14.

Figure 6.14: *The calculated line intensity of the 642.19 nm Dy line of lamp 19 as a function of the radius of the burner in a 0g and 2g situation.*

Note that because there was no possibility of calibrating the Spechelle for this wavelength, the emission line intensity is presented in arbitrary units. However, since we are, for the moment, only interested in the relative additive density distribution, this is not a problem.
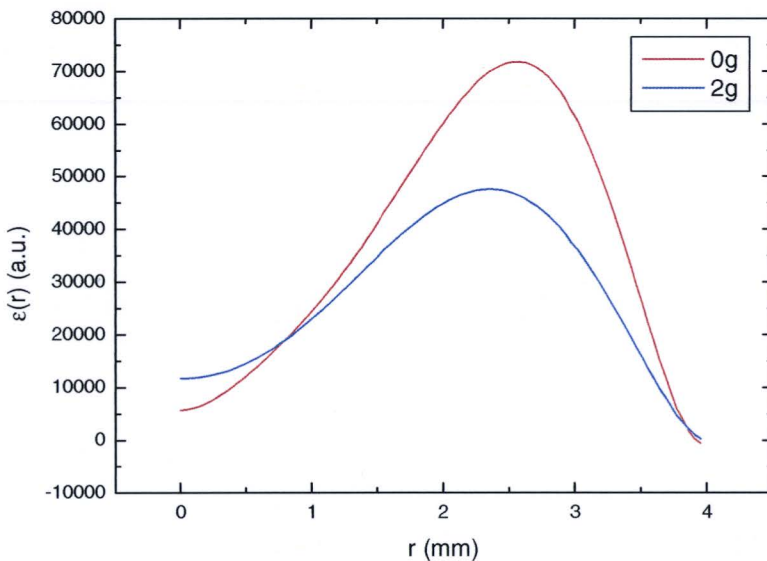
In Fig. 6.14 we see that the emission line intensity of the atomic dysprosium is still significant for $r>3$ mm. The temperature (see Fig. 6.11) is however relatively low in that region. Thermodynamic calculations with Chemapp [17], performed by M. Haverlag, give the partial atomic dysprosium pressures as shown in Fig. 6.15. These calculations can only be used as an indication, because in the calculations is assumed that the overall elemental pressure is constant, which is due to segregation phenomena not valid in the plasma under study. Because the exact cold spot temperature is not known for the used lamps, the calculation is performed for two cold spot temperatures, i.e. 1000 and 1100 K.

From 6.14 we can deduce that the atomic dysprosium pressure drops very fast near the 2000 K. We see that for both cold spot temperatures, the atomic partial pressure is close to zero in the region near the estimated wall temperature of 1200 K. In Fig. 6.14 is however visible that still a significant amount of radiation from the atomic dysprosium is emitted by the plasma in that region. Presumably, the calculated emission line intensities near the burner wall, are a little too large, probably caused by scatter of the burner wall.
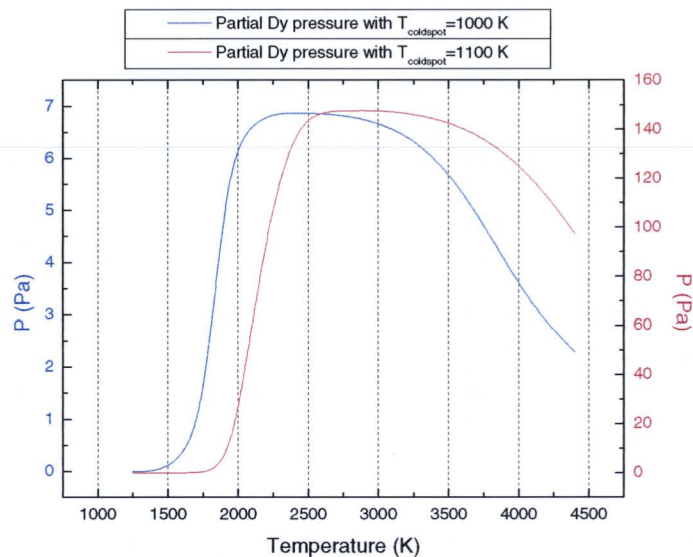
Figure 6.15: *The partial pressure of atomic Dy as a function of temperature for a system in which the total amount of Dy is constant (mixed situation). This is shown for two different salt pool temperatures. Note that a second y-axis is used for the red graph.*

With the additive line intensity as a function of the radius and the temperature profile given, we can calculate the relative atomic additive density distribution with Eq. 3.38. For that, however, we also need an expression for the partition function $Q_{Dy}(T)$ of dysprosium. Therefore we obtained from [23] 11 values of $Q_{Dy}(T)$ for the temperature interval 1000-6000 K, and fitted these data points with a fourth order polynomial fit,

which interconnects the data points accurately. The found expression used for the calculation of the partition function of dysprosium is:

$$Q_{Dy}(T) = 15.39 + 2.63 \cdot 10^{-3}T - 1.43 \cdot 10^{-6}T^2 + 4.26 \cdot 10^{-10}T^3 - 8.29 \cdot 10^{-15}T^4 \quad (6.2)$$

The resulting atomic additive density profiles for a micro-gravity and hyper-gravity situation are presented in Fig. 6.16. The significant line intensity measured near the burner wall, combined with the lower temperature in that region, result in an possible overestimation of the calculated density. This is indicated by the cross-hatched area.
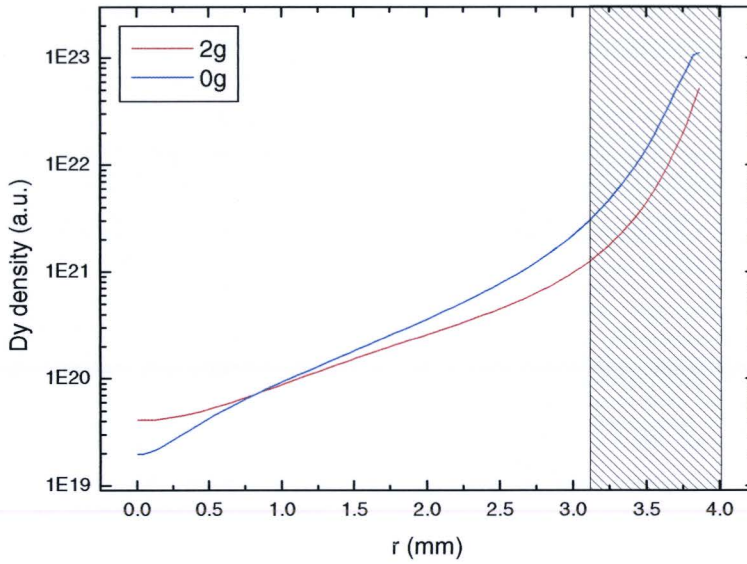
Figure 6.16: *The calculated Dy density distribution for a 0g and 2g situation of lamp 19. The cross-hatched area indicates that the values calculated in that region are probably not reliable.*

The calculated densities in the non-cross-hatched area are however very promising. The clearly visible difference between the micro-gravity and hyper-gravity situation corresponds with the expected trends. The expectation that in the hyper-gravity situation the radial segregation would reduce is clearly proven. The differences between the density in the center of the discharge and the density near r=3 mm, corresponds to the expected difference caused by the temperature difference which affects the chemical equilibrium and the gas density via the ideal gas law, combined with the radial segregation effects.

6.1.6 Estimation of errors

In order to get an idea of the sensitivity for errors of the introduced method to calculate plasma temperatures, we take a look at the propagation of errors in the calculation process and present the major sources for errors.

We can determine the following major sources of errors and their estimated maximum error.

- Error in the effective mercury dose, 21% (Appendix C).
- Error in the automatically determined line intensity, 5%.
- Error in the absolute radiance calibration procedure, 10%.
- Error in the used transition probability of the 579.07 nm mercury emission line.

The error in the transition probability A needs some further discussion. The value for A used in all the performed calculations is $2.04 \cdot 10^8$ s^{-1}, which is obtained from the Kurucz Atomic Line Database [29]. Recently, it was discovered that this value is not consistent with other literature sources. Stormberg [40] uses a completely different value of $4.58 \cdot 10^7$ s^{-1} for this transition probability. Other sources report transition probabilities of the 576.76 nm mercury emission line, which originates from the same upper energy level and has a comparable line intensity, of $2.36 \cdot 10^7$ s^{-1} [32] and $5.84 \cdot 10^7$ s^{-1} [40]. So, it is very well possible that the actual transition probability is only 22% of the transition probability used in all our calculations. Due to the fact this possible error was only discovered just before the final version of the report had to be finalized, we have chosen not to repeat all calculations, but to investigate the deviation caused by this possible error.

To see what the effect of these errors (mercury dose, line intensity, calibration, transition probability) is on the calculated temperature profile, we calculated the effect of an error of 10% in one of the described sources of errors. Because all the sources of errors have the same effect on the calculated temperature (see Eq. 3.1), we can calculate the effect by changing the effective mercury dose in the program T-profile Calculator. It appeared that an error of 10% only results in a deviation of the axis temperature of 28 K. (from 5528 K to 5500 K). If instead of the used value for the transition probability ($2.04 \cdot 10^8$ s^{-1}), the most probable value ($4.58 \cdot 10^7$ s^{-1}) is used, the axis temperature changes form 5528 K to 6030 K. The shape of the temperature profile is not affected noticeable. So, probably, all the calculated temperature profiles present an axis temperature which is roughly 500 K too low.

The calculation of the influence of errors on the calculated temperature profile shows something remarkable. Severe errors only result in slight changes of the calculated temperatures. Due to the use of the 579.07 nm mercury emission line, which has a very high upper energy level of 8.85 eV, the emission of this emission line is extremely temperature dependent. Slight changes in the plasma temperature result in major changes in the emitted radiation of the 579.07 nm line. This is why the use of this method for calculating plasma temperatures is very robust.

However, we have to keep in mind that with all the calculations Local Thermal Equilibrium (LTE) is assumed. Especially near the burner wall this probably not the case. This is possibly also a reason for the calculated densities in the cross-hatched area of Fig. 6.16 being overestimated. If the electron temperature exceeds the gas temperature, which is used in the calculation, an overestimation of the calculated densities can be expected.

6.2   Parabolamp

In this section the results of the measurements performed with the Parabolamp experiment are presented and discussed qualitatively. In Appendix B the exact performed measurement sequence can be found.

6.2.1 *Gravity dependence of the visible light output*

As described in section 2.5, we expect changes in the luminous output of a burning metal halide lamp while varying gravity. The typical measurements shown in Fig. 6.17 prove that this is the case, and that the changes in luminous output are reproducible. We can clearly see the occurrence of the micro-gravity periods every three minutes, with both positive and negative effects on the luminous output of the two different lamps. In the graph shown on the right of Fig. 6.17, the negative influence of the hyper-gravity period before and after the micro-gravity period on the luminous output can also be seen.
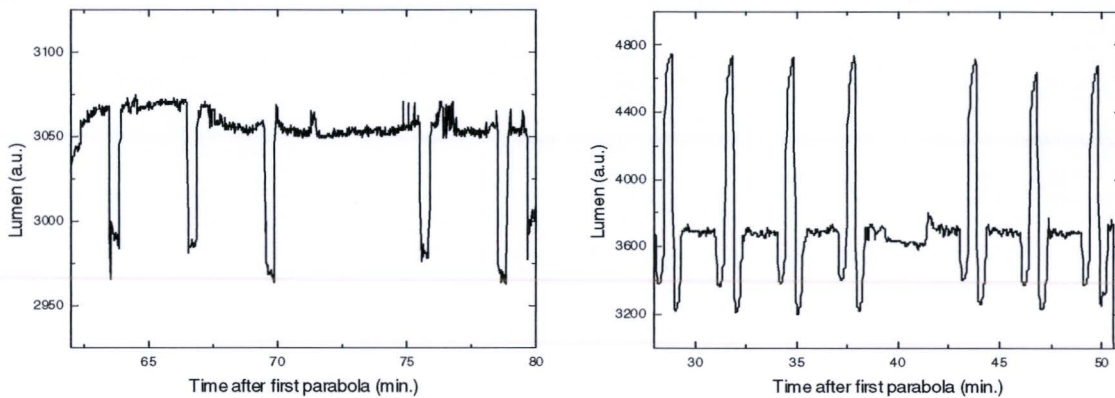
Figure 6.17: *Two graphs showing the change in luminous output during g-transitions. The "peaks" visible in both graphs are 0g situations. The graph left shows the luminous output of lamp 43 (NaTlDyI) in a horizontal burning position. The graph on the right illustrates the behavior of lamp H1 (NaCeI) in a vertical burning position. It is clearly visible that the changes are reproducible.*

Because the hyper-gravity situation is not well defined during a parabolic flight, due to significant differences in the experienced gravity in that period, only the difference in luminous output of a lamp in a micro-gravity situation is compared with the normal luminous output. The average change in luminous output in a micro-gravity situation compared with a normal situation for all measured lamps in both horizontal and vertical burning position is shown in Table 6.1.

lamp:	Difference 0g - 1g in %				
	CDM NaDyl	*CDM NaTlDyl*	*CDM NaTlCal*	*CDM NaTlCal & Cel₃*	*Helios with NaCel*
horizontal	-2.5	-2.9	-1.9	-4.7	+8
vertical	+4.0	0.0	+2.2	-2.2	+25

Table 6.1: *Relative changes in luminous output in the 0g phase with respect to 1g situation for all lamps in both horizontal and vertical burning position. The relative error in the size of the measured changes is about 10-20 %.*

To determine the differences in luminous output between horizontally and vertically burning of the lamps, Table 6.2 presents the luminous output of the measured lamps in both burning positions.

lamp:	Luminous output (a.u.)				
	CDM NaDyl	*CDM NaTlDyl*	*CDM NaTlCal*	*CDM NaTlCal & Cel₃*	*Helios with NaCel*
horizontal	2475 ± 25	3060 ± 25	2600 ± 75	3000 ± 25	4500 ± 150
vertical	2325 ± 25	3000 ± 25	2475 ± 50	2925 ± 25	3700 ± 200

Table 6.2: *Luminous output of the measured lamps under normal gravity conditions in both vertically and horizontally burning position.*

The interpretation of these results will be discussed in section 6.2.3.

6.2.2 A closer look at the processes during g-transitions

When we take a closer look at the change in luminous output as a function of time (and thus gravity), we typically obtain a graph like is shown in Fig. 6.18. Especially the Helios burners show a significant and consistent behavior during gravity transitions, so that is why we now will concentrate on the Helios burners.

The graph presented in Fig. 6.18 concerns a vertically burning Helios lamp, and we see that the luminous output (at constant power input) increases as an exponential function with a certain time scale. This suggests a diffusion driven increase of the luminous output. This is exactly as predicted in section 2.5. Presumably, in this lamp considerable axial segregation emergences and in the micro-gravity phase, when the convection flow stops, the additives are able to diffuse to the upper part of the discharge, where they previously were absent, resulting in an increase of the luminous output. We also see that in the hyper-gravity phase, the luminous output is reduced. The expectation that this type of lamp is positioned just at the left of the maximum of the Fischer curve is therefore correct. When increasing the gravity, the axial segregation increases too, resulting in a decrease of luminous output, while in the micro-gravity phase, the axial segregation disappears and the luminous output increases significantly. Even the time scale of the diffusion process canceling the axial segregation can be determined from Fig. 6.18.
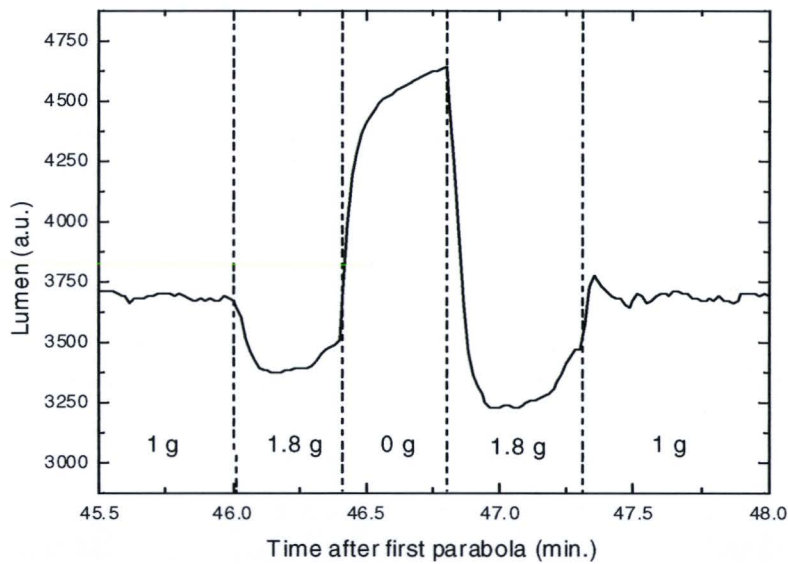
Figure 6.18: *The visible light output of lamp H1 burning vertically during parabola #12.*

However, the luminous output of a horizontally burning lamp shows a completely different behavior, as can be seen in Fig. 6.19. Again the luminous output as a function of time is given for a Helios lamp, this time burning horizontally.
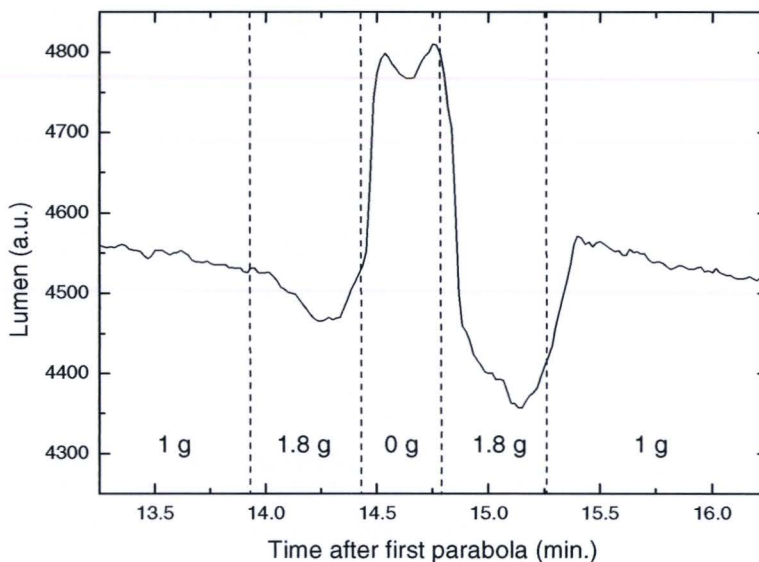
Figure 6.19: *The visible light output of lamp H1 burning horizontally during parabola #4.*

In contrast with the measurement shown in Fig. 6.18, the luminous output of a horizontally burning lamp almost immediately reaches a higher value, when the micro-gravity phase is entered. This indicates that the change in luminous output is not caused by diffusive effects. As discussed in section 2.5, these diffusive effects would furthermore cause the luminous output to **decrease**, due to the canceling of the

convective mixing. This appears not to be the case. So the effects visible in Fig. 6.19 are caused by an effect which is not taken into account in the discussion in section 2.5, which is arc bending. Due to the high aspect ratio, and thus relatively small burner diameter, the discharge is positioned close to the burner wall. In the presence of gravity, convection-driven arc bending manifests (see section 2.4), introducing significant energy losses to the close-by burner wall. When entering a micro-gravity phase, the convection flow causing the arc bending immediately stops, and the wall losses also disappear immediately.

With the changes in luminous output during gravity transitions, the measured effects can be explained qualitatively for the Helios lamps. In the next section, the changes in the luminous output for the rest of the lamps is discussed qualitatively.

6.2.3 Qualitative explanation of measured effects

As is shown in Table 6.1, changes in the luminous output between the micro-gravity and normal situation differ much mutually for the measured CDM burners with the different additives used. Unlike with the Helios burners, the effects can not be explained by looking closely to the luminous output as a function of time.

First, we will discuss the changes in luminous output for horizontally burning lamps with a CDM-type burner. We see that, in contrast with the Helios burners, the luminous output is lowered in a micro-gravity situation. Apparently, the qualitative discussion in section 2.5, which predicts this effect, is useful for this type of burner. Due to the aspect ratio of 1, resulting in a relatively large burner diameter, the arc bending of the discharge does not result in significant energy losses in the 1g situation. But due to the mixing in a 1g situation by convection flows, which are relatively strong due to the large burner diameter, the radial segregation of additives is reduced, and the luminous output of the lamp burning under normal gravity conditions is larger than the luminous output in a micro-gravity situation, where the radial segregation is maximized. The mutual differences in luminous output change of horizontally burning CDM-type lamps are caused by the different diffusion processes and the different type of radiation of the different additives.

For the vertically burning situation, we see both positive and negative changes in the luminous output of the CDM-type burners. Apparently, these lamps are positioned, as expected, on the right hand side of the Fischer curve (like lamp Y in section 2.5) , where the convective mixing reduces the radial, and thus axial, segregation. Because of the use of different additives, the balance between convective mixing and axial segregation opens out in a positive change of the luminous output in a micro-gravity situation for one type of additive, and a negative change for an other type of additive.

The measurement values presented in Table 6.2 show that the prediction that a horizontally burned lamp always has a higher luminous output than the same lamp burned vertically, is correct for all cases investigated.

7 Conclusions and Recommendations

7.1 Conclusions

- The presented method for calculating the radial plasma temperature profile of quartz metal halide lamps with the absolute intensity profile of the optically thin 579.07 nm mercury emission lines has proven to be very suitable and gives reliable plasma temperature profiles.

- The calculated radial atomic dysprosium density profiles show the expected behavior for a lamp in a micro-gravity and a hyper-gravity situation. The calculation of the densities near the wall are somewhat overestimated, possibly due to scatter on the burner wall, and non-LTE properties of the plasma near the burner wall.

- The developed fitting routines for Microcal Origin 6.0 have proven to successfully execute the automatic determination of the lateral line intensities of both the mercury 579.07 nm emission line and the 642.19 nm dysprosium emission line.

- The developed software programs for automatic dark background measurement subtraction and emission line straightening speed up and simplify the measurement analysis procedure significantly.

- The developed software program "T-profile calculator" proved to be very convenient for numerical calculation of the plasma temperature profiles, and the extrapolation of the calculated temperatures to the burner wall, with the temperature model of Fischer.

- The saturation problems encountered during the previous Parabolic Flight Campaign (PFC) have successfully been resolved for both the ARGES prototype setup and the final International Space Station (ISS) experimental setup.

- The new cylindrically shaped burner design succeeds in preventing the liquid additive from covering the inside of the burner wall, which would cause the spectroscopic measurements to be disturbed.

- A new experimental setup, baptized the "Parabolamp experiment", has successfully been developed and constructed with the aim of measuring the integral luminous output of ceramic metal halide lamps, burning both vertically and horizontally, as a function of time, and thus of gravity, when attending a parabolic flight.

- With the use of segregation and arc bending effects, the measured changes in integral luminous output of several types of lamps have been explained qualitatively.

7.2 Recommendations

- Because of the limited flight time available in the PFC, the performed measurements were restricted to the lamp power of 150 W. The longer measurement time available in the ISS poses the opportunity to measure the plasma properties at different power levels of the burning lamp. This can give more information about the processes inside the plasma.

- Also due to the limited measurement time available in the PFC, no ionic emission lines have been measured. The ISS experiment however poses the possibility to also measure these emission lines, to investigate the ionization processes in the plasma of metal halide lamps.

- Other methods to determine the plasma temperature profile should be used, to be sure that the calculated temperature profiles are exactly correct. With the use of the Bartels method, the absolute intensity of self-reversed mercury emission lines can be used to calculate the plasma temperatures. The Boltzmann temperature determination method showed to give incorrect plasma temperatures in a previous study. However, recently it was discovered that the second dysprosium emission line used in that study, actually consists of two emission lines, separated only by a very small wavelength difference. The 643.655 nm and the 643.673 nm emission lines were assumed to be one single spectral line, because the Spechelle is not able to resolve these two lines. This probably caused the major errors in the calculated temperatures. Consequently, the Boltzmann method might still be a suitable method to determine plasma temperatures, provided that accurate data is available for transition probabilities. Input from experts (e.g. J. Lawler) in this field is therefore recommended.

- The prevention of saturation of the CCD causes the less intense additive emission lines to have relatively small intensities in the measurements. If these emission lines would be used for the Boltzmann method, the measurement of these additive emission lines with larger shutter times should be reconsidered.

Bibliography

[1]   Akker, D. v.d., *The design of a tunable diode laser absorption spectroscopy setup for measuring salt additives in metal-halide lamps in micro-gravity conditions,* Philips Trainee Report CDL 03/40010 (2003).

[2]   Andover Corporation, http://www.andcorp.com

[3]   Bax, M., *The design of a high resolution emission spectrometer for microgravity experiments on metal halide lamps,* Philips Trainee Report CDL 03/40009 or TU/e EPG 03-09 (2003).

[4]   Benck, E.C., Lawler, J.E., and Dakin, J.T., *Lifetimes, branching ratios, and absolute transition probabilities in Hg I,* J. Opt. Soc. Am. B **6** 11-22 (1989).

[5]   Elenbaas, W., *High pressure mercury vapour lamps and their applications,* Centrex, Eindhoven (1965).

[6]   Elenbaas, W., *The high pressure mercury vapour discharge,* North-Holland, Amsterdam (1951).

[7]   Fischer, E., *Axial segregation of additives in mercury-metal-halide arcs,* J. Appl. Phys. **47** 2954-2960 (1976).

[8]   Fischer, E., *Influences of External and Self-Magnetic Fields on the Behaviour of Discharge Lamps,* Philips GmbH Forschungslaboratorium Aachen Lobornotiz nr. 13/78 (1978).

[9]   Geijtenbeek, J.J.F., *The origin of demixing,* Philips Technical Note CDL 01/20125 (2001).

[10]   Groot, J.J. de, and Jack, A.G., *Plasma temperature measurements using self-absorbed spectral lines: A discussion of the methods due to Bartels and Kruithof,* J.Quant.Spectr.Rad.Transf. **13** 615-626 (1973).

[11]   Groot, J.J. de, and Vliet, J.A.J.M. van, *The high-pressure sodium lamp,* Kluwer Technical Books, Deventer (1986).

[12]   Haverlag, M., *An energy balance model for HID lamps including 2-D radiation transport,* Philips Report CDL 03/xx (2003).

[13]   Haverlag, M., SAD Calculations of Dy densities, Philips CDL.

[14]   Haverlag, M., *Segregation of HID lamps; a literature study,* Philips Report CDL 01/10030 (2001).

[15]   Hirschfelder, J.O., Curtiss, C.F., and Bird, R.B., *Molecular Theory of Gases and Liquids,* Wiley, New York (1954).

[16]   Hout, F. van den, *Master Thesis (to be publised),* Philips Trainee Report CDL (2004).

[17]   http://gttserv.lth.rwth-aachen.de/~sp/tt/index.htm

[18]   http://www.esa.int

[19]   http://www.esa.int/SPECIALS/Delta_Mission

[20]   http://www.novespace.fr

[21] http://www.phys.tue.nl/EPG

[22] http://www.phys.tue.nl/tuedacs

[23] http://www.thespectroscopynet.com/Theory/Partition_Functions.asp

[24] http://www.tuedacs.nl

[25] Karabourniotis, D., *Nonequilibrium excited-state distribution of atoms in dense mercury plasmas*, J. Appl. Phys. **92(1)** 25-31 (2002).

[26] Kemenade, Marc van, *Master Thesis (to be publised),* TU/e EPG 04-xx (2004).

[27] Kemps, P.C.M., *First Results of Testing of the Space-Optics*, ESA document DSM-ARG-801 (2003).

[28] Körber, A., *A simple delta lambda method for measurements of element pressures illustrated by application examples to HID lamps*, Aachen report PFL 1322/98 (1998).

[29] Kurucz Atomic Line Database, http://cfa-www.harvard.edu/amdata/ampdata/kurucz23/sekur.html.

[30] Labsphere, *A Guide to Integrating Sphere Theory and Applications*, http://www.labsphere.com/tech_info/docs/IS_Theory_Application.pdf

[31] Lochte-Holtgreven, W., *Plasma diagnostics*, North-Holland, Amsterdam (1968).

[32] National Institute of Standards and Technology, *Physical Reference Database*, http://physics.nist.gov/PhysRefData/contents.html.

[33] OriginLab Corporation, *LabTalk Developer's Guide*, http://www.abo.fi/fak/ktf/ank/Documents/datank/Labtalk%20Development%20Guide.pdf.

[34] Pedrotti, F.L., and Pedrotti, L.S., *Introduction to optics* (*second edition*), Prentice-Hall, London (1993).

[35] Philips Lighting BV, *Introduction guide to Philips HID lamps*, booklet 3222 635 12571 (1996).

[36] Schiffelers, G., *Study of gravity dependent radial de-mixing in metal halide lamps using spectroscopic techniques,* TU/e EPG 03-16 (2003).

[37] Software package Borland Delphi 7.0 Professional, http://www.borland.com.

[38] Software package MathSoft MathCad 11, http://www.MathCad.com.

[39] Software package Microcal Origin 6.0, *Non-linear least square fitter (NLSF),* http://www.OriginLab.com.

[40] Stormberg, H.P., and Schäfer, R., *Time-dependent behavior of high-pressure mercury discharges*, J. Appl. Phys. **54** 4338-4347 (1983).

[41] Weerdesteijn, P., and Haverlag, M., *Light-technical properties of Na:Ce lamps: experiments with burner auxiliary heating*, Philips Technical Note CDL 03/xx (2004) (*to be published).
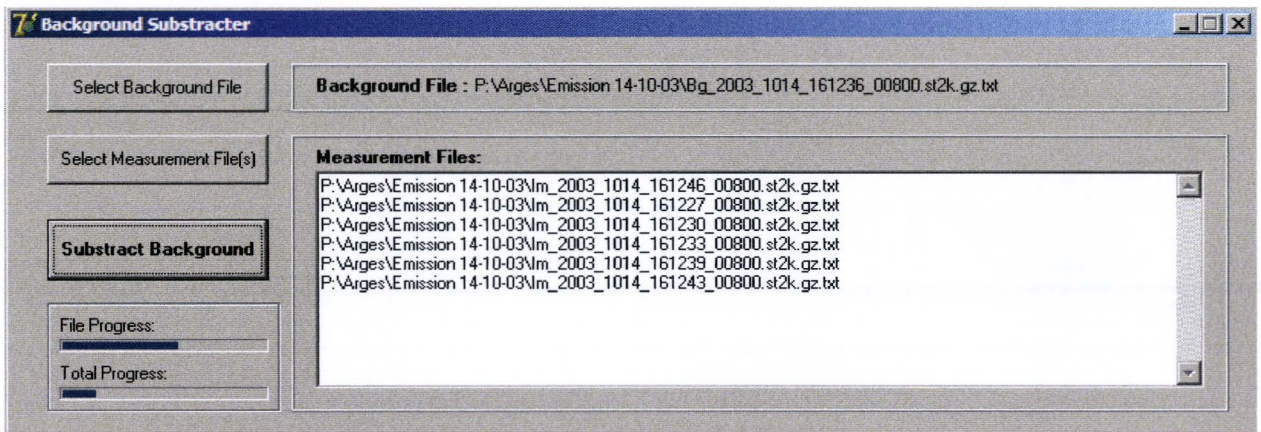
Appendix A: Developed software

A.I   Background Subtracter

Description

This program, created with [37], automatically subtracts a selected background-file from one or more measurement files. The resulting files are placed in a subfolder "without background" in folder of the measurement files.

Appearance

Source code

```
unit BackgroundF;

interface

uses
  Windows, Messages, SysUtils, Variants, Classes, Graphics, Controls, Forms,
  Dialogs, StdCtrls, ExtCtrls, ComCtrls;

type
  TForm1 = class(TForm)
    BtnSelectBackground: TButton;
    Panel1: TPanel;
    Label1: TLabel;
    LabelBackground: TLabel;
    BtnSelectMeasurement: TButton;
    Panel2: TPanel;
    Memo1: TMemo;
    Label3: TLabel;
    BtnSubstractBackground: TButton;
    OpenDialog1: TOpenDialog;
    OpenDialog2: TOpenDialog;
    ProgressBar1: TProgressBar;
    ProgressBar2: TProgressBar;
    Label2: TLabel;
    Label4: TLabel;
    Bevel1: TBevel;
```

```
    procedure BtnSelectBackgroundClick(Sender: TObject);
    procedure BtnSelectMeasurementClick(Sender: TObject);
    procedure BtnSubstractBackgroundClick(Sender: TObject);
  private
    { Private declarations }
  public
    { Public declarations }
  end;

Type
  data = array [1..200,1..1600] of integer;

var
  Form1: TForm1;
  backdata: data;
  Backname: string;
implementation

{$R *.dfm}

procedure TForm1.BtnSelectBackgroundClick(Sender: TObject);

var
  f1: textfile;
  dummy: string;
  k,i, dumint: integer;

begin
  If OpenDialog1.Execute then
  begin
    backname:=opendialog1.FileName;
    LabelBackground.Caption:=backname;
    AssignFile(f1, backname);
    reset(f1);
    readln(f1, dummy);
    for k:=1 to 1600 do
    begin
      read(f1, dumint);
      for i:= 1 to 199 do
      begin
        read(f1, backdata[i,k]);
      end;
      readln(f1, backdata[200,k]);
    end;
    CloseFile(f1);
  end;
end;

procedure TForm1.BtnSelectMeasurementClick(Sender: TObject);

begin
  if OpenDialog2.execute then
  begin
    memo1.Lines.Clear;
    Memo1.Lines.AddStrings(Opendialog2.Files);
  end;
end;

procedure TForm1.BtnSubstractBackgroundClick(Sender: TObject);
var
  f,f2:textfile;
  dummy, backfolder, measfile: string;
  i,k, m, dumint, data: integer;
  code: boolean;
```

```
begin
 if backname=" then MessageDlg('Select Background File First!', mtWarning, [mbOk], 0,)
 else
 begin
 if memo1.Lines.Count=0 then MessageDlg('Select Measurement File(s) First!', mtWarning, [mbOk], 0,)
 else
 begin
 with memo1.lines do
 begin
 progressbar2.Max:=count;
 for i:=0 to count-1 do
 begin
  Bevel1.Visible:=true;
  Label2.Visible:=true;
  label4.Visible:=true;
  Repaint;
  ProgressBar1.Visible:=true;
  ProgressBar2.Visible:=true;
  ProgressBar2.Position:=i;
  Assignfile(f, Strings[i]);
  Reset(f);
  backfolder:=Extractfiledir(Strings[i])+'\without background';
  code:=CreateDir(backfolder);
  measfile:=ExtractFilename(Strings[i]);
  Assignfile(f2,backfolder+'\'+measfile);
  Rewrite(f2);
  Readln(f, dummy);
  for k:=1 to 1600 do
  begin
   read(f, dumint);
   write(f2, dumint:6);
   for m:=1 to 199 do
   begin
    read(f, data);
    write(f2, data-backdata[m,k]:6);
   end;
   readln(f, data);
   writeln(f2, data-backdata[200,k]:6);
   ProgressBar1.Position:=k;
  end;
  CloseFile(f);
  Closefile(f2);
  ProgressBar2.Position:=Count;
  Repaint;
 end;
 end;
 end;
 end;
 MessageDlg('The Backgroud-values have been substracted.', mtInformation, [mbOk], 0,)
end;

end.
```

A.II   Emission line straightener

Description

This program, created with [37], automatically edits the selected measurement file(s) in such a way that the emission lines will be straightened. In this way the data-analyse software always finds an emission line in the same data point interval.

Appearance

Source code

```
unit StraightenF;

interface

uses
  Windows, Messages, SysUtils, Variants, Classes, Graphics, Controls, Forms,
  Dialogs, StdCtrls, ExtCtrls, ComCtrls;

type
  TForm1 = class(TForm)
    BtnSelectMeasurement: TButton;
    BtnStraighten: TButton;
    OpenDialog2: TOpenDialog;
    ProgressBar2: TProgressBar;
    Label4: TLabel;
    Bevel1: TBevel;
    ProgressBar1: TProgressBar;
    Label1: TLabel;
    procedure BtnSelectMeasurementClick(Sender: TObject);
    procedure BtnStraightenClick(Sender: TObject);
  private
    { Private declarations }
  public
    { Public declarations }
  end;

Type
  data = array [1..201,1..1600] of integer;

var
  Form1: TForm1;
```

```
  imagedata, verschuifdata: data;
  Backname: string;
implementation

{$R *.dfm}

procedure TForm1.BtnSelectMeasurementClick(Sender: TObject);

begin
 if OpenDialog2.execute then
 begin
 repaint;
 end;
end;

procedure TForm1.BtnStraightenClick(Sender: TObject);
var
 f,f2:textfile;
 folder, measfile: string;
 i,k,m,l, dumint, data, verschuiving: integer;
 code: boolean;

begin
 if OpenDialog2.Files.Count=0 then MessageDlg('Select Measurement File(s) First!', mtWarning, [mbOk], 0,)
 else
 begin
 with Opendialog2.Files do
 begin
 progressbar2.Max:=count;
 Bevel1.Visible:=true;
 label4.Visible:=true;
 label1.Visible:=true;
 Repaint;
 ProgressBar2.Visible:=true;
 ProgressBar1.Visible:=true;
 for i:=0 to count-1 do
 begin
   for k:=1 to 1600 do for m:=1 to 201 do verschuifdata[m,k]:=0; {maak array schoon}
   ProgressBar2.Position:=i;
   ProgressBar1.Position:=1;
   repaint;
   Assignfile(f, Strings[i]);
   Reset(f);
   folder:=Extractfiledir(Strings[i])+'\straightened';
   code:=CreateDir(folder);
   measfile:=ExtractFilename(Strings[i]);
   Assignfile(f2,folder+'\'+measfile);
   for k:=1 to 1600 do   {lees data in}
   begin
     for m:=1 to 200 do
     begin
       read(f, imagedata[m,k]);
     end;
     readln(f, imagedata[201,k]);
   end;
   for k:= 1 to 1600 do verschuifdata[1,k]:=imagedata[1,k];
   for m:=2 to 201 do
   begin
     verschuiving:=round(-74.59+2.077*(m-1)-0.0124*(m-1)*(m-1)+1.55E-5*(m-1)*(m-1)*(m-1));
     if verschuiving>0 then
     begin
       for l:=1 to verschuiving do verschuifdata[m,l]:=0;
       for k:=verschuiving to 1600 do
       begin
```

```
        verschuifdata[m,k]:=imagedata[m,k-verschuiving];
      end;
    end
    else
    begin
      for k:=1 to 1600+verschuiving do
      begin
        verschuifdata[m,k]:=imagedata[m,k-verschuiving];
      end;
    end;
  end;
  Rewrite(f2);
  for k:=1 to 1600 do   {schrijf data weg}
  begin
    for m:=1 to 200 do
    begin
      write(f2, verschuifdata[m,k]:6);
    end;
    ProgressBar1.Position:=k;
    writeln(f2, verschuifdata[201,k]:6);
  end;
  CloseFile(f);
  Closefile(f2);
  ProgressBar2.Position:=Count;
  Repaint;
  end;
  end;
  end;
  MessageDlg('The CCD-images have been straightened.', mtInformation, [mbOk], 0,)
end;

end.
```

A.III fit579.ogs

Description

This LabTalk-scriptfile is used in Microcal Origin 6. If a measurement file (with the 580 nm filter) is loaded into a worksheet and that worksheet is active, this LabTalk-scriptfile creates a graph with all the lateral line intensities of the 579.07 nm emission line over the burner diameter, using a Lorentz-fit procedure. (The text behind the "//" is comment). This scriptfile also makes use of the scriptfile "fit.ogs" (Appendix A.V)

Source code

```
%P=%H;
%O=Intensities; //name new worksheet
create %O -w 200 X I R2 Xc Y0 W; //create new worksheet
step=1;

begin=80; //startcolumn, ONLY EVEN NUMBERS!
end=190; //endcolumn, ONLY EVEN NUMBERS!

p1=1000; //initial fit-values, only used the first fit
p2=488;
p3=120;
p4=4000000; //after initialisation the previous values are used for start-values
p1save=p1; //save initial values
p2save=p2;
p3save=p3;
```

```
p4save=p4;
middle=begin+(end-begin)/2;

for (kk=middle; kk<=end; kk++) {analyse;};
p1=p1save;
p2=p2save;
p3=p3save;
p4=p4save;
for (kk=middle-1; kk>=begin; kk--) {analyse;};

window -a %O; //select worksheet window
worksheet -s;
worksheet -s 1 1 2 200; //select all
worksheet -p 202;  //make graph
window -r %H Lateralintensities; //rename graph window
run.section(setaxis);  //change layout of graph with procedure "setaxis", written by P.Kemps
label -xb Lateral position (x 44.4 µm); //set axis labels
label -yl Intensity (a.u.);
label -xt \b(Intensity of 579.06 nm Hg-line over burnerdiameter);
set %c -z 5; //set symbol-size to 5;

def analyse {
window -a %P;  //set previous worksheet active
worksheet -s; //unselect all
worksheet -s kk*step 200 kk*step 800;  //select peak
worksheet -p 200;  //plot selected data
//run.section(setaxis);  //change lay-out of graph with procedure "setaxis", written by P.Kemps
run h:\fit.ogs; //perform lorentz-fit
%(%O,1,kk*step)=kk*step; //write column-number to worksheet
aa=nlsf.p4;
aa=round(aa,1);
%(%O,2,kk*step)=aa; //write fit-area to worksheet
bb=nlsf.cod;  //get R^2 value
bb=round(bb,3);
%(%O,3,kk*step)=bb; //write R^2-value to worksheet
cc=nlsf.p2;
cc=round(cc,1);
%(%O,4,kk*step)=cc; //write Xc-value to worksheet
dd=nlsf.p1;
dd=round(dd,1);
%(%O,5,kk*step)=dd; //write Y0-value to worksheet
ee=nlsf.p3;
ee=round(ee,1);
%(%O,6,kk*step)=ee; //write W-value to worksheet
window -c %H; //close graph window
//type "column = $(kk*step)";
};
```

A.IV fit642.ogs

Description

This LabTalk-file is used in Microcal Origin 6. If a measurement file (with the 640 nm filter) is loaded into a worksheet and that worksheet is active, this LabTalk-scriptfile creates a graph with all the lateral line intensities of the 642.19 nm emission line over the burner diameter, using a Lorentz-fit procedure. (The text behind the "//" is comment)
This scriptfile also makes use of the scriptfile "fit.ogs" (Appendix A.V)

Source code

```
%P=%H;
%O=Intensities; //name new worksheet
create %O -w 200 X I R2 Xc Y0 W; //create new worksheet
step=1;

begin=40; //startcolumn, ONLY EVEN NUMBERS!
end=200; //endcolumn, ONLY EVEN NUMBERS!

p1=2000; //initial fit-values, only used the first fit
p2=986;
p3=7;
p4=300000; //after initialisation the previous values are used for start-values
p1save=p1; //save initial values
p2save=p2;
p3save=p3;
p4save=p4;
middle=begin+(end-begin)/2;

for (kk=middle; kk<=end; kk++) {analyse;};
p1=p1save;
p2=p2save;
p3=p3save;
p4=p4save;
for (kk=middle-1; kk>=begin; kk--) {analyse;};

window -a %O; //select worksheet window
worksheet -s;
worksheet -s 1 1 2 200; //select all
worksheet -p 202;  //make graph
window -r %H Lateralintensities; //rename graph window
run.section(setaxis); //change layout of graph with procedure "setaxis", written by P.Kemps
label -xb Lateral position (x 44.4 µm); //set axis labels
label -yl Intensity (a.u.);
label -xt \b(Intensity of 579.06 nm Hg-line over burnerdiameter);
set %c -z 5; //set symbol-size to 5;

def analyse {
window -a %P;  //set previous worksheet active
worksheet -s; //unselect all
worksheet -s kk*step 975 kk*step 1050;  //select peak
worksheet -p 200;  //plot selected data
//run.section(setaxis); //change lay-out of graph with procedure "setaxis", written by P.Kemps
run h:\fit.ogs; //perform lorentz-fit
%(%O,1,kk*step)=kk*step; //write column-number to worksheet
aa=nlsf.p4;
aa=round(aa,1);
%(%O,2,kk*step)=aa; //write fit-area to worksheet
bb=nlsf.cod;  //get R^2 value
bb=round(bb,3);
%(%O,3,kk*step)=bb; //write R^2-value to worksheet
cc=nlsf.p2;
cc=round(cc,1);
%(%O,4,kk*step)=cc; //write Xc-value to worksheet
dd=nlsf.p1;
dd=round(dd,1);
%(%O,5,kk*step)=dd; //write Y0-value to worksheet
ee=nlsf.p3;
ee=round(ee,1);
%(%O,6,kk*step)=ee; //write W-value to worksheet
window -c %H; //close graph window
//type "column = $(kk*step)";
};
```

A.V fit.ogs

Description

This LabTalk-file is used in Microcal Origin 6. Both script-files *fit579.ogs* and *fit642.ogs* make use of this fit-procedure, which performs the actual Lorentz-fit on the selected data set. Fit-parameters are stored and can be read by the script-file that called this procedure. (The text behind the "//" is comment)

Source code

```
sec; //set timer to 0, for tool to time processes;
NumPeaks = 1;
nlsf.func$ = "Lorentz";
nlsf.numReplica=0;
%A=xof(%C);
ii=nlsf.tolerance; //save tolenrance
nlsf.tolerance=.005; //set tolerance
nlsf.cleanupfitdata();
nlsf.fitdata$=%C; //set active dataset for fitting
nlsf.v1=1; //1=vary Y0, 0=fix Y0
if(nlsf.iterate(1)==-1) //start non-linear least square fitter session.
    return 1;
nlsf.iterate(2);
nlsf.iterate(3);
if(nlsf.datastep > 4)
{
    nlsf.datastep/=2;
    nlsf.iterate(1);
    nlsf.iterate(2);
}
if(nlsf.datastep > 1)
{
    nlsf.datastep=1;
    nlsf.iterate(2);
}
nlsf.iterate(40);
//nlsf.end(8);
nlsf.tolerance=ii; //restore tolerance
type (column $(kk): W = $(p3) Y0= $(p1));
return        0;

def time {
    sec -e t;
    Type ($(%1): time= $(t) sec.);//tool to time processes
};
```

A.VI T-Profile-Calculator

Description

This program, created with [37], calculates the corresponding temperatures when a set of absolute intensities of 579.07 nm Hg emission lines from r=0 to r=$r_{lastdatapoint}$ is loaded and the effective Hg dose and effective temperature are given. Because the relation of the measured line intensity vs. temperature is not linear, this program uses a simple numerical procedure to calculate the temperature. The result of the calculation is plotted in red into a graph, which is visible on the screen. Besides that, the calculated

temperatures are stored in a file for use by other programs. The program has also the possibility of plotting a temperature profile (green) described by a formula introduced by Fischer. The parameters of the formula can be adjusted in such a way that the model fits the experimental data. In this way a very good estimate of the temperature profile over the entire burner diameter can be obtained.

Appearance

Source code

```
unit FTprofilecalculator;

interface

uses
  Windows, Messages, SysUtils, Variants, Classes, Graphics, Controls, Forms,
  Dialogs, StdCtrls, ExtCtrls, StrUtils, Math, ComCtrls;

type
  TForm1 = class(TForm)
    Label1: TLabel;
    EditHgDose: TEdit;
```

```
      Label2: TLabel;
      Bevel1: TBevel;
      BtnSelectInputFile: TButton;
      Label3: TLabel;
      Label4: TLabel;
      Label5: TLabel;
      Bevel2: TBevel;
      LabelInputFile: TLabel;
      Label6: TLabel;
      Label7: TLabel;
      LabelHgPressure: TLabel;
      BtnCalculateTr: TButton;
      PlotImage: TImage;
      UpDownHg: TUpDown;
      EditEffectiveT: TEdit;
      UpDownT: TUpDown;
      CheckBoxShowT: TCheckBox;
      Bevel3: TBevel;
      Label9: TLabel;
      Label10: TLabel;
      Label11: TLabel;
      EditTwall: TEdit;
      EditGamma: TEdit;
      UpDownGamma: TUpDown;
      EditT1T2: TEdit;
      UpDownT1T2: TUpDown;
      Label8: TLabel;
      LabelEffT: TLabel;
      OpenDialog1: TOpenDialog;
      Label12: TLabel;
      Label13: TLabel;
      Label14: TLabel;
      EditRlastdatapoint: TEdit;
      Label15: TLabel;
      Label16: TLabel;
      Edittshutter: TEdit;
      Label17: TLabel;
      procedure HgDoseChange(Sender: TObject);
      procedure EditEffectiveTChange(Sender: TObject);
      procedure EditGammaChange(Sender: TObject);
      procedure EditTwallChange(Sender: TObject);
      procedure EditT1T2Change(Sender: TObject);
      procedure EditRlastdatapointChange(Sender: TObject);
      procedure EdittshutterChange(Sender: TObject);
      procedure CalculateP;
      procedure CalculateTmodel;
      procedure FormCreate(Sender: TObject);
      procedure FormClose(Sender: TObject; var Action: TCloseAction);
      procedure BtnSelectInputFileClick(Sender: TObject);
      procedure BtnCalculateTrClick(Sender: TObject);
      procedure Drawgraph;
      procedure UpDownHgClick(Sender: TObject; Button: TUDBtnType);
      procedure UpDownTClick(Sender: TObject; Button: TUDBtnType);
      procedure UpDownGammaClick(Sender: TObject; Button: TUDBtnType);
      procedure UpDownT1T2Click(Sender: TObject; Button: TUDBtnType);
      procedure CheckBoxShowTClick(Sender: TObject);
      procedure Plotgrafiek(Destination:TCanvas;getmaxx,getmaxy:integer);

  private
    { Private declarations }
  public
    { Public declarations }
  end;
```

```
Type
 data=array [1..1000] of double;
 dataint=array [1..1000] of integer;

Const
 A=2.04E8;
 gup=5;
 hnu=3.43E-19;
 k=1.38E-23;
 Eup=1.417E-18;
 conversion=4*pi*2.964E-4/4.44E-5; // conversion=4*pi*Beta/deltax

var
 Form1: TForm1;
 HgDose,Phg,T1T2,gamma,Rlastdatapoint,tshutter: Double;
 default_dir: string;
 InputFileName: string;
 Urad: data;
 Tr: data;
 Datapoints,EffectiveT,Twall: integer;
//Vars from Graphs
 PlotZoom,DrawZoom,DrawZoomMin                    : double;
 xfac, yfac, mark_x, mark_y, border          : smallint;
 minx, miny, intx, inty, maxx, maxy, offset1, offset2   : single;
 plot_text, x_text, y_text              : string;
 j{, getmaxx, getmaxy}                : integer;
 xmaxax, ymaxax, xtick, ytick, xcomx, xcomy, ycomx, ycomy, xvalx : longint;
 xvaly, yvalx, yvaly, x1, y1, x2, y2, leftax        : longint;
 beginplot, plotwidth, plotwidth2, rightax, botax, topax     : longint;
 xarray, yarray, xarray2, yarray2              : data;
 FastGraphTime, SlowGraphTime              : integer;
 FastGraph                    : boolean;

implementation

{$R *.dfm}

procedure TForm1.HgDoseChange(Sender: TObject);
begin
 If EditHgDose.Text<>" then
 begin
  Hgdose:=1E-6*StrToFloat(editHgDose.Text);
  CalculateP;
  if PlotImage.Visible then BtnCalculateTrClick(nil);
 end;
end;

procedure TForm1.EditEffectiveTChange(Sender: TObject);
begin
 If EditHgDose.Text<>" then
 begin
  EffectiveT:=StrToInt(editEffectiveT.Text);
  CalculateP;
  if PlotImage.Visible then BtnCalculateTrClick(nil);
 end;
end;

procedure TForm1.EditGammaChange(Sender: TObject);
begin
 If EditGamma.Text<>" then
 begin
  Gamma:=StrToFloat(EditGamma.Text);
  CalculateTmodel;
 end;
```

```
  end;

procedure TForm1.EditTwallChange(Sender: TObject);
begin
  If EditTwall.Text<>'' then
  begin
   Twall:=StrToInt(EditTwall.Text);
   CalculateTmodel;
  end;
end;

procedure TForm1.EditT1T2Change(Sender: TObject);
begin
  If EditT1T2.Text<>'' then
  begin
   T1T2:=StrToFloat(EditT1T2.Text);
   CalculateTmodel;
  end;
end;

procedure TForm1.EditRlastdatapointChange(Sender: TObject);
begin
  If EditRlastdatapoint.Text<>'' then
  begin
   Rlastdatapoint:=StrToFloat(EditRlastdatapoint.Text);
   if PlotImage.Visible then Drawgraph;
  end;
end;

procedure TForm1.EdittshutterChange(Sender: TObject);
begin
  If StrToFloat(Edittshutter.Text)<>0 then
  begin
   tshutter:=StrToFloat(Edittshutter.Text);
   if PlotImage.Visible then BtnCalculateTrClick(nil);
  end;
end;

procedure TForm1.CalculateP;
begin
  Phg:=Hgdose*k*effectiveT/(200.6*1.66E-27*2.88E-7*pi); {2.88E-7*pi is cylindervolume with r=4mm and h=18mm}
  LabelHgPressure.Caption:=FloatToStrF(Phg/1E5,fffixed,7,2);
end;

procedure TForm1.CalculateTmodel;
var i,modelpoints:integer;
    sum:double;

begin
  modelpoints:=1000;
  plotwidth2:=modelpoints-1;
  if Tr[1]<>0 then
  begin
   // -----filling of plotarrays
   for i:=0 to modelpoints-1 do
   begin
     xarray2[i]:=i*4/modelpoints;
     yarray2[i]:=Twall+(((Tr[1]-Twall)*T1T2)/(T1T2+1))*(1-sqr(i/modelpoints))+((Tr[1]-
Twall)/(1+T1T2))*exp(gamma*LN(1-sqr(i/modelpoints)));
   end;
   // -----calculation of Teffective
   sum:=0;
   for i:=1 to modelpoints do
   begin
```

```
      sum:=sum+((i-0.5)*sqr(4/modelpoints))/(0.5*(yarray2[i-1]+yarray2[i]));
    end;
    LabelEffT.Caption:=FloatToStrF(8/sum,fffixed,4,0);
  end;
 if PlotImage.Visible then drawgraph;
end;

procedure TForm1.FormCreate(Sender: TObject);
var f:textfile;

begin
 getdir(0,default_dir);
 default_dir:=default_dir+'\';
 assignfile(f,default_dir+'settings.set');
 reset(f);
 readln(f,HgDose);
 readln(f,effectiveT);
 readln(f,Twall);
 readln(f,gamma);
 readln(f,T1T2);
 readln(f,Rlastdatapoint);
 readln(f,tshutter);
 EditHgDose.text:=FloatToStr(1E6*HgDose);
 EditEffectiveT.text:=IntToStr(effectiveT);
 EditTwall.Text:=IntToStr(Twall);
 EditGamma.Text:=FloatToStr(gamma);
 EditT1T2.Text:=FloatToStr(T1T2);
 EditRLastDataPoint.Text:=floatToStr(Rlastdatapoint);
 Edittshutter.Text:=floatToStr(tshutter);
 CloseFile(f);
 CalculateP;
end;


procedure TForm1.FormClose(Sender: TObject; var Action: TCloseAction);
var f:textfile;
begin
 assignfile(f,default_dir+'settings.set');
 rewrite(f);
 writeln(f,HgDose);
 writeln(f,effectiveT);
 writeln(f,Twall);
 writeln(f,gamma);
 writeln(f,T1T2);
 writeln(f,Rlastdatapoint);
 writeln(f,tshutter);
 closefile(f);
end;

procedure TForm1.BtnSelectInputFileClick(Sender: TObject);
var i:integer;
    f:textfile;

begin
 If OpenDialog1.Execute then
 begin
  InputFileName:=opendialog1.FileName;
  LabelInputFile.Caption:=InputFileName;
  AssignFile(f, InputFileName);
  Reset(f);
  i:=1;
  While not eof(f) do
  begin
   readln(f ,Urad[i]);
```

```
    inc(i);
  end;
  datapoints:=i-1;
  CloseFile(f);
  BtnCalculateTr.Visible:=true;
 end;
end;

procedure TForm1.BtnCalculateTrClick(Sender: TObject);
Const Tstart=1000;
var i: integer;
   Ur,U,Ulast,T,Tstep,Tlast: double;
   f1:textfile;

 procedure CalculateU;
 begin
  U:=A*hnu*Phg*gup*exp(-Eup/(k*T))/(k*T);
 end;

begin
 assignfile(f1,default_dir+'output.out');
 rewrite(f1);
 for i:=1 to datapoints do
 begin
  Tstep:=500;
  //Ur:=Urad[i]/tshutter; if this programm is used for shuttertime correction, this line must be used
  Ur:=Urad[i];
  T:=Tstart;
  U:=0;
  Repeat
   Repeat
    Ulast:=U;
    Tlast:=T;
    T:=T+Tstep;
    CalculateU;
   Until abs(Ur-U)>abs(Ur-Ulast);
   Tstep:=-Tstep/2;
  Until abs(T-Tlast)<0.1;
  Tr[i]:=T+Tstep;
  Write(f1,i/datapoints*Rlastdatapoint:12);write(f1,'':4);writeln(f1,T+Tstep:12);
 end;
 closefile(f1);
 if CheckBoxShowT.Checked then CalculateTmodel;
 Drawgraph;
end;

procedure TForm1.UpDownHgClick(Sender: TObject; Button: TUDBtnType);
begin
 if button=btnext then
   EditHgDose.Text:=FloatToStrF(StrToFloat(EditHgDose.Text)+0.1,fffixed,3,1)
  else
   EditHgDose.Text:=FloatToStrF(StrToFloat(EditHgDose.Text)-0.1,fffixed,3,1)
end;

procedure TForm1.UpDownTClick(Sender: TObject; Button: TUDBtnType);
begin
 if button=btnext then
   EditEffectiveT.Text:=IntToStr(StrToInt(EditEffectiveT.Text)+10)
  else
   EditEffectiveT.Text:=IntToStr(StrToInt(EditEffectiveT.Text)-10)
end;

procedure TForm1.UpDownGammaClick(Sender: TObject; Button: TUDBtnType);
begin
```

```
    if button=btnext then
      EditGamma.Text:=FloatToStr(StrToFloat(EditGamma.Text)+0.1)
    else
      EditGamma.Text:=FloatToStr(StrToFloat(EditGamma.Text)-0.1)
  end;

  procedure TForm1.UpDownT1T2Click(Sender: TObject; Button: TUDBtnType);
  begin
    if button=btnext then
      EditT1T2.Text:=FloatToStr(StrToFloat(EditT1T2.Text)+0.1)
    else
      EditT1T2.Text:=FloatToStr(StrToFloat(EditT1T2.Text)-0.1)
  end;

  procedure TForm1.CheckBoxShowTClick(Sender: TObject);
  begin
   if PlotImage.Visible then
    begin
     CalculateTmodel;
     Drawgraph;
    end;
  end;

  procedure TForm1.Drawgraph;
  var i: integer;
  begin
    for i:=1 to datapoints do
    begin
      xarray[i-1]:=i/datapoints*Rlastdatapoint;
      yarray[i-1]:=Tr[i];
    end;
    minx:=0;
    maxx:=4;
    maxy:=6500;
    miny:=1000;
    x_text:= 'radius (mm)';
    mark_x := 4;
    mark_y := 11;
    y_text := 'Temperature (K)';
    plot_text := 'Taxis = '+FloatToSTrF(Tr[1],fffixed,7,0)+' K';
    plotwidth:=datapoints-1;
    Form1.Height:=598;
    PlotImage.Visible:=True;
    plotgrafiek(PlotImage.Canvas,PlotImage.Width-5,PlotImage.Height);
  end;

  procedure TForm1.plotgrafiek(Destination:TCanvas;getmaxx,getmaxy:integer);
  {This routine plots the graph. It has been adopted from Marco Haverlag's Eldes Code and modified severely by
Sander Nijdam and Pim Kemps}
  var i        : integer;
      s        : string;
      Arect    : Trect;
      textdir  : integer;
      clipregion : Thandle;
  begin
    with Destination do
     begin
      textdir := 0;
      font.handle:=createfont(0,0,round(10*textdir),round(10*textdir),
              fw_bold,0,0,0,default_charset,out_tt_precis,clip_default_precis,
              proof_quality,variable_pitch or 4 or ff_swiss,'');
      pen.width := 1; pen.color := $00000000;

      ARect := Rect(0, 0, Width, Height);
```

```
brush.color := $00F3F3F3;
fillrect(Arect);

leftax := round(71/640*getmaxx); rightax := round(625/640*getmaxx);
botax := round(424/480*getmaxy); topax := round(15/480*getmaxy);
xfac := rightax-leftax; yfac := botax-topax;
xmaxax := getmaxx; ymaxax := getmaxy; xcomx := round(leftax+0.45*xfac);
xcomy := (round(455/480*getmaxy));
ycomx := round(10/640*getmaxx); ycomy := round(topax+0.65*yfac);
xvalx := round(60/640*getmaxx); xvaly := round(434/480*getmaxy);
yvalx:= ifthen(maxy < 1000, round(40/640*getmaxx), round(35/640*getmaxx));
if maxy < 100 then yvalx  := round(45/640*getmaxx);
yvaly := round(414/480*getmaxy);
moveto(leftax-border,topax-border); lineto(leftax-border,botax+border);
lineto(rightax+border,botax+border); lineto(rightax+border,topax-border);
lineto(leftax-border,topax-border);
intx := maxx-minx;
inty := maxy-miny;
//------------------    draw the grid
for i:=0 to mark_x do
begin
  pen.color:=$00BBBBBB;
  moveto(round(i/mark_x*xfac+leftax),botax);
  lineto(round(i/mark_x*xfac+leftax),botax+(topax-botax));
  s:=FloatToStrF(minx+i*intx/mark_x,fffixed,7,2);
  Font.size:=10;
  textout(xvalx+i*(xfac div mark_x),xvaly+border,s);
end;
textout(xcomx,xcomy+border,x_text);
textdir:=90;
font.handle:=createfont(10,8,round(10*textdir),round(10*textdir),
        fw_bold,0,0,0,default_charset,out_tt_precis,clip_default_precis,
        proof_quality,variable_pitch or 4 or ff_swiss,'');
textout(ycomx-border,ycomy,y_text);
textdir:=0;
font.handle:=createfont(0,0,round(10*textdir),round(10*textdir),
        fw_bold,0,0,0,default_charset,out_tt_precis,clip_default_precis,
        proof_quality,variable_pitch or 4 or ff_swiss,'');
for i:=0 to mark_y do
begin
  moveto(leftax,round(botax-i/mark_y*yfac));
  lineto(leftax-(leftax-rightax),round(botax-i/mark_y*yfac));
  s:=FloatToStrF(miny+i*inty/mark_y,fffixed,7,0);
  Font.size:=10;
  textout(yvalx-border,yvaly-i*(yfac div mark_y),s);
end;
//------------------    write label
font.color:=$00999999;
Font.size:=12;
textout(leftax+5,topax+4,plot_text);
font.color:=$00000000;
clipregion:=createrectrgn(leftax,topax,rightax,botax);
selectcliprgn(handle, clipregion);
//------------------    plot graph2
if CheckBoxShowT.Checked then
begin
 pen.color:=clgreen;
 pen.width:=2;
 if intx=0 then intx:=1;
 x1:=leftax+round((xarray2[beginplot]-minx)/intx*xfac);
 y1:=botax-round((yarray2[beginplot]-miny)/inty*yfac);
 moveto(x1,y1);
 for i:=beginplot to beginplot+plotwidth2 do
 begin
```

```
     x1:=leftax+round((xarray2[i]-minx)/intx*xfac);
     y1:=botax-round((yarray2[i]-miny)/inty*yfac*(height-162)/(height-160))-1;
      lineto(x1,y1);
    end;
     x1:=leftax+round((xarray[beginplot]-minx)/intx*xfac);
   end;
   //------------------    plot graph1
   pen.color:=clred;
   pen.width:=2;
   if intx=0 then intx:=1;
   x1:=leftax+round((xarray[beginplot]-minx)/intx*xfac);
   y1:=botax-round((yarray[beginplot]-miny)/inty*yfac);
   moveto(x1,y1);
   for i:=beginplot to beginplot+plotwidth do
   begin
     x1:=leftax+round((xarray[i]-minx)/intx*xfac);
     y1:=botax-round((yarray[i]-miny)/inty*yfac*(height-162)/(height-160))-1;
      lineto(x1,y1);
    end;
    pen.color:=$00000000;
    DeleteObject(clipregion);
  end;
end;

end.
```

Appendix B: Parabolic Flight Sequence October 2003

Parabola sequence Bordeaux Oktober 2003

Day 1:

time (10s.)	start zero-G	parabola#	parabolamp	lamp	power	nm-filter	greyfilter	shuttertime (ms)	saturation (%)
14:20:48	14:21:26	0	46 hor.	19	254	1	4	laser adjusting	
14:23:48	14:24:26	1	46 hor.	19	254	1	4	200	too weak
14:26:48	14:27:26	2	46 hor.	19	254	2	2	1000	25
14:29:48	14:30:26	3	46 hor.	19	254	3	2	800	26.5
14:32:48	14:33:26	4	46 hor.	19	254	1	5	160	25
14:35:48	14:36:26	5	46 hor.	19	254	2	3	300	46
14:40:48	14:41:26	6	46 hor.	20	254	1	4	200	22
14:43:48	14:44:26	7	46 vert.	20	254	2	2	500	23
14:47:48	14:48:26	8	46 vert.	20	254	3	2	600	31
14:50:48	14:51:26	9	46 vert.	20	254	1	5	200	56
14:53:48	14:54:26	10	46 vert.	20	254	2	2	600	28
14:59:48	15:00:26	11	46 vert.	18	226	2	3	350	29
15:02:48	15:03:26	12	46 vert.	18	226	3	3	150	26
15:05:48	15:06:26	13	46 vert.	18	239	2	3	250	27
15:08:48	15:09:26	14	off	18	239	3	3	500	69
15:11:48	15:12:26	15	off	18	239	2	3	800	67
15:20:48	15:21:26	16	43 hor.	16	254	**	**		
15:23:48	15:24:26	17	43 hor.	16	254	**	**		
15:26:48	15:27:26	18	43 hor.	16	254	1		1500	30
15:29:48	15:30:26	19	43 hor.	16	254	1		3000	56
15:32:48	15:33:26	20	43 hor.	16	254	3		500	80
15:38:48	15:39:26	21	43 hor.	12	254	1	4	400	
15:41:48	15:42:26	22	43 hor.	12	254	2	3	200	
15:45:48	15:46:26	23	43 hor.	12	254	3	2	600	28
15:52:48	15:53:26	24	43 vert.	12	254	1	4	400	38
15:55:48	15:56:26	25	43 vert.	12	254	2	3	250	55
16:00:49	16:01:27	26	43 vert.	20	254	2	3	200	
16:03:48	16:04:26	27	43 vert.	20	254	2	3	200	
16:06:48	16:07:26	28	43 vert.	20	254	2	3	200	55
16:09:48	16:10:26	29	43 vert.	20	254	1	4	600	
16:12:48	16:13:26	30	43 vert.	20	254	1	4	600	81

Day 2:

time (10s.)	start zero-G	parabola#	parabolamp
10:24:50	10:25:28	0	50 hor.
10:27:50	10:28:28	1	50 hor.
10:30:50	10:31:28	2	50 hor.
10:33:50	10:34:28	3	50 hor.
10:36:50	10:37:28	4	50 hor.
10:39:50	10:40:28	5	50 hor.
10:44:50	10:45:28	6	50 hor.
10:47:50	10:48:28	7	50 vert.
10:50:50	10:51:28	8	50 vert.
10:54:50	10:55:28	9	50 vert.
10:57:50	10:58:28	10	50 vert.
11:04:50	11:05:28	11	50 vert.
11:07:50	11:08:28	12	50 vert.
11:12:50	11:13:28	13	50 vert.
11:15:50	11:16:28	14	off
11:18:50	11:19:28	15	off
11:27:50	11:28:28	16	52 hor.
11:30:50	11:31:28	17	52 hor.
11:33:50	11:34:28	18	52 hor.
11:36:50	11:37:28	19	52 hor.
11:40:50	11:41:28	20	52 hor.
11:46:50	11:47:28	21	52 hor.
11:49:50	11:50:28	22	52 hor.
11:52:50	11:53:28	23	52 vert.
11:55:50	11:56:28	24	52 vert.
11:58:50	11:59:28	25	52 vert.
12:03:50	12:04:28	26	52 vert.
12:06:50	12:07:28	27	52 vert.
12:09:50	12:10:28	28	52 vert.
12:12:50	12:13:28	29	52 vert.
12:15:50	12:16:28	30	52 vert.

Helical Instabilities measurements

Day 3:

time (10s.)	start zero-G	parabola#	parabolamp	lamp	power	nm-filter	greyfilter	shuttertime (ms)	saturation (%)
10:25:51	10:26:29	0	H1 hor	12	254	1	4	500	ok
10:28:52	10:29:29	1	H1 hor	12	254	2	3	250	ok
10:32:51	10:32:29	2	H1 hor	12	254	3	2	1200	ok
10:35:51	10:35:29	3	H1 hor	12	254	1	4	650	ok
10:38:51	10:38:29	4	H1 hor	12	254	2	3	300	ok
10:41:51	10:41:29	5	H1 hor	12	254	3	3	150	ok
10:49:51	10:50:29	6	H1 hor	19	254	1	5	400	ok
10:52:51	10:53:29	7	H1 vert	19	254	2	3	400	ok
10:55:51	10:56:29	8	H1 vert	19	254	3	3	200	ok
10:58:51	10:59:29	9	H1 vert	19	254	1	5	500	ok
11:01:51	11:02:29	10	H1 vert	19	254	2	3	500	ok
11:07:51	11:08:29	11	H1 vert						
11:10:51	11:11:29	12	H1 vert						
11:13:51	11:14:29	13	H1 vert						
11:16:51	11:17:29	14	off						
11:19:51	11:20:29	15	off						
11:29:51	11:30:29	16	H2 hor						
11:32:51	11:33:29	17	H2 hor						
11:35:51	11:36:29	18	H2 hor						
11:38:51	11:39:29	19	H2 hor						
11:41:51	11:42:29	20	H2 hor						
11:48:51	11:49:29	21	H2 hor						
11:51:51	11:52:49	22	H2 hor						
11:54:51	11:56:09	23	H2 vert						
11:57:51	11:59:29	24	H2 vert						
12:00:51	12:02:49	25	H2 vert						
12:11:51	12:12:29	26	H2 vert						
12:14:51	12:15:29	27	H2 vert						
12:17:51	12:18:29	28	H2 vert						
12:20:51	12:21:29	29	H2 vert						
12:23:51	12:24:29	30	H2 vert						

Helical Instabilities measurements

Appendix C: Calculation of the effective mercury dose

To determine the amount of mercury present in the discharge volume, which is defined as the burner volume minus the volume "behind" the top of the electrodes, the *electrode volume,* we have to estimate the temperature of this electrode volume.

Therefore, we distinguish two extreme cases:

1. The average temperature of the electrode volume is equal to the wall temperature.
2. The average temperature of the electrode volume is equal to the effective temperature of the discharge volume.
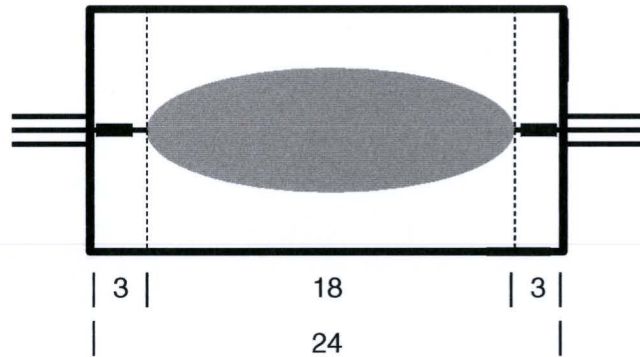
Figure C.1: *Schematic drawing of the burner used in the ARGES experiments, with some characteristic dimensions in mm.*

With the dimensions of the used burner, as shown in Fig. C1, we can calculate the fraction of the mercury in the discharge for both extreme cases. For case 1, we estimate that the wall temperature is approximately 0.5 times the effective discharge temperature. In real, case 1 is an underestimation of the temperature in the electrode volume. Because the mercury density in the electrode volume is in this case twice the average mercury density in the discharge, the fraction of the total mercury dose present in the discharge volume is 50%.

For case 2, where the electrode volume is assumed to have the same temperature as the effective discharge temperature (overestimation), the mercury density in the electrode volume is equal to the average mercury density in the discharge. Therefore, the fraction mercury in the discharge is equal to the ratio of the discharge volume and the total burner volume, which is 75%.

Because the real situation is in between both extreme cases, we choose the effective mercury dose to be 62% of the actual mercury dose. The maximum error in the effective mercury dose introduced by this estimation is thus (75%-62%)/62% = 21%.

Acknowledgements